Energy Transfer Processes in Supramolecular Light-Harvesting Systems

Amy Louise Stevens

Balliol College

University of Oxford

A thesis submitted for the degree of *Doctor of Philosophy*.

Michaelmas Term 2011

"I believe that these mysteries are not separate entities but are in fact complimentary verses of the same song. Now, I cannot hear it yet, but I can feel it and that is enough for me to proceed."

Dale Cooper, *Twin Peaks*

ABSTRACT

Energy Transfer Processes in Supramolecular Light-Harvesting Systems

Amy L. Stevens, Balliol College, submitted for DPhil Michaelmas term 2011

This dissertation attempts to understand how energy transfer in a molecular wire and a spherical organic assembly are affected by molecular structure. The molecular wire is a DNA-hybrid structure composed of a strand of thymine bases appended by a cyanine dye. Hydrogen bonded to each base is a naphthalene-derivative molecule. Using time-integrated photoluminescence and time-correlated single photon counting measurements, energy transfer from the naphthalene donors to the cyanine acceptors was confirmed, and its dependence on temperature and DNA-template length investigated. Donor-thymine bonding was disrupted at temperatures above $\sim$25°C resulting in poor donor template decoration and low rates of energy transfer. Increasing numbers of donors attach to the scaffold, forming an orderly array, as the template length increases due to the stabilising effects of the donor-donor π-stacking interactions. Conversely, modelled energy transfer rates fall as the scaffold length increases because of the longer donor-acceptor distances involved. Therefore, the energy transfer rate was greatest for a template built from 30 thymines.

The spherical organic assemblies (nanoparticles) are formed by fast injection of a small volume of molecularly dissolved fluorene-derivative amphiphilic molecules into a polar solvent. The amphiphilic molecules contained either a naphthalene (donor) or a benzothiadiazole (acceptor) core. The donor-acceptor mixed nanoparticles resemble an amorphous polymer film and were modelled as such using the Förster resonance energy transfer theory. The Förster radii extracted from the measurements depends intricately on the donor-acceptor spectral overlap and distance. The latter effect was controlled by the stacking interactions between the molecules.

Altering the morphology of the structural units is the key to optimising energy transfer in molecular structures. To achieve efficient organic molecule-based devices, the importance of this property needs to be fully appreciated and effectively exploited.

Acknowledgements

Many people have helped me during my PhD years at Oxford. My sincerest gratitude goes to my supervisor, Laura Herz. Thank you for helping me wade through the muddy waters of organic molecule research and for teaching me to view all experimental results with suspicion.

I have also worked closely with some of the members of the Eindhoven University of Technology, including Pim Janssen, Amparo Ruiz-Carretero, Adrien Kaeser, their supervisor Albert Schenning. Mathieu Surin, at the University of Mons, helped with some theoretical modelling.

I wish to thank the members of the Organic Semiconductors and the Teraherz Photonics groups at Oxford, past and present. Getting to know you has made my time at Oxford much more colourful.

Balliol College and my college advisor, Dr. David Lucas, have supported me every step of the way. Thank you for the tutoring opportunity and the financial support. The Oxford Condensed Matter Physics subdepartment has helped to fund travel to conferences, while the ESPRC has enabled me to live and eat.

I thank my parents for being supportive and understanding that a PhD entails a huge time commitment.

Thanks to serendipity, who is never thanked enough.

Finally, I thank my beloved Steven. You have been my truest friend and ally and have opened my eyes to many many things such as human nature, huge swathes of the food pyramid that I believed previously were inedible, computers, maths, great music, and semi-colons.

Table of contents

Chapter 1

Introduction

Organic molecules are poised to become important electronic devices in the near future. Organic material properties have been exploited for use in solar cells[80, 116], thin-film transistors[113], field-effect transistors[9], light-emitting devices[185, 116], molecular wires[33, 11, 166], and chemical and biological sensors[185, 119]. The advantage of these materials is the ease with which their properties can be manipulated through careful engineering of their chemical structures[31]. However, the real driving force pushing development in the field of organic materials is the potential to produce ultra-low cost devices. This potential needs to be captured through innovative large-scale fabrication techniques such as improved solution deposition methods[188] or roll-to-roll thermal transfer processes[57]. Another key requirement is improved device performance. Organic semiconductors suffer from small carrier mobilities due to the hopping mechanism of photoexcitations from conjugated region to conjugated region. Hence, the morphology of the materials, either amorphous or crystalline, results in mobilities ranging from $<1\,\mathrm{cm^2V^{-1}s^{-1}}$ to in excess of $40\,\mathrm{cm^2V^{-1}s^{-1}}$, respectively[116, 103], from which single-crystal devices with mobilities

up to $30\,cm^2V^{-1}s^{-1}$ have been fabricated[66, 104, 145, 77]. Another morphology-dependent process is the interaction of nearby conjugated chains. For example, insulating a conjugated polymer chain with nonconjugated insulating macrocycles failed to prevent interchain interactions which resulted in distorted excitation dynamics[33]. Clearly, if device performance is to be improved, it is important to understand the role of morphology in these materials. This dissertation aims to examine the role of morphology in some new molecular systems.

Chapter 2 contains background material relating to organic semiconductors, especially their self-assembling ability, and the theories that have been developed to describe their optical properties.

In Chapter 3, time-integrated photoluminescence and time-correlated single photon counting techniques are discussed, with reference to experimental setups and nonlinear laser physics principles. The techniques examined in this chapter are used to generate the results presented in the rest of the thesis.

The first organic samples investigated were the self-assembling DNA-hybrid structures in Chapter 4. These structures are composed of diaminopurine-equipped naphthalene derivatives that are hydrogen-bonded along a single-stranded oligothymine template. By performing time-resolved measurements of the naphthalene donor luminescence decay in the absence and presence of a cyanine dye acceptor bonded covalently to the 5' end of the oligothymine, the role of temperature and DNA template length on the energy transfer from donors to the acceptor

was examined. The energy transfer rate depended on the template length in a complex way. Hence, in order to replicate the observed transfer dynamics, a model assuming Förster energy transfer occurs between donors and acceptors was constructed whose geometric arrangement had been determined through Molecular Dynamics simulations of the whole assembly structure. This model is discussed in Chapter 5. The simulated and the experimental data, taken together, shed light on the energy transfer rate's template dependence. This is in spite of the simplicity of the model. These results suggested that efficient energy transfer, in excess of that expected from simple Förster calculations, is feasible even for long DNA-templated assemblies of π-stacked conjugated chromophores. Such structures may therefore act as molecular wires transporting energy from one end to another. However, it is interesting that the order of the donor array is crucial to achieve efficient energy transfer.

Smaller nanoparticle systems, formed from fluorene-derivative amphiphiles, were investigated in chapters 6 and 7. Nanoparticles are interesting systems to study because of their large range of potential uses, especially in biology as probes to track and image specific biomolecules. In Chapter 6, nanoparticles were formed from these amphiphiles by injecting a small volume of molecularly dissolved non-polar amphiphile solution into a large volume of polar solvent. Nanoparticles form as a natural consequence of trying to reduce the energy of the system by limiting hydrophobic interactions between the non-polar molecule end and the polar solvent. The core group in the amphiphile molecules was a naphthalene or a benzothiadiazole such that the resulting chromophore acted as a donor or acceptor, respectively. The stacking in the donor-only or acceptor-only nanoparticles was investigated and it was shown that the stability of the

samples depended on the molecules' ability to stack intimately.

The scope of invesigation was widened to include nanoparticles containing a mixture of donor and acceptor amphiphiles in Chapter 7. Time-integrated and time-resolved measurements were performed on the samples as a function of the percentage of acceptors in the nanoparticles. The nanoparticles resembled an amorphous polymer film and were modelled as such using the Förster resonance energy transfer theory. Förster radii were extracted from three sources: photoluminescence intensities, photoluminescence decays, and donor / acceptor spectral overlap. Again, the results were found to depend critically on the stacking interactions between the amphiphiles. The morphology of the molecules in the nanoparticle system has a clear bearing on the energy transfer efficiency and, hence, the fluorescence intensities of the nanoparticles. This, in turn, determines their usefulness as probes and environmental sensors.

In Chapter 8, the specific photophysics results and general themes of the dissertation are summarised. Some space is dedicated to future experiments that follow naturally from the results presented in the thesis.

Chapter 2

Background theory

This chapter reviews the fundamental optical properties of conjugated polymer materials, and the models used to describe energy transport within them. A brief treatise is given on self-assembly and interchain interactions.

2.1 Conjugated material properties

2.1.1 Nature of the fundamental excitations

In conjugated compounds, electrons from unhybridised p-like atomic states of sp^2-hybridised carbon atoms cooperate to form large delocalised orbitals called π orbitals[60, 158, 116, 166, 80]. These orbitals spread out across the whole molecule, promote electron conduction[166], and are highly polarisable[80, 11]. Conjugated compounds occur as small molecules, polymers, or biological materials with a well-defined molecular weight, an indeterminate number of molecu-

lar repeat units, and a high level of complexity, respectively[57]. For all their differences, the π-conjugation is the origin of the electronic and optical properties of all these compounds[37].

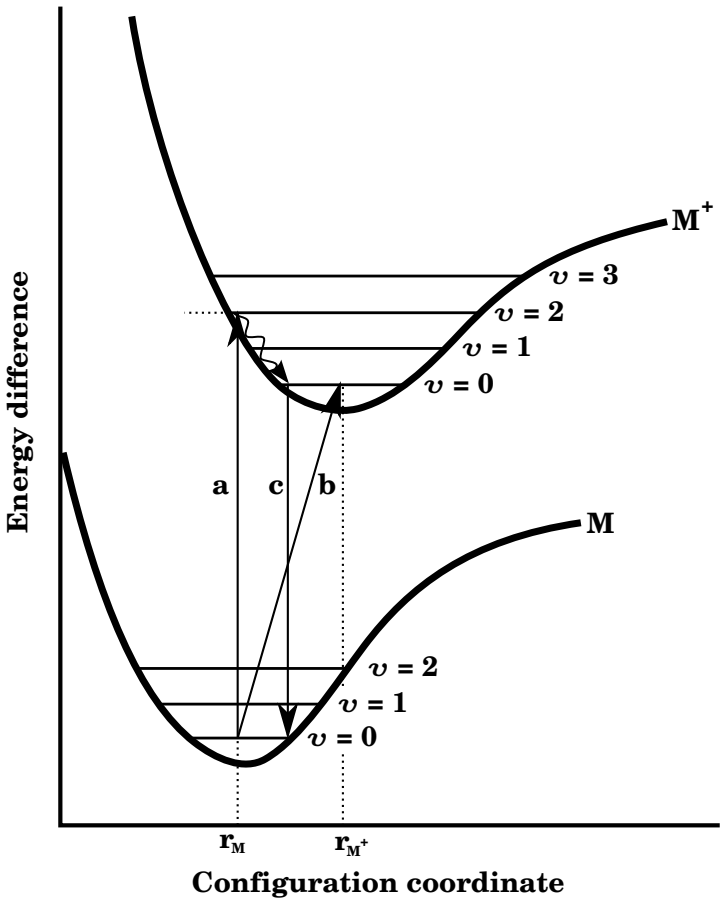

Figure 2.1: Adapted from [158]. Two electronic states: *a* denotes a Franck-Condon transition, *b* represents a zero-phonon transition, wavy arrow is a radiationless transition between vibrational states of the upper electronic level, *c* is the emission or fluorescence transition, with the distance between r_M and r_{M*} representing the configurational coordinate displacement of the upper state relative to the ground electronic state.

The π-molecular orbitals define the electronic levels of the highest occupied molecular (HOMO) and lowest unoccupied molecular (LUMO) orbitals[116]. The HOMO-LUMO band gap, a result of the so-called Peierls instability[158, 201] (1D chains) or Jahn-Teller effect[142] (molecules), is typically 1.5 to 3 eV which permits excitation of conjugated compounds by light in the visible region[80, 197]. Upon excitation, an electron is promoted to the conduction band leaving behind an empty electron state (hole) in the otherwise filled valence band. The electron and hole can mutually interact via the Coulombic attraction to form a tightly-bound excitonic state. This electrically neutral electron-hole pair, for the case of Frenkel excitons, has a binding energy of ∼1 eV and is localised on a single molecule at a time. It can 'hop' to other molecules on a chain (intrachain hopping) or other molecules on an adjacent chain (interchain hopping)[57, 55, 197]. Other photoexcitations that can occur and travel throughout the material are larger-diameter more weakly bound excitons, i.e. charge-transfer states, charge carriers, i.e. electrons or holes[57], and polarons[185]. Other excitations such as solitons, present in some conjugated materials, have energy levels between the HOMO and LUMO levels[55].

2.1.2 Shape of the spectra

The total energy of a molecule in its ground state and excited state, respectively, is

$$E_t = E_e + E_v + E_r \tag{2.1}$$

$$E_t' = E_e' + E_v' + E_r' \tag{2.2}$$

where the subscripts represent the electronic (e), vibrational (v), and rotational (r) energy components[28]. The Born-Oppenheimer approximation assumes that the wavefunctions of ground and excited vibronic states can be separated into electronic and vibrational components because of the large disparity between electronic and nuclear masses[158]. Electrons can move from the ground state S_0 to the first excited singlet state S_1, by absorbing a photon with an energy higher than the HOMO-LUMO gap. Higher excited states S_2, S_3 do exist, but they decay at an extremely rapid rate, by internal conversion, into the S_1 state[17]. Hence, an absorption transition is defined as

$$\Delta E = E'_x - E_x \tag{2.3}$$

where x is either the electronic or vibrational energy component, as the rotational energy is negligibly small in comparison[28].

In π-conjugated systems, the bond lengths are modulated by the π-electron densities on the bonds. Upon energy absorption, the π-electron densities change which modifies the bond lengths[116]. This strong connection between electronic structure and geometric structure is known as electron-vibration coupling[116, 197], and assigns corresponding vibronic shoulders to each electronic absorption band[181]. Figure 2.1 represents these as vibronic levels ($\mu = 0, 1, ...$) inside an electronic manifold. The absorption transition is given by the vertical 'a' arrow in the diagram. This is a consequence of the Franck-Condon principle, which assumes that the electronic transitions are so rapid compared to motions of the nuclei setting up the molecular skeleton that the positions of the nuclei can be taken as constant during the electronic transition[197]. After the 'a' absorption transition, in Figure 2.1, the excitation loses vibrational

energy before decaying to the ground state ('c' arrow in Figure). The difference between the 0-vibration absorption band and the 0-vibration emission band is called Stokes shift. The shape of the fluorescence emission spectrum will generally be similar to the shape of the first absorption band (although in mirror image relationship to it) because the distribution of levels in the first excited state, which is responsible for the shape of the first absorption band, is generally similar to the distribution of levels in the ground state, which is responsible for the shape of the fluorescence band[152].

Instead of decaying back to the ground state and emitting fluorescence, the energy can cross to a triplet state, through a process known as intersystem crossing[158, 28]. The singlet state has a total spin multiplicity of zero[116]; the triplet state, a total spin multiplicity of three[142]. This transition is forbidden[158] unless a heavy metal atom is present to enhance the spin-orbit coupling and partially allow the transfer[185, 98]. In this case, the excitation decays to the lowest vibrational level in the triplet state and then decays to the ground state with the emission of phosphorescence.

2.1.3 Photoexcitation migration

In a real polymer chain, the photoexcitations are not delocalised over the entire chain, but rather over just a few repeat units of the backbone. Hence a conjugated polymer chain is visualised as a series of linked chromophores, each with a different extent of π-electron delocalisation[181]. Dynamic localisation of an excitation, due to feedback to the electronic system from the changed

positions of the nuclei, causes horizontal kinks and torsions in the chain to act as separators for spectral units[19]. This is shown at the top of Figure 2.2 where on a timescale of ∼1 ps, the kinks in the chain, combined with the nuclear motion, have partitioned the chain into conjugated segments[170]. On shorter timescales (<1 ps), the initially extended exciton localises on a shorter, more planar section of the polymer chain due to structural relaxation of excited segments along high frequency stretching modes of double and single carbon bonds[170].

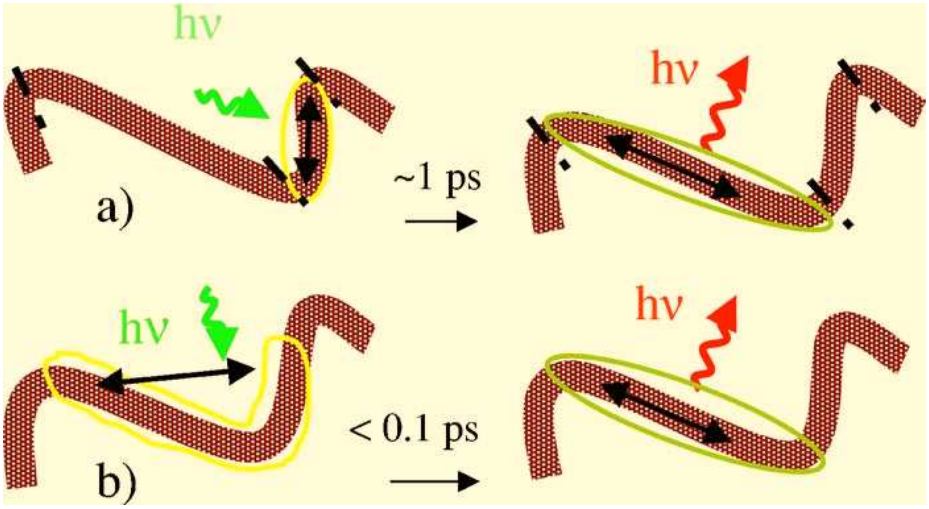

Figure 2.2: The polymer backbone is shown in brown. At longer times(>1 ps), exciton migration is mitigated by weak dipole-dipole coupling, while at short times (<100 fs), the exciton is localised on a bent conjugated segment. From [170].

Since excitons are neutral species, their motion is left unperturbed by any electric field, and they diffuse via random hops[116] between dipole-dipole coupled conjugated segments. If an exciton hops many times, its migration can be described using a random-walk based diffusion formalism[161]. If the mean free path of the exciton is short (∼1 lattice spacing), it

hops incoherently through the lattice and is scattered at each molecule[161]. The probability, however, that an exciton will spontaneously recombine (with the emission of a photon) limits the hopping time. There is a tendency for the excitons to diffuse to molecular regions with lower excitation or decay energy[197]. Each domain provides unoccupied states around the LUMO and HOMO level for electrons and holes, respectively. In a crude approximation, the temporal decay of the mean energy $\langle E \rangle(t)$ of photoexcitations generated at random within a Gaussian density of states should follow

$$\langle E \rangle(t) \sim \ln\left(\frac{t}{t_0}\right), \tag{2.4}$$

with the dwell time, t_0, characterising the average time for a single hop[115]. Förster resonance energy transfer is a single-step radiationless energy transfer process[58, 76]. As mentioned in Subsection 2.1.1, the energy can migrate along the backbone, referred to as intrachain migration, or between chains, referred to as interchain migration. Intrachain migration requires physical reorientation of the polymer segments to facilitate communication between regions of broken conjugation which takes time and is likely to be thermally activated. However, interchain energy transfer requires only physical proximity of conjugated segments that are strongly dipole-dipole coupled[181]. The Förster energy transfer mechanism will be described in detail in Section 2.4.

2.2 Self-assembly

Self-assembly, as pioneered by J.M. Lehn, and others, has fast become a staple tool used in the control of complex supramolecular systems [123, 124, 125]. When governed by molecular

recognition, self-assembly can produce systems with specific architectural and functional features determined by the interactions of the molecular components of the resulting aggregates [34, 184, 191]. The ensuant supramolecular systems are used as novel materials for devices, or as model systems in which to study properties such as energy transport or the effect of disorder in a system. It has even been proposed that organogels[35, 7, 218] self-assembling *in vivo* can regenerate optic tracts, resulting in vision recovery[78]. Typical interactions encountered in the supramolecular systems, such as hydrogen bonding, hydrophobic, hydrophilic and π-π interactions, are weak and highly temperature dependent. Other important factors are steric constraints and cooperative binding, wherein the interaction of one molecule with a macromolecular system increases the affinity for binding other molecules to this system [69]. Self-assembly is a particularly attractive technique because of the ease of sample preparation from solution to a drop-casted film, and the scope for up-scaling the technique to produce a large number of molecular nanostructures with well-defined morphologies [223].

2.2.1 Self-assembling impetus

Equilibrium thermodynamics requires that in an aggregated molecular system in solution, the chemical potential of all identical molecules in different aggregates be the same[89]. This requirement leads to[89, 102]

$$X_N = N\left[X_1 \exp\frac{(\varepsilon_1 - \varepsilon_N)}{k_B T}\right]^N, \tag{2.5}$$

where X_N is the volume fraction of solute molecules in an aggregate with N molecules, X_1 is the volume fraction of free solute molecules, ε_N is the free energy change when a molecule is

removed from the bulk and placed into an aggregate of N molecules, ε_1 is the free energy of an isolated molecule, k_B is Boltzmann's constant, and T is temperature. Hence, if $\varepsilon_N \geq \varepsilon_1$, most of the solute molecules will be present in solution as isolated molecules. On the other hand, aggregates will form if $\varepsilon_N < \varepsilon_1$ [102]. As a first approximation for micellar structures, ε_N, as a function of N, is determined by the geometric shape of the aggregate. Finite structures develop in lieu of phase separation, simply because for some N, ε_N is minimised[89]. More generally, self-assembly thermodynamics and intra-aggregate forces, such as those mentioned above, determine the equilibrium structures formed[89]. These self-assembled particles can coalesce over time[171], for example, so the molecular structure has to be designed carefully to prevent time-dependent changes of the system properties.

2.2.2 Scaffold incorporation

An additional aid in the design of self-assembled systems is the inclusion of a scaffold to fix the positions of the functional units, thereby aiding stability and reducing disorder, in these so-called "templated systems"[144, 12]. DNA is one example of a template found in nature as the formation of double-stranded DNA (dsDNA) is itself a cooperative self-assembly process [96, 41]. Since the advent of DNA origami, where long DNA scaffold strands are folded into designer shapes with the help of short staple strands [167, 223], DNA has been used as a scaffold to form complex shapes [51] and upon which nanoparticles and other materials may be bound with high reproducibility [151, 156]. DNA can act as a scaffold for assembly of pendant chromophores [140], chromophores bound in the minor groove [69], or chromophores incorporated between

the bases in single-stranded DNA (ssDNA) before hybridisation with the complementary ssDNA [68, 203]. More generally, hydrogen-bonding between specific nucleic bases has been utilized to form 'DNA-like' self-assembled stacked structures [90, 91]. These examples indicate that the properties of specific binding sites and of high monodispersity make DNA an attractive structure for arranging chromophores. Chromophores that harness the specific bonding mechanisms to DNA, such as multivalent guests that bond to DNA with high efficiencies [93], can be designed. This results in the synthesis of samples with specific packing orders that enhance the electronic and optical properties of a material [217].

2.2.3 Energy transport in templated systems

DNA-templated systems have been used in a multitude of ways, for example, as force sensors [186], molecular beacons [101], and molecular wires [173, 70]. All of these applications rely on dipole-dipole resonance energy transfer between luminescent dye molecules and much effort has thus been devoted to understanding and improving such processes. This mechanism was mentioned in Subsection 2.1.3 and will be discussed further in Section 2.4. For force sensors and molecular beacons, resonance energy transfer is detected in order to determine a change in distance between two dye molecules, a process which can be improved, e.g. by using a dye-quencher pair that can form a ground state complex [100, 101], or by using a fluorescent base analogue such as 2-aminopurine [189, 139] as one of the dye molecules. Molecular wires, on the other hand, are designed to allow energy to travel effectively between their ends – a process referred to as *energy transport*. Molecular wires are most commonly constructed from dsDNA to which

dyes are either covalently bound [173], or intercalated between the nucleic bases [70], or bound in the major or minor groove. However, efficiencies of energy transfer between the incorporated dyes are still limited by structural defects and varying conformations of the wire [173]. In addition, exact determination of the dye positions in the wires into which they are intercalated or groove bound is still difficult as the interchromophore distance is a function of the intercalator density [70]. Furthermore, intercalation by large dye molecules leads to local DNA-unwinding sites which can affect the structural integrity of the DNA [70]. These problems have been surmounted through the design of a new DNA-scaffolded supramolecular structure. This structure will be examined in detail in chapters 4 and 5.

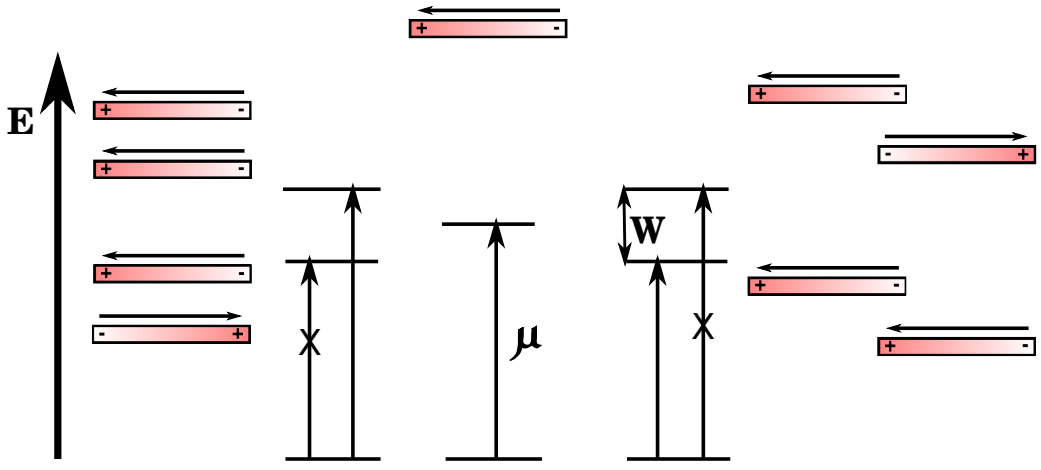

Figure 2.3: H- and J-aggregates at left and right of diagram, respectively. The optical splitting between the allowed transitions in both aggregates is W. From Ref. 42.

2.3 Interchain interactions

The intermolecular forces between molecules in a solid are highly directional and spatially complex, being based on the overlap of the frontier π-molecular orbitals between adjacent molecules[116]. A small distance change between adjacent molecules can cause their wavefunctions to move in or out of phase with one another. This can drastically affect the bandwidths and, hence, the emission wavelength of the structure[67]. Thus, it is important to understand and control the intermolecular forces in a device based on π-conjugated structures.

2.3.1 General considerations for dimers

Interchain coupling can be explained by molecular exciton theories in terms of dipole coupling of segments approximating the Coulomb potential[110]. The simplest case is that of a cofacial dimer in which two chains are separated by an interchain distance d[111]. The total Hamiltonian of this system is[42]

$$H_{\text{tot}} = H_1 + H_2 + H_{12}, \tag{2.6}$$

where H_x is the Hamiltonian of isolated chain x and H_{12} describes the interchain interactions. The Hamiltonian of the interchain interactions is a slight perturbation of the system[158, 42] and so, at first order, can be neglected. Accordingly, the interaction of the lowest energy optically-allowed excited state of the chains leads to

$$\Psi^{\pm} = \frac{1}{\sqrt{2}}(\Psi_1^* \Psi_2 \pm \Psi_1 \Psi_2^*), \tag{2.7}$$

where Ψ_x^* is the lowest excited state and Ψ_x is the ground state of chain x[42]. In a cofacial dimer the lowest excited state of the dimer corresponds to the antisymmetric combination of the wavefunctions, i.e. Ψ^-, shown on the left of Figure 2.3. The two dipoles effectively "cancel out" and the lower excited state becomes optically forbidden. The whole oscillator strength is concentrated in the higher excited state, Ψ^+, instead[42]. This is known as a H-aggregate[110, 39]. The energy splitting between the two excited states, as estimated from first-order perturbation theory is[42]

$$W = \langle \Psi^+ | H_{\text{tot}} | \Psi^+ \rangle - \langle \Psi^- | H_{\text{tot}} | \Psi^- \rangle, \tag{2.8}$$

which is the difference between the energies of the symmetric and antisymmetric combinations.

In polymers with transition dipole moments in head-to-tail, parallel (right and left of Figure 2.3, respectively), and oblique arrangements, an N-fold exciton degeneracy exists before excited-state interactions. The intermolecular dipole-dipole interaction of transition dipoles causes an electrostatic perturbation which produces an exciton band of N discrete exciton states. However, only one or very few of the available exciton states are optically allowed[110]. For the head-to-tail case, the highest-energy exciton band component corresponds to excitation nodes between each molecular unit with a net transition moment of zero. This corresponds to a repulsive electrostatic interaction between each transition dipole. Hence, this exciton state is forbidden[110, 111]. Therefore J-type aggregates correspond to a spectral redshift[7, 38]; H-type aggregates, a spectral blueshift[48, 79]. The so-called "dark" states are important because if a triplet level lies below a forbidden lowest exciton level in an exciton band, greatly enhanced

triplet-state excitation can occur. The normal singlet-state emission of the molecule will be totally quenched in this case[110].

2.3.2 Interchain species and their spectral signatures

Aggregates occur when the π-electrons of conjugated molecular systems are neutrally delocalised over multiple segments in both the ground and excited states, i.e. the extent of π-delocalisation is significantly altered from that of a single chromophore[181]. If the π-electrons are shared equally in the excited state but not in the ground state, the interchain species is termed an excimer. Such an excited state complex is stable as a result of resonance contributions from exciton and charge-transfer configurations: $^1(A^*A) \leftrightarrow {}^1(AA^*) \leftrightarrow {}^1(A^-A^+) \leftrightarrow {}^1(A^+A^-)$, where A is a chromophore. The relative contributions (to the excimer wave function) from exciton and charge transfer may vary for different materials[99]. A polaron pair is a charge-separated interchain species with a radical cation (hole polaron) on one segment and a radical anion (electron polaron) on the adjacent segment. Two different molecules sharing an interchain excited state with a partial degree of charge transfer character is referred to as an exciplex[181]. This complex is only stable in the excited state[99].

In general, photoluminescence spectral redshifts[129, 215, 130, 27, 220, 212, 20] betray the presence of interchain interactions in a molecular system. Energy funnels very efficiently to the lowest energy segments, formed by electron delocalisation across adjacent chains, where a long-wavelength photon is released[81, 38]. A large Stokes shift can result from the stabilisation

energy of $\sim$ 0.5 to 0.7 eV of the interchain species in oligomer thin films[99]. Long radiative lifetimes of the delocalised interchain excited state, taken with the multitude of nonradiative deexcitation pathways available, lead to low quantum yields for the interchain emission[181]. The number of interchain species present in a π-conjugated sample can be changed upon forming a film from a solution, annealing the film, changing casting solvents, and changing the sample temperature[181]. Strategies to stop interchain species forming include threading the oligomer backbone with nonconjugated insulating macrocycles via hydrophobic interactions during polymerisation[33] and changing the oligomer side chains.

2.3.3 The effect on lifetimes

As mentioned in Subsection 2.3.2, the lifetime of the interchain species can differ sharply from that of the monomer species. This was studied for stilbene molecules occurring as cofacial dimers in Ref. 43. It was found that the interaction strengths depend intricately on the relative strengths of the overlap between the wave functions of the adjacent molecules. For an intermolecular separation greater than 7 $\AA$, there is only weak coupling of the molecular orbitals. The situation is as in the left of Figure 2.3 where the transition between the lowest excited state to the ground state is forbidden and the excitation is localised on only one of the weakly-coupled molecules at any time. Below a chain separation of $\sim$7 $\AA$, the molecular orbitals of the dimer start to delocalise over the two chains, such that they are strongly coupled. Correlated quantum-chemical calculations[43] suggest that the first excited state in a dimer is self-localised, i.e. possesses strong intrachain character, where the electron is located close to the hole in the

centre of the chain. The probability of finding the exciton on the second chain, or of creating an interchain exciton, is low but increases exponentially as the distance between the chains diminishes. Hence, even at short distances, the equilibrium geometry in the lowest excited state is not symmetric with respect to the two chains. This relaxes the selection rules and a small transition dipole moment between the ground state and the lowest excited state exists and is redshifted with respect to that in the isolated molecule. Hence, increases in radiative lifetimes upon aggregation formation[126] are due to weak coupling between the ground and the (redshifted) lowest excited states, yielding small radiative decay rates, or the migration of excitations toward regions where the molecules are of lowest energy before emission of a photon occurs[42, 43].

2.4 Mechanisms of energy transfer

In Subsection 2.2.3, resonance energy transfer between self-assembled chromophores in a DNA scaffolded system was shown to be crucial to their use. Hence, an in-depth understanding of such transfer processes is important.

2.4.1 Excitonic coupling

The most general expression for the rate of energy transfer between an excited donor and a ground-state acceptor, k_{DA}, can be derived from time-dependent perturbation theory and the

Fermi golden rule[120]:

$$k_{D^* \to A^*} = \frac{1}{2\pi} |V_{AD}|^2 \int \alpha_A(\omega) f_D(\omega) d\omega \tag{2.9}$$

where V_{AD} is the excitonic coupling matrix element and the spectral overlap is between the donor's emission $f_D(\omega)$ and the acceptor's absorption $\alpha_A(\omega)$. In Förster's approach, the excitonic coupling is represented by a multipole interaction between the transition dipoles, each located at the centre of the respective molecule, truncated after the dipolar term (point-dipole approximation)[120]. An alternative mechanism to Förster resonance energy transfer is Dexter-type energy transfer. The electronic coupling (V_{DA}) is dominated, in this case, by electronic exchange interactions mediated by the overlap between donor and acceptor orbitals. Hence, the energy transfer depends heavily on distance: e^{-d}, where d is the donor-acceptor distance[120, 82, 121].

2.4.2 Förster energy transfer between a donor-acceptor pair

Based on the weak coupling limit of radiationless transitions, Förster[59] derived the rate constant for the transfer process involving a single donor-acceptor pair to be

$$K_{D^* \to A^*} = \frac{1}{\tau_D} \left(\frac{R_0}{R} \right)^6, \tag{2.10}$$

where τ_D is the mean lifetime of the excited donor, R_0 is the critical transfer distance for which excitation transfer and spontaneous deactivation are of equal probability, and R is the distance between the donor and the acceptor species[58, 59, 75]. Equation 2.10 implies that the transfer rate is independent of exciting wavelength, and is thus only valid if the donor molecule is in the

lowest vibrational level of its excited state[22]. Also, the size of the molecules is restricted to being smaller than intermolecular separations when such point-dipole models are used to calculate the electronic coupling that promotes energy transfer from one molecule to another[22, 153].

The Förster radius, R_0, is calculated from[59, 153, 22, 75]

$$R_0 = \left[\frac{9000 \ \ln 10}{128\pi^5} \frac{\kappa^2 \phi_D}{n^4 N} \int_0^\infty \frac{1}{\overline{\nu}^4} \ f_D(\overline{\nu}) \ \varepsilon_A(\overline{\nu}) \, d\overline{\nu} \right]^{\frac{1}{6}} \tag{2.11}$$

where the dipole orientation factor is κ^2, ϕ_D is the fluorescence quantum yield of the donor in the absence of energy transfer, n is the refractive index of the material at the peak of the integrand, N is Avogadro's constant, $f_D(\overline{\nu})$ is the fluorescence spectrum of the donor with integrated intensity normalised to unity on a wavenumber scale, and $\varepsilon_A(\overline{\nu})$ is the molar decadic extinction coefficient of the acceptor. The dipole orientation factor incorporates the relative directions of the acceptor and donor transition dipole moments through[50]

$$\kappa^2 = \left[(\vec{d} \cdot \vec{a}) - 3(\vec{d} \cdot \vec{r}) \ (\vec{a} \cdot \vec{r}) \right]^2 \tag{2.12}$$

where $\vec{d}$ is the vector in the direction of the donor transition dipole moment, $\vec{a}$ is the vector in the direction of the acceptor transition dipole moment, $\vec{r}$ is the vector that connects the centres of the two transition dipole moments, and the length of each of the vectors $\|\vec{d}\|$, $\|\vec{a}\|$, and $\|\vec{r}\|$ is equal to 1.

2.4.3 Kinetic rate equations and transfer efficiency

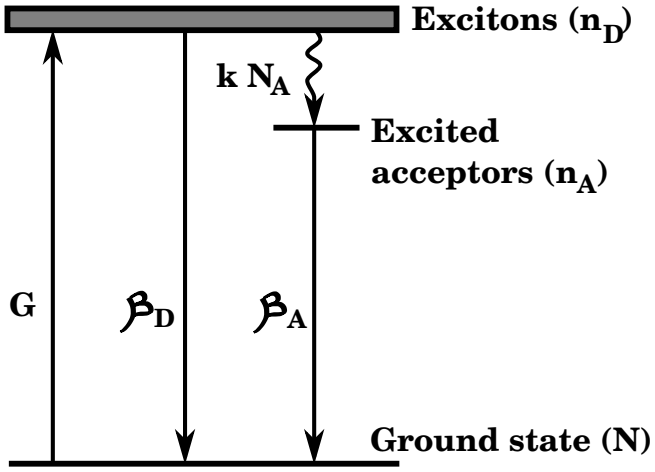

Figure 2.4: A schematic of the singlet energy state $\hbar\omega_D$ of the donor and of the acceptor $\hbar\omega_A$. Adapted from Ref. 161.

From Figure 2.4, the intensity of the donor fluorescence, at frequency ω_D, is proportional to n_D, the number of excited donors created by exciting the π-conjugated system. Correspondingly, the acceptor fluorescence, at $\hbar\omega_A$, is proportional to n_A, the number of excited acceptors. It is assumed that there are many more donors (N_D) than acceptors (N_A), and many more acceptors than excitons (n_D). Hence, direct excitation of the acceptors, and exciton-exciton collisions and other biexciton effects are neglected. These conditions lead to a set of rate equations

$$\frac{\mathrm{d}\, n_D(t)}{\mathrm{d}t} = G(t) - \beta_D\, n_D(t) - k(t)\, n_D(t) \tag{2.13}$$

$$\frac{\mathrm{d}\, n_A(t)}{\mathrm{d}t} = k(t)\, n_D(t) - \beta_A\, n_A(t) \tag{2.14}$$

where β_D $(=\tau_D^{-1})$ and β_A $(=\tau_A^{-1})$ are the fluorescence decay rates — inclusive of radiative and nonradiative processes but in the absence of energy transfer — for the donor and the acceptor, respectively, $G(t)$ is the generation rate of donor excitons, assumed to be proportional to the

instantaneous intensity of the excitation pulse, and k is the energy-transfer probability per unit time[161, 159, 160].

Equations 2.13 and 2.14 can be used to describe the kinetics of the fluorescence intensity for the dipole-dipole model where the donors and acceptors are distributed randomly in space[160]. For a δ-function excitation at time $t_0 = 0$, the number of excited donors created is

$$n_D(N_A,t) = n_D(0)\exp\left[-\beta_D t - \int_0^t k(t')\mathrm{d}t'\right] \tag{2.15}$$

where $n_D(0)$ is the initial excited donor concentration[161]. Here, $k(t)$ is time-dependent which arises from its donor-acceptor separation dependence. The efficiency of energy transfer thus decreases with time[159, 114, 137]. Assuming that the time-dependence of $k \propto t^{-1/2}$ (see Subsection 2.4.4), the last term of Equation 2.15 can be integrated[161]. The integral of $n_D(N_A t)$ over time yields the donor fluorescence intensity $I_D(\gamma)$

$$I_D(\gamma) = I_D(0)\left[1 - \pi^{1/2}\gamma\exp[\gamma^2]\ \mathrm{erfc}(\gamma)\right] \tag{2.16}$$

where $\gamma = \dfrac{\sqrt{\pi}}{2}\dfrac{C_A}{C_0}$, C_A is the concentration of acceptors, C_0 is the "critical concentration" defined as $C_0 = (4/3\pi R_0^3)^{-1}$, and the complementary error function $\mathrm{erfc}(\gamma) = 1 - \left(\dfrac{2}{\sqrt{\pi}}\right)\displaystyle\int_0^\gamma \exp(-u^2)\mathrm{d}u$[161, 204, 160, 74]. The average number of acceptor molecules in a sphere of radius R_0 is represented by $4/3 C_A \pi R_0^3$[204]. Similarly the fraction of photons emitted from the acceptor is

$$I_A(\gamma) = I_A(0)\,\pi^{1/2}\gamma\exp[\gamma^2]\ \mathrm{erfc}(\gamma). \tag{2.17}$$

2.4.4 Förster energy transfer in a donor-acceptor ensemble

The energy transfer needs to be extended from transfer between single donors and acceptors to transfer between ensembles of donor and acceptor molecules. The survival probability $G(t)$ of the donor molecule, i.e. the probability that the donor is still excited at time t after excitation at $t_0 = 0$, is the sum over all possible rate constants k_{DA}; see Equation 2.10. For a random distribution of donors and acceptors, the time dependent $n_D(t)$ and $n_A(t)$, derived from equations 2.13 and 2.14, are[161, 160]

$$n_D(t) = n_D(0)\exp\left[-\beta_D + t - \gamma(\pi\beta_D t^{1/2})\right] \tag{2.18}$$

$$n_A(t) = \gamma\beta_D^{1/2}\exp\left[-\beta_A t\right]\int_0^t \exp\left[\beta_A\xi\right] n_D(\xi)\,\xi^{-1/2}\mathrm{d}\xi, \tag{2.19}$$

where γ is defined as in Subsection 2.4.3. From this, the time-dependent transfer rate for the donor-acceptor ensemble (DAE) is extracted as

$$k_{DAE}(t) = 2\gamma\beta_D^{1/2}t^{-1/2}. \tag{2.20}$$

Excited donors located in proximity to acceptors transfer their energy and have a swift decline in number compared to those farther away. Hence, the random distribution of donors and acceptors present at time $t_0 = 0$ becomes less random with elapsing time, as fewer excited donors reside near acceptors. Hence, the characteristic $t^{-1/2}$ time dependence for energy transfer from randomly distributed immobile donors to randomly distributed immobile acceptors describes a slower and slower rate of energy transfer as the excitations near each acceptor become depleted[161, 160].

2.4.5 Dimensionality

The fluorescence of a donor molecule surrounded with n acceptor molecules distributed at random in a large spherical volume ($R_{\text{sphere}} \gg R_0$), can be described by[204]

$$i_D(t) = i_D(0)\exp\left[-\frac{t}{\tau_D} - 2\gamma\left(\frac{t}{\tau_D}\right)^{1/2}\right], \tag{2.21}$$

also, where i_D and $i_D(0)$ describe the fluorescence intensity at a time t and at $t_0 = 0$, respectively, and τ_D and γ have been defined previously. This equation is valid for randomly distributed acceptors in three dimensions. If the dimension is less than three, the equation must be generalised to

$$i_D(t) = i_D(0)\exp\left[-\frac{t}{\tau_D} - 2\gamma\left(\frac{t}{\tau_D}\right)^{d/6}\right] \tag{2.22}$$

where d is dimension 1, 2, or 3 and γ is given by $\gamma = \frac{\Gamma(1-d/6)}{2} C_A V_d R_0^d$. Here, V_d is the volume of the unit sphere of dimension d ($V_1 = 2$; $V_2 = \pi$; $V_3 = 4\pi/3$), and Γ is the gamma function[204].

Chapter 3

Experimental procedure

Laser spectroscopy can be used to probe the responses of matter to light. Time-integrated photoluminescence (TIPL) spectroscopy and time-correlated single photon counting (TCSPC) are invoked in subsequent chapters to elucidate fundamental properties of supramolecular assemblies. In this chapter, the pertinent features of these procedures and their experimental implementation are elucidated.

3.1 Time-integrated photoluminescence

Time-integrated photoluminescence (TIPL) spectroscopy has become a fundamental tool in the characterisation of basic properties of newly-synthesised materials. Intensities and frequencies of energy-level transitions; the presence or absence of vibronic features; peak shifts upon changing sample conditions; e.g. temperature or type of solvent; and other quantitative and qualitative

information can be detected using TIPL spectroscopy.

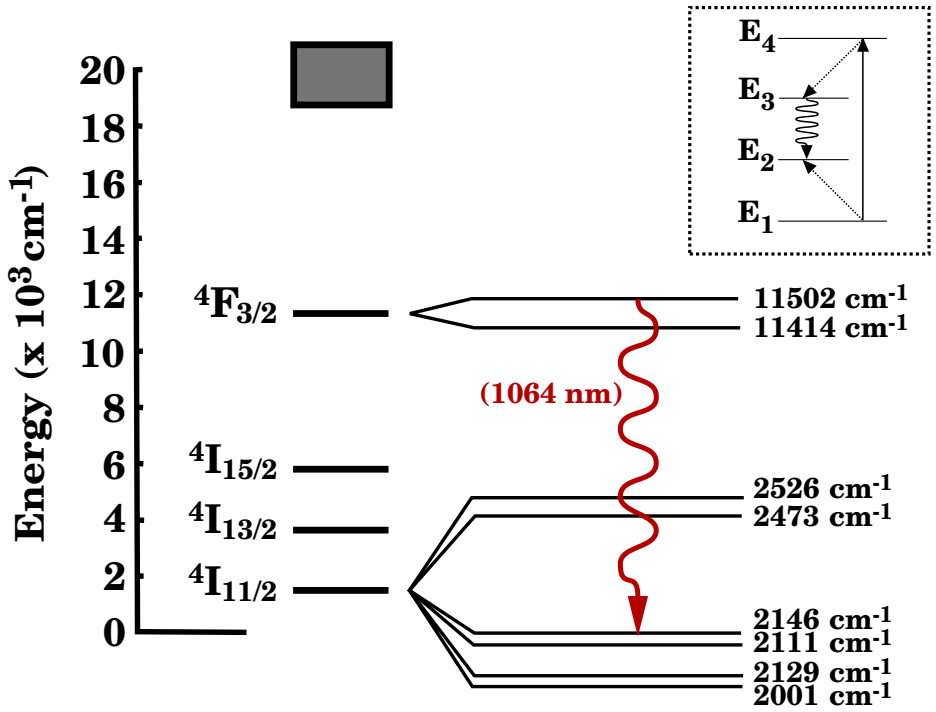

Figure 3.1: The Nd^{3+} energy levels in a yttrium vanadate crystal. A schematic diagram of a four-level laser system is shown in the inset. Adapted from Ref. 193.

3.1.1 Pump laser

To measure a compound's photoluminescence (PL) spectrum, a tunable, monochromatic, stable excitation source is necessary. In this case, the source is a Ti:Sapphire *Tsunami* laser pumped by a solid-state *Millennia* laser. In the *Millennia* pump laser, the active material — that is, a material that amplifies light under favourable conditions — is a neodymium yttrium vanadate crystal ($Nd:YVO_4$). Population inversion[169] can occur in the crystal because the ground and excited energy levels of the doped Nd^{3+} ions form a so-called "four-level system".

The inset in Figure 3.1 shows a four-level laser system. For population inversion to occur, the electronic decay from the excited state (E_4) to the metastable E_3 energy level, and the deexcitation of state E_2 must occur on very short timescales. Hence, the relatively long-lived E_3 level is over occupied and stimulated emission can occur from this state[169]. The energy levels in Figure 3.1 refer to the Nd^{3+} ion. The grey states at high energy are the absorption bands. Photoexcitations quickly drop to the $^4F_{3/2}$ level where they are long-lived ($\sim$60 μs[193]). The lasing transition (highlighted in red) to the $^4I_{11/2}$ state occurs with emission of a 1064 nm photon[63].

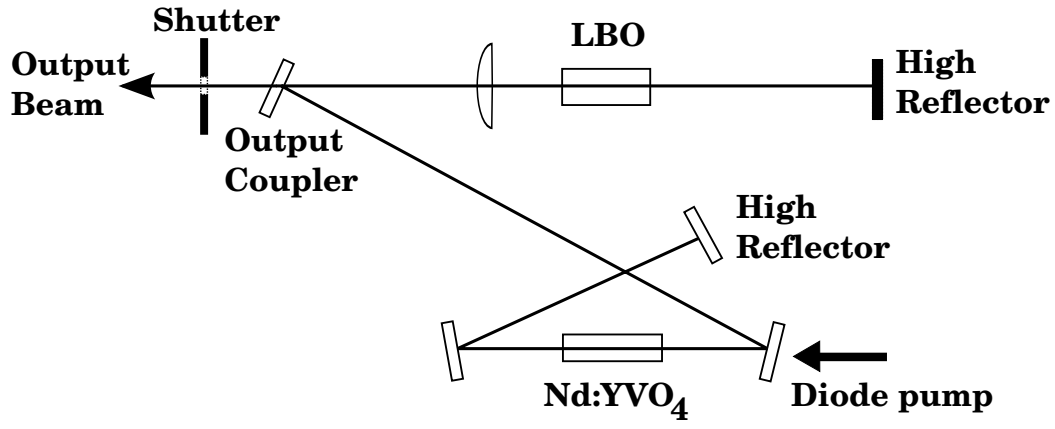

Figure 3.2: The X-shaped cavity of the *Millennia* pump laser. Adapted from Ref. 193.

To sustain the lasing action, the active medium is kept within a cavity; see Figure 3.2. The Nd:YVO_4 crystal is end-pumped with a 40 W fibre-coupled diode bar, hence emitting 1064 nm[193]. This light is resonated in the cavity, amplified, and frequency doubled to 532 nm in a non-critically phase-matched, temperature-tuned lithium triborate (LBO) crystal[193]. The

resulting green beam is directed out of the laser and used to pump a Ti:Sapphire *Tsunami* laser.

3.1.2 Frequency doubling

Second harmonic generation in a nonlinear crystal produced frequency-doubled green light as the *Millennia's* output. The nonlinear LBO[187] crystal has a similar bond structure to BBO[53] and has the double advantage of a high nonlinear coefficient and a high damage threshold. In classical physics, light sets into motion oscillations of harmonic electronic dipoles. These dipoles coherently re-emit the light and, in turn, light propagates through the material[169]. However, when the light excitation energy is extremely high the oscillators become strongly anharmonic. This so-called "dipole approximation" is the polynomial expansion of the macroscopic polarisation of the material, namely

$$\mathbf{P} = \chi^{(1)}\varepsilon_0 \cdot \mathbf{E} + \chi^{(2)}\varepsilon_0 \cdot \mathbf{E}\mathbf{E} + \ldots \tag{3.1}$$

where $\mathbf{E}$ is the applied electric field, ε_0 is the permittivity of free space, $\chi^{(1)}$ is the linear susceptibility of the material, and $\chi^{(2)}$ is the second-order susceptibility tensor that governs second-harmonic generation[169]. This tensor depends on the orientation of the optic axis and the polarisation of the electric field[219]. When two photons that have the same angular frequency (ω) propagate through a suitable material, second harmonic generation occurs as the photons mix together to get a single photon with twice the frequency of the original photons. For the ideal case of a plane wave propagating in a material, the intensity of the second harmonic

$I(2\omega)$ is

$$I(2\omega) = A\omega^2 \chi^{(2)}_{eff} l^2 I^2(\omega) \left(\frac{\sin\left(\frac{\Delta kl}{2}\right)}{\left(\frac{\Delta kl}{2}\right)} \right)^2 \tag{3.2}$$

where $I(\omega)$ is the incident intensity, A is a constant that depends on the index of refraction, l is the length of material, $\chi^{(2)}_{eff}$ is the material-dependent effective susceptibility, and k is the wavenumber[169]. After propagating a distance l in a crystal, the dephasing quantity $\Delta kl = (k_2 - 2k_1)l$, where k_1 and k_2 are the wavenumbers of the fundamental and second-harmonic beam respectively[154], must be equal to zero for constructive interference to occur[169]. This is known as the phase matching condition. Dephasing is overcome by propagating the light waves in a birefringent crystal where the index of refraction is directionally dependent.

3.1.3 Laser tunability

The Ti:Sapphire *Tsunami* is the laser used in the experiment to excite the sample because of its broad tuning range, large gain cross section, good thermal conductivity, large bandwidth, and high repetition rate[174, 108, 194]. The active medium is composed of a Al_2O_3 crystal where the Al^{3+} ions are replaced, at certain sites, by Ti^{3+} (titanium) ions. The 5-fold degenerate 3D-electron energy levels of the Ti^{3+} ion are split by the crystal field of the Al_2O_3 host and spin-orbit coupling into a doubly degenerate ground state and a doubly degenerate first excited state[143, 194]. There is strong coupling between the vibrational energy states of the Al_2O_3 host and the electronic energy states of the active Ti^{3+}[61]. Hence, the doubly-peaked vibrationally-broadened fluorescence spectrum (600-1000 nm) of the Ti^{3+} ions yields a large tun-

ing range[8][1]. The tuning length depends on the laser cavity properties, for example, the mirror coatings[143, 8, 194].

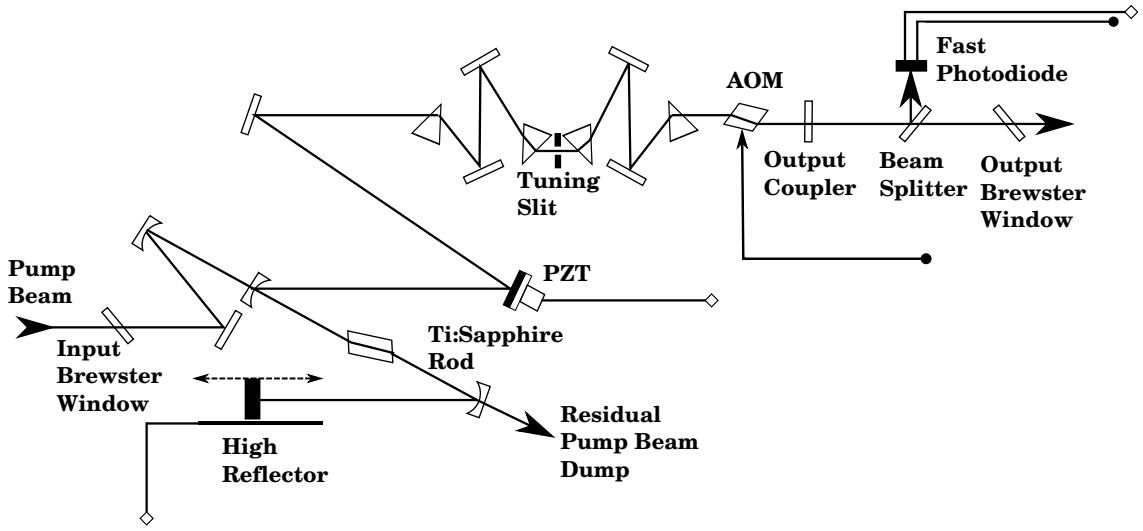

Figure 3.3: The cavity of the Ti:Sapphire laser. The prism dispersion/slit wavelength selector assembly, the high reflector, and the output coupler can be manually adjusted by the user. Adapted from Ref. 194.

To achieve lasing from the Ti:Sapphire cavity upon continuous-wave (CW) pumping using the *Millennia* Nd:YVO_4 laser, the unsaturated round-trip CW gain must be greater than the round-trip loss[194]. A high gain is attained when the density of Ti^{3+} ions in the laser crystal is high and the pumping and cavity oscillating mode overlap is high. In Figure 3.3, the Brewster-angled Ti:Sapphire rod is shown positioned to the left-hand side of the 10-mirror cavity[194]. The laser medium is long because of the small pump absorption cross section of Ti:Sapphire[107]. The folded cavity arrangement is needed because of the high repetition rate

[1]The fluorescence decay time at 300 K is $\sim$3.2 μs[143, 8].

of the laser ($\sim$80 MHz = 3.75 m). The pumping beam enters the cavity through an input Brewster window. This beam and the oscillating laser mode are focussed and overlapped through a narrow volume in the active medium[194, 107], while the residual pump beam is dumped at the second cavity focus mirror. Using a small volume of the active medium maintains the large gain by reducing energy scattering loss in the rod. It is necessary also to match the astigmatism[2] in the cavity mode, induced by the Brewster-angled rod, by introducing astigmatism into the pump beam through use of an appropriately-angled concave mirror[194, 175, 107]. The resultant output beam is collimated and expanded to normal size.

Ultrashort pulses are produced using a regenerative mode-locking technique[3]. A Brewster-angled acousto-optic modulator (AOM, see Figure 3.3), driven by a radio-frequency (RF) signal derived from the cavity, introduces into the cavity controlled loss through diffraction[107]. The intense, short pulses produce nonlinear effects in the long laser crystal such as self-phase modulation[194]. Also, extra positive group velocity dispersion (GVD), above that from the other optical components, is introduced into the cavity. Prism pairs compensate for this effect by producing negative GVD so that subpicosecond pulses can be generated. This will be discussed further in Subsection 3.1.4. The wavelengths of the light are spatially spread by the prism pairs. By translating a slit in the middle of the prism pair, the output light wavelength is tuned. The width of the slit affects the bandwidth of the output pulse[194]. An overall tuning

[2]Astigmatism is where the position of the minimum laser beam radius is different for different transverse directions[154]. It needs to be compensated for to maintain high gain.

[3]Mode-locking is initiated by causing a sudden cavity-length change such as translating an intracavity prism, moving an external cavity mirror, or tapping on the laser lid[107].

range of the combined *Millennia* (5.5 W pump power) and Ti:Sapphire *Tsunami* laser assembly from 736 nm to 950 nm was achieved with a pulse width of 100 fs.

3.1.4 Short-duration pulses and mode-locking

Ultrashort pulses, on the order of femtoseconds, are important for the investigation of molecular short-time phenomena and of the dynamics of physical, chemical, and biological processes[196, 61]. The typical instantaneous intensity-fluctuating multimode[4] output of a laser consists of resonance frequencies of the cavity for which the optical amplification (gain) is greater than the cavity losses[169, 61]. The gain-bandwidth, i.e. the width of the frequency range that can be amplified, which depends on the atomic energy levels of the laser medium[194], is inversely related to pulse duration by the uncertainty principle[61, 194]. Hence, the minimum requirement for the generation of short pulses is that the spectral bandwidth must be broad. To obtain the ultrashort high intensity laser pulse, the phase differences between the modes are fixed, so-called mode-locking. This yields a succession of single pulses with a repetition rate of $2L/c$, where L is the cavity length[194, 61, 169].

Although many mode-locking techniques exist, the method utilised in the Ti:Sapphire *Tsunami* laser is regenerative mode-locking[194]. Mode-locking requires that a type of modulation (periodic loss) be applied to the laser radiation which has a period equal to the cavity round trip time[61, 169, 107]. The advantage of regenerative mode-locking is that the frequency

[4] There can be as many as 10^4 oscillating modes in a Ti:Sapphire laser[169].

used to drive the modulator is derived from the laser cavity so that if the laser cavity length changes slightly, the driver frequency adjusts accordingly. Figure 3.3 shows the amplitude modulator (AOM) to the left of the output coupler. A piezoelectric transducer is attached to one of the AOM's surfaces and, together with reflection from the AOM's surfaces, produces a standing acoustic wave within the modulator at the cavity-derived RF frequency[54]. Hence, a time-dependent refractive index grating perpendicular to the light propagation direction is produced[194]. Upon interaction of the laser light with this grating, some of the light is diffracted out of the cavity which introduces the necessary time-dependent loss[194]. The initial jumble of longitudinal modes are partially phase-locked by the AOM which produces mode beating. This beating signal is detected, amplified, divided by two, reamplified, and fed to the modulator. Hence, the modulator will always have a maximum in transmission when the pulse is present[107]. The AOM is run off resonance with a diffraction efficiency to 1%[194]. To achieve the shortest possible pulses, however, pulse broadening effects in the cavity need to be compensated for.

The two primary causes of pulse broadening are group velocity dispersion (GVD) and self-phase modulation (SPM). GVD occurs because the index of refraction of any material is frequency dependent. Each frequency in the pulse experiences a slightly different index of refraction which, in turn, affects the velocity of each frequency, and causes a spreading of the pulse[61]. Pulses acquire a positive chirp (low leads the high frequencies) as they pass through materials in the cavity at visible and near-IR wavelengths[194]. SPM results from the nonlinearity of the refractive indices of intracavity media at high pulse intensities, due to the optical Kerr

effect[61, 169]. As the pulse propagates through the Ti:Sapphire material, the leading edge experiences a higher and higher index of refraction. This causes a delay in the individual oscillations of the electric field, resulting in a broadened, positively-chirped pulse[194]. These effects can be counter-acted by introducing prism-pairs into the beam. These prism-pairs provide negative group-velocity dispersion that is both low loss and easily adjusted from negative through to positive values, and occurs with no transverse displacement of the temporally dispersed rays[56, 107, 194]. Using these techniques, Ti:Sapphire lasers have generated pulses as short as 8 fs[61], while the laser described here produces pulses of ∼100 fs.

3.1.5 Experimental details

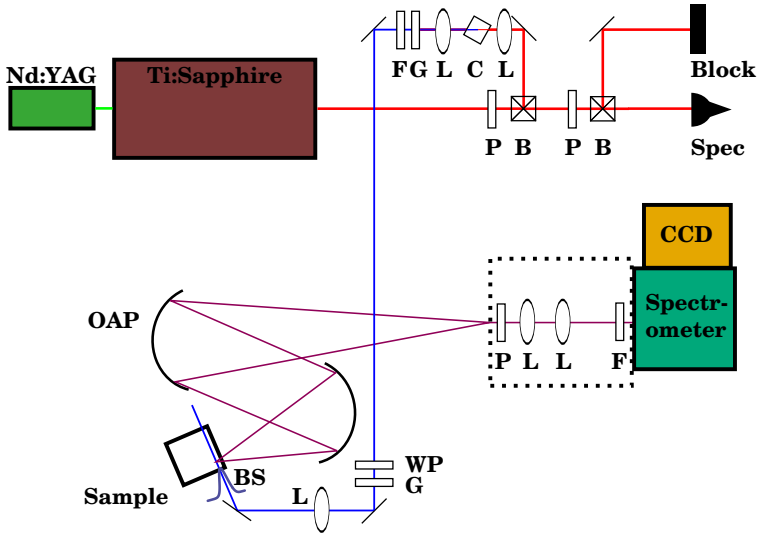

Figure 3.4: Schematic diagram of the laser setup used to capture time-integrated photoluminescence.

To measure time-integrated photoluminescence of a sample, the setup in Figure 3.4 is used. The pulsed red laser light emerging from the Ti:Sapphire laser is split at the first beam-splitter (B) into an excitation and gate beam. The gate beam is further split to provide the spectrometer (Spec) with an intensity fraction so that the beam profile can be monitored. The rest of the beam is dumped (Block). The excitation beam is frequency doubled using a set of two lenses (L) and a BBO crystal (C). The filter (F) and Glan-Thompson (G) prism[154] remove any residual red laser light from the excitation beam. The Glan-Thompson and half-wave plate (WP) combination before the sample allow adjustment of the beam's polarisation direction and power. The excitation beam enters the cuvette near to its right edge and the emerging photoluminescence is collected by two off-axis parabolic mirrors (OAPs) along a trajectory orthogonal to the excitation.

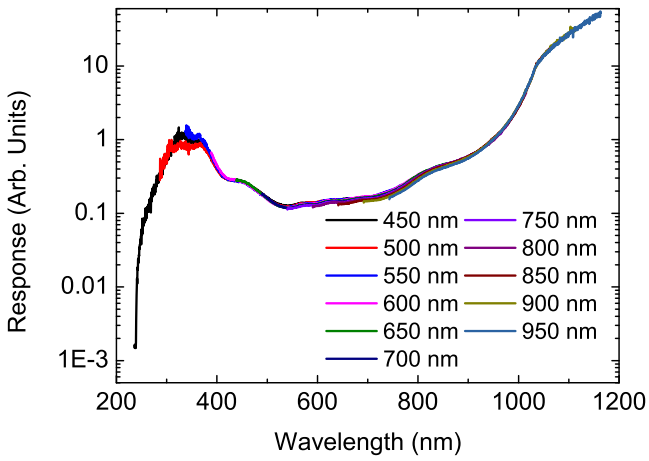

Figure 3.5: Response curves for the spectrometer/CCD combination acquired using a lamp of known spectral distribution. The listed wavelengths are the central wavelength for each response curve. The extracted photoluminescence spectra are corrected using these curves[152].

This trajectory reduces fluorescence reabsorption errors[14]. The photoluminescence is collimated, dispersed in a monochromator, and imaged onto a nitrogen-cooled charge-coupled device (CCD). The TRIAX 190 spectrometer can present one wavelength at a time from its exit slit, or a range of wavelengths at the exit focal plane for detection by an array detector[207]. The CCD has a 26 μm$\times$26 μm pixel size, and a 26.6 mm$\times$6.7 mm imaging area, a low dark current, and a relatively flat response from 250 nm to 900 nm with an average quantum efficiency of 40%[206]. The response curves for the spectrometer/CCD combination are presented in Figure 3.5.

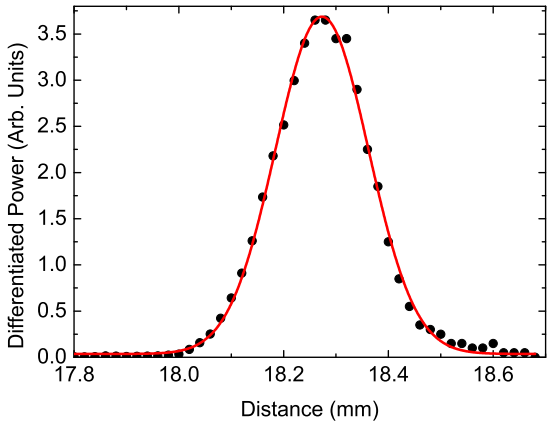

Figure 3.6: Beamwidth measurement. Experimental data (black dots) and Gaussian fit (red line).

The beam width at the sample stage is 210 μm (FWHM), see Figure 3.6, and was measured using a knife-edge method. A knife edge is moved perpendicular to the direction of propagation of the laser beam while the total transmitted power is measured as a function of the knife-edge position[47]. The resulting length-dependent power plot was differentiated and fitted with a Gaussian function to get the FWHM. The measurement was repeated for different laser powers.

3.2 Time-Correlated Single Photon Counting

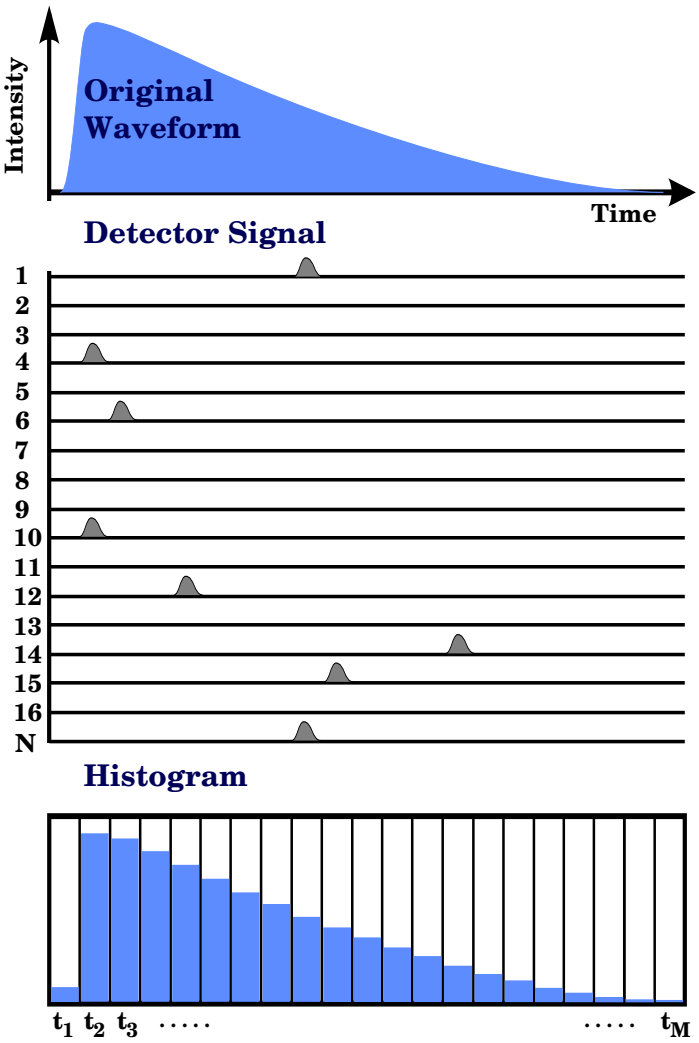

Figure 3.7: The principle of time-correlated single photon counting apated from Ref. 16. The number of times the detector is triggered into searching for a photon (depicted as grey pulses) is N. N is large enough such that a low-noise histogram, partitioned into identical time channels $t_1, t_2, \ldots, t_M$ ($M \sim 10^3$) where each t corresponds to a different photon arrival time, is acquired.

Time-resolved spectroscopy is the study of dynamical processes, such as energy transfer, in materials by means of spectroscopic techniques. These processes occur over very short timescales, e.g. electronic relaxation, nuclear relaxation and charge transfer all occur in molecules on a timescale of between one femtosecond and one nanosecond[74, 182, 196, 182]. The time-correlated single photon counting (TCSPC) technique does not suffer from gain noise or electronic noise and has a higher time-resolution than any analogue recording method[16].

3.2.1 General principle

A reference pulse from the laser ("start pulse") triggers the start of a timer in the TCSPC electronics. The timer stops when fluorescence photons from the laser-excited sample impinge on a fast detector ("stop pulse"). The arrival of single fluorescence photons in the detector channel at a certain time is illustrated in Figure 3.7. As the experiment is repeated and the number of photons sensed reaches N, where N is a suitably large number, a histogram of the photon arrival times is constructed. This reflects the photoluminescence (PL) decay of the original waveform — compare the top and bottom of Figure 3.7. Multiple measurement cycles is implemented easily through the use of a pulsed laser. However, the probability of registering more than one photon per measurement cycle must be low so that later arriving photons in the same detection period are not missed, leading to an over-representation of early time photons and a distorted PL decay waveform[155, 16]. This is achieved by attenuating the light level at the sample[155]. In modern high-repetition rate systems, the start-stop pulses are reversed, i.e. a fluorescent photon from the sample triggers the start of the timer, while the following laser pulse stops the timer.

This will be explained in more detail in Subsection 3.2.2 below.

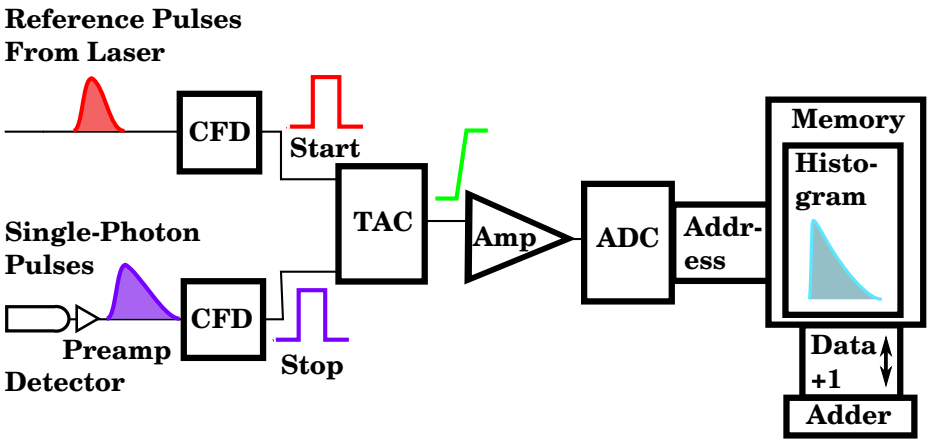

Figure 3.8: A schematic diagram of the components of which a TCSPC system is composed. Adapted from Ref. 16.

3.2.2 Specific tasks of the electronic components

The inputs of the TCSPC system are a reference pulse from a laser and a PL single-photon signal from a detector; see Figure 3.8. For the Ti:Sapphire laser, a fast Silicon-PIN (planar diffused diode) photodiode[5] is used to get an electrical timing reference signal from the optical pulse train[155]. In the photomultiplier tube (PMT), a single incident photon releases an electron from the photocathode which is amplified, by liberating extra electrons through collisions with successive dynodes, and accelerated towards the anode. The gain can reach values of 10^6 to 10^8, the response is very fast (few nanoseconds), but the quantum efficiency is about 0.5

[5] A PIN diode consists of a single crystal having an intrinsic (undoped) region sandwiched between p- and n-type regions, regions with an excess of holes or electrons, respectively. The number of electron-hole pairs produced, when a bias potential is applied across the detector, is dependent on the energy of the incident photons[142].

usually[16, 155]. The output pulse is called the single electron response (SER) which varies in amplitude from pulse to pulse because of the random nature of the signal amplification process in the PMT[16].

A constant fraction discriminator (CFD) triggers on both pulses. To achieve accurate time measurements, accurate triggering, that does not depend on the pulse amplitude, is required[16]. The CFD fulfills this requirement by triggering on the zero cross point of the sum of the input pulse and the delayed/inverted input pulse[155, 16]. Additionally, the CFD rejects input pulses smaller than a threshold value, thus suppressing noise from the environment, from preamplifiers, and small background pulses from the detector[16]. The output pulses of the CFDs are used as start and stop pulses of the time-to-amplitude converter (TAC), as shown in Figure 3.8. This consists of a highly linear ramp generator, usually a capacitor, that is started by one signal and stopped by the other[155, 192]. Hence, the final voltage at the capacitor represents the time between start and stop pulses[16]. The voltage is fed to a biased amplifier (Amp) which selects a smaller time window of the TAC range, and then fed to an analogue to digital converter (ADC)[16]. The ADC resolves the TAC signal into thousands of identical time channels (identical within 1% or better)[16]. Varying time-channel widths result in a systematic variation in the number of photons in the channels which distorts the final result. The ADC converts the amplified TAC signal into the address of the memory corresponding to the time of the photon. By incrementing the data contents of the addressed location the photon distribution builds up[16, 155].

Fast PMTs can manage count rates of up to $\sim 10^7$ counts per second[155, 16]. If the light intensity per signal period is constrained between 0.01–0.1 photons, lasers with repetition rates of 50–100 MHz have count rates near 10^6 photons per second[16]. The way to side-step this overloading problem is by starting the TAC when a photon is detected and stopping it with the next reference pulse from the light source, i.e. reversing the start and stop pulses. Hence, the TAC only has to work at the rate of the photon detection events which is much lower than the rate of the excitation pulses.

3.2.3 Experimental details

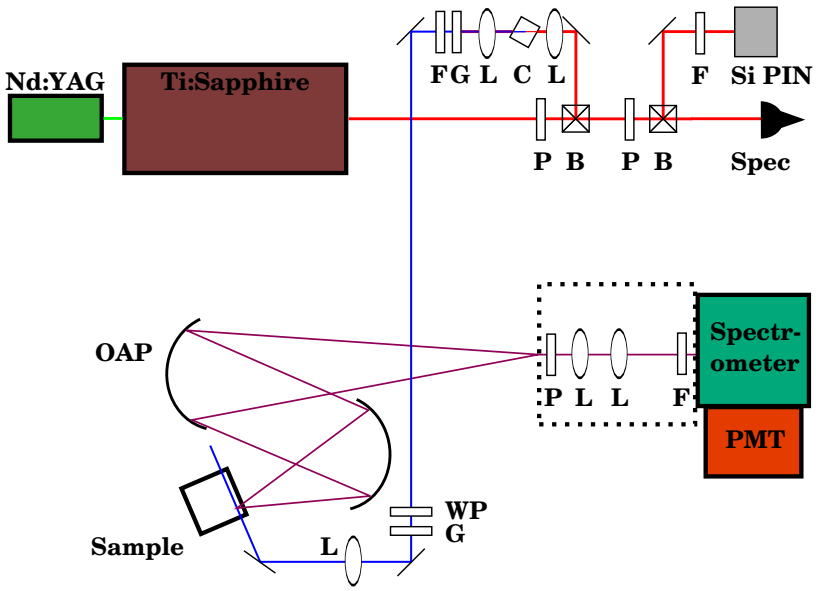

Figure 3.9: Schematic diagram of the laser setup during the time correlated single photon counting experiments.

The experimental setup shown in Figure 3.9 varies from the TIPL setup (Figure 3.4) in two

ways. First, the gate beam is incident on a photodiode which provides the TCSPC Becker & Hickl SPC-130 electronics with a reference pulse train. Secondly, the PL emerging from the OAPs is directed onto a Peltier-cooled photomultiplier tube (PMC-100 from Becker & Hickl). The PMT can detect wavelengths in the range 300-900 nm and has a dark count[6] of 200-500 s^{-1} (counts per second) at 22°C.

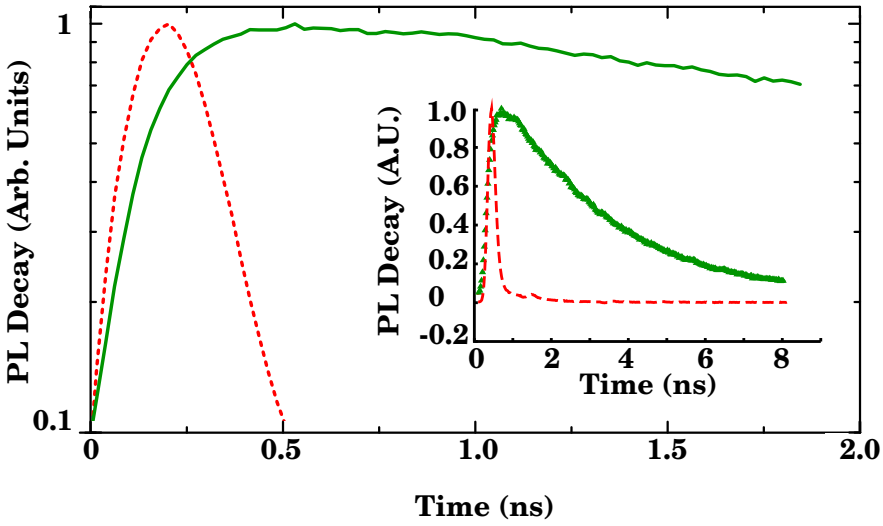

Figure 3.10: Green line: decay of the photoluminescence of a cyanine dye appended to a strand of 40-thymine bases which to each is attached a naphthalene-derivative molecule, at 15°C, measured with the time-correlated single photon counting (TCSPC) technique. Red dashed line: instrument response function (IRF) for the TCSPC system. Inset: long-time decays of the sample and IRF up to 8 ns.

The instrument response function (IRF) of the system would be infinitely narrow if the system was ideal. However, the excitation pulse, the detectors, and the electronics are far from infinitely

[6]Output pulses from PMTs unrelated to light input[155].

sharp and infinitely accurate, respectively[155]. The total IRF is the convolution of all the IRFs from the non-ideal system components[155]. For an analogue signal recording technique, the width of the IRF cannot be narrower than the single electron response (SER), which is 1.5 ns for the PMC-100[16]. However, the time resolution of TCSPC depends on the accuracy at which the time of the individual photons can be determined, i.e. the spread in PMT transit times[192, 16]. The transit time spread (TTS) is determined mainly by the variation in electron transit times of the electrons to the anode in the PMT, and to a lesser extent by the emission at the photocathode, and the timing jitter of the subsequent electronics[16]. Hence, the IRF width is 180 ps (FWHM) for the TCSPC system, which is much shorter than the SER width[16]. The IRF, an example of which is shown in Figure 3.10, is measured by placing a scattering medium in the sample compartment and detecting this scattered light, which simulates a Dirac delta function $\delta(t)$[118], with the TCSPC system[155]. Better resolution can be achieved by using a deconvolution technique to mathematically disentangle the IRF and the true fluorescence lifetime of a sample[147, 118, 13, 192].

3.3 Synthesis of samples

The samples investigated in the following chapters were synthesised by the Functional Organic Materials Group at the Eindhoven University of Technology. A host-guest material was studied in Chapter 4 and Chapter 5. The host, single-stranded DNA (with or without a dye molecule attached at one end), was supplied purified and freeze-dried by *MWG Biotech Ag*[168]. The achiral naphthalene guest derivative, equipped with a diaminopurine hydrogen-bonding unit, was

synthesised via a convergent route involving reactants such as commercial 2,6-diaminopurine and 6-bromo-2-naphthol[95]. The amphiphilic molecules, used in the conjugated nanoparticle study in chapters 6 and 7, were synthesised according to Ref. 1, Ref. 6, and Ref. 105. The procedure used to form nanoparticles from these molecules is described fully in sections 6.2 and 7.2.

Chapter 4

Energy transfer in ssDNA-templated stacks of naphthalene chromophores

4.1 Introduction

DNA-templated chromophore assemblies can overcome some of the difficulties associated with dye-intercalated DNA systems, as mentioned in Chapter 2. This is accomplished through direct hydrogen bonding of diaminopurine-equipped naphthalene derivatives to the bases of single DNA strands. The advantage of this type of system is that the naphthalene chromophores are positioned along the DNA template into well-defined chiral assemblies in solution[95]. By choosing DNA templates with a single Cy3.5 acceptor dye covalently attached to one end, energy transfer from randomly-placed excitations on the DNA-bonded naphthalene assemblies to the assembly end was investigated.

4.2 Samples

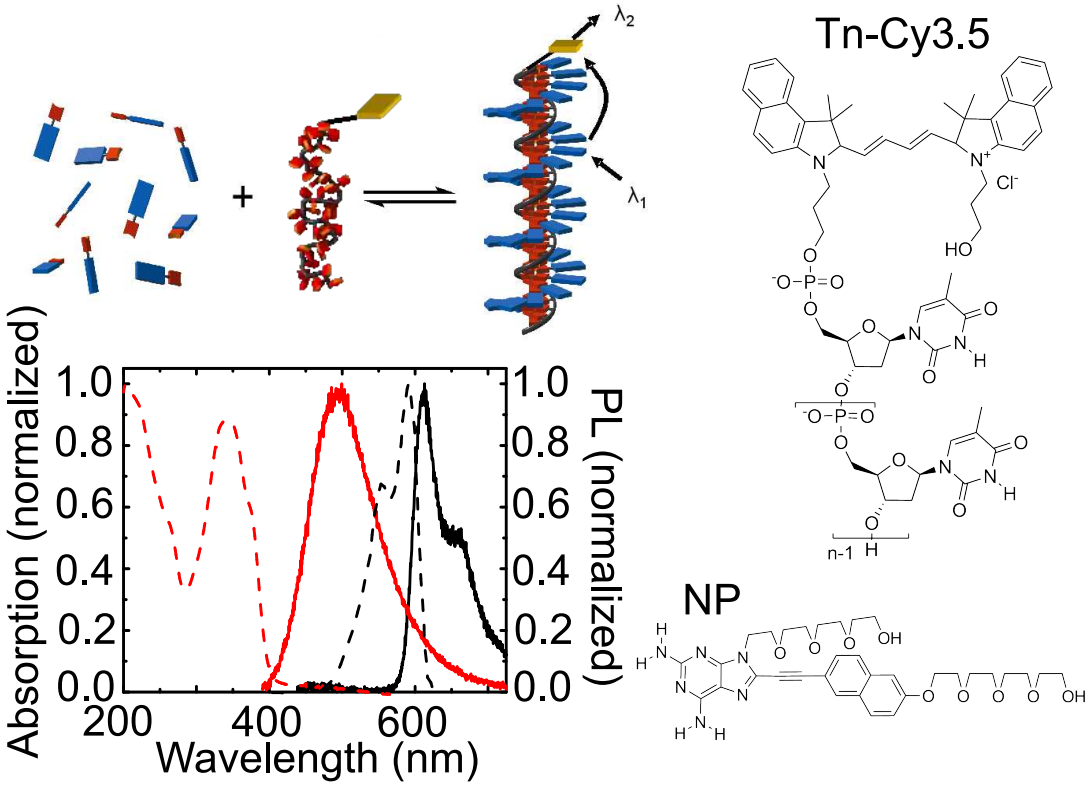

Figure 4.1: Left, Top. Schematic representing the self-assembly of diaminopurine-naphthalene derivatives (NP) along a single-stranded oligothymine template. Samples were prepared in ultrapure water with an NP concentration of 1.6 mM and an oligothymine template concentration that corresponded to a thymine base concentration of 0.4 mM. The final structure obtained has a right-handed helical nature at low ($\leq$20°C) temperatures. Bottom. UV-Vis absorption and photoluminescence spectra for the NP donor (red dashed and solid lines, respectively) and the Cy3.5 acceptor when attached to a 20-base oligothymine (black dashed and solid lines, respectively). Right. Chemical structures of NP and cyanine dye Cy3.5 bonded to the 5' end of the oligothymine.

The system under investigation self-assembles under the auspices of a collective of different chemical bonds, as schematically shown in Figure 4.1. Blue bars represent the non-chiral diaminopurine naphthalene derivative (NP) chromophores, whose synthesis has been detailed in Ref. 95. The black strand represents the single-stranded (ss) DNA template, denoted by Tn, which consists of n thymine bases. Paramount in driving the template-NP binding is the triple hydrogen bonding of NP, via its diaminopurine end, to the pyrimidine unit of each thymine basis. The hydrogen bonding groups of these molecules are indicated by red bars in Figure 4.1. The synthetic design criteria and characterisation for this and for a similar supramolecular system have been described in detail in Refs. 95, 168, and Refs. 92, 94, respectively. A complex range of intermolecular interactions influence the assembly process, which can be affected by even small changes in the molecular structure of the individual components[94]. Ethylene oxide side groups were selected for NP to facilitate solubility in water, while termination of the molecule with a hydroxy group was chosen to inhibit both NP aggregation and also further aggregation of the whole DNA hybrid complex[97, 92, 94]. In addition, the NP donor was designed expressly to incorporate a diaminopurine hydrogen bonding unit, because the diaminopurine's large π-conjugation area strengthens the donor-donor interactions — in turn, promoting stabilisation of the assembly, especially for long template lengths[95].

Previous characterisation of these assembled systems has revealed that the hydrogen bonding of NP to the template is weaker than bonds between complementary bases in double-stranded (ds) DNA, and highly specific[95]: NPs did not bind to strands of adenine or cytosine bases, and dsDNA was formed in preference to retention of the NP-oligothymine aggregates when

a strand of complementary adenine bases was added to solutions containing the templated assembly[95, 97]. Together, molecular modelling and morphological studies show that the stacking geometry and resulting chiral order strongly depend on the nature of the chromophore. For naphthalene-based systems, the relatively weak interactions between such molecules yield assembled supramolecules resembling the dsDNA B-helix structure[198]. A simple one-dimensional Ising model has been used to demonstrate that the interplay between the energies involved in donor-oligothymine (guest-host) and donor-donor (guest-guest) binding has a strong influence on the formation of the aggregates[94]. Spectroscopic evidence for the formation of templated assemblies has also been presented: upon mixing the donor with the template, the absorption band was found to be blue-shifted and mitigated in intensity while the circular dichroism[1] spectrum exhibited a positive Cotton-effect in the naphthalene absorption region[95]. These results are indicative of the formation of chiral aggregates[203], with the oligothymine template inducing a right-handed helical structure as NP binds to it. The length and thickness of 20-base templated assemblies, containing diaminotriazine hydrogen bonding naphthalenes, have been determined to be approximately 7 nm and 3.5 – 4 nm, respectively, based on a combination of cyro-transmission electron microscopy (cryoTEM), angle-dependent dynamic light scattering (DLS), atomic force microscopy (AFM), and molecular dynamical modelling[94, 198].

[1] Spectroscopic method measuring the difference in absorbance of left- and right- handed circularly polarised light by a material, as a function of wavelength. Chiral molecules and biomolecules with secondary structures show circular dichroism in their absorption bands[142].

To permit investigations of energy transfer in the DNA templated assemblies, an acceptor Cy3.5 cyanine dye (yellow bar in Figure 4.1) was covalently bonded to the phosphate group at the 5' end of the ssDNA. Cyanine dyes are characterised by two heterocyclic components connected by a polymethine bridge. They benefit from large extinction coefficients; moderate fluorescence quantum yields; and widespread applicability as photosensitisers, stains, and fluorescent probes[69]. The absorption and photoluminescence spectra shown in Figure 4.1 contain a cyanine dye absorption peak at 589 nm and an emission peak at 612 nm. For NP, absorption is found to peak at 344 nm and emission broadly around 480 nm. The spectral overlap between the NP donor chromophore emission and the Cy3.5 acceptor absorption should thus permit efficient energy transfer from the former to the latter chromophore.

In order to assess the dependence of energy transfer on the assembly length, samples containing oligothymines with different numbers of bases n were used, with n being either 10, 20, 30, 40, or 60. To allow accurate relative measurement a complex (NP-Tn-Cy3.5), an acceptor (Tn-Cy3.5), and a donor (NP-Tn) sample for each oligothymine length were prepared. Here, the acceptor sample comprised a Cy3.5 acceptor dye covalently bonded to the 5' end of the n-base oligothymine; the donor sample an n-base oligothymine template decorated with NP donors; and the complex sample a Cy3.5 dye bonded to the donor-decorated n-base oligothymine template. Samples were prepared in ultrapure water with an NP concentration of 1.6 mM and an oligothymine template concentration that corresponded to a thymine base concentration of 0.4 mM. Therefore, each base site was available to an average of four NPs in order to promote filling of the template binding sites at low temperatures[95]. In the absence of the template,

NP is dissolved molecularly at this solution concentration, i.e. aggregation effects should not be expected[95].

4.3 Experimental details

Time-integrated measurements using the experimental setup shown in Figure 3.4 and time-resolved measurements using the TCSPC technique, see Chapter 3, were performed on the DNA-hybrid samples. During the measurements, the sample solutions were held in micro-cuvettes (internal dimensions of 1 mm $\times$1 mm $\times$40 mm) mounted on a temperature-controlled stage that allowed adustments between 15°C and 90°C with an accuracy of 1°C. The samples were excited at 375 nm with an excitation power of 30 μW using the frequency-doubled pulsed output from the Ti:Sapphire *Tsunami* laser described in Chapter 3. The excitation wavelength was chosen to excite predominantly the NPs. The excitation power and collection time (25 s per TCSPC scan) was set so that sample degradation was reduced to an acceptable minimum. This was helped further by moving the sample stage vertically so that fresh solution was excited for each measurement. In addition, the low excitation powers and high pulse repetition rate meant that measurements were taken in a linear regime, with significantly fewer than one excitation per assembly at any given time. Heating the samples was a fully reversible process[94], as confirmed by the recovery of TIPL peak heights upon heating, cooling, and re-testing each sample. When not in use for short durations, the samples were stored in a darkened environment in air at room temperature, and returned to a freezer at other times.

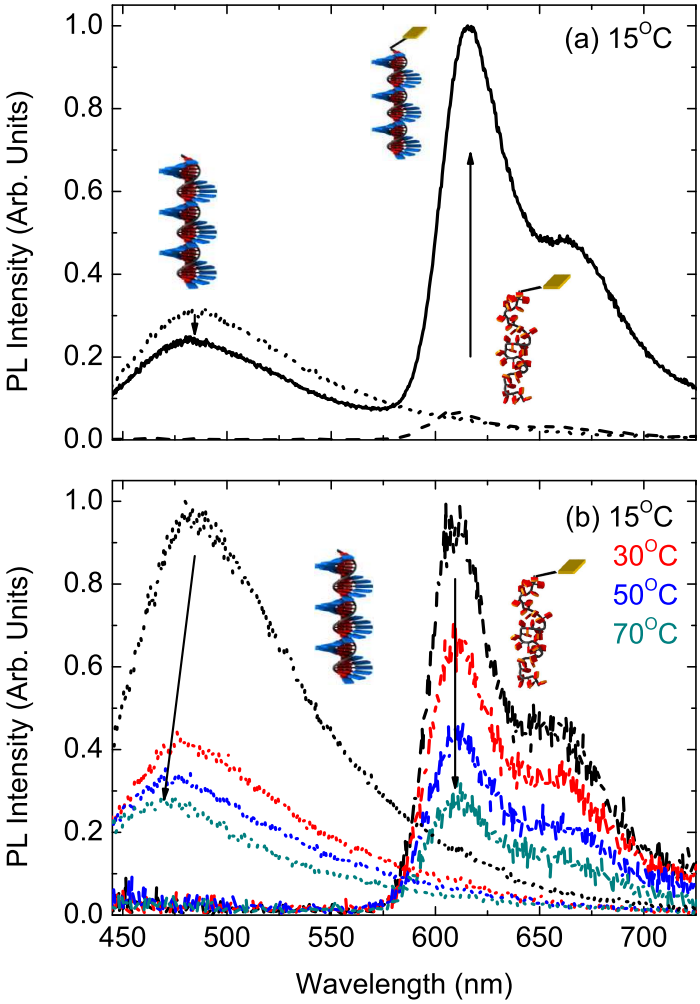

Figure 4.2: (a) Time-integrated photoluminescence of the "complex" (NP-T*40*-Cy3.5; solid line), the "acceptor" (T*40*-Cy3.5; dashed line), and the "donor" (NP-T*40*; dotted line) at 15°C. (b) Time-integrated photoluminescence of the 40-base "donor" (dotted lines) and 40-base "acceptor" (dashed lines) for different temperatures.

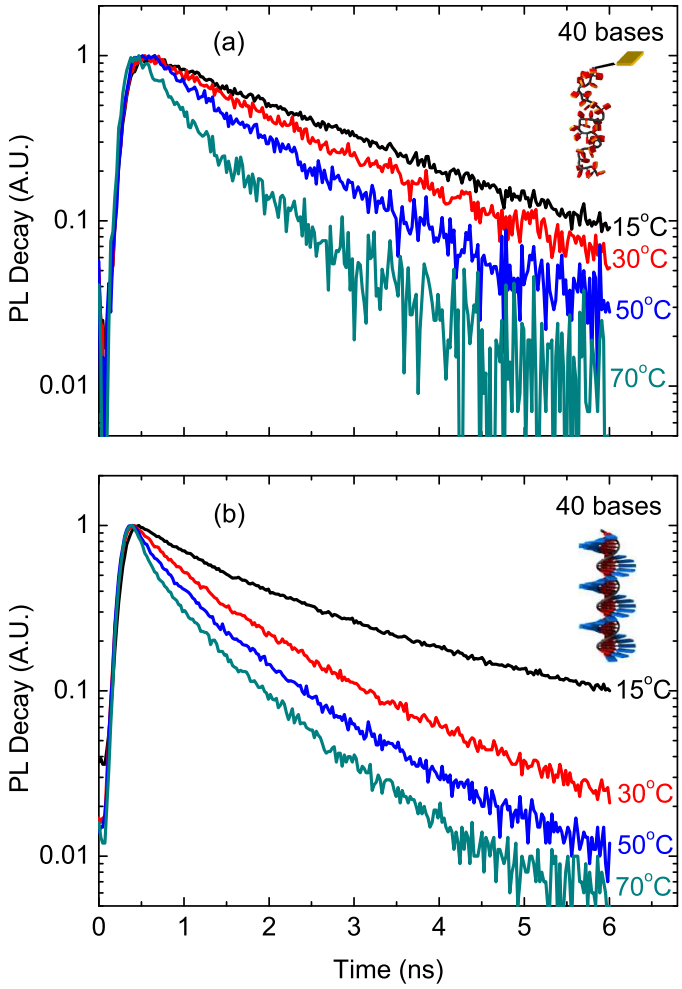

Figure 4.3: (a) Time-resolved photoluminescence of Cy3.5 attached to a 40-base oligothymine (the "acceptor") for different temperatures, detected at the peak (620 nm) of the emission spectrum. (b) PL decay of a 40-base oligothymine-NP assembly lacking the Cy3.5 dye (the "donor") for different temperatures, detected near the peak (507 nm) of the emission spectrum.

4.4 Results and discussion

4.4.1 TIPL

Initial measurements of TIPL spectra for donor, acceptor and complex samples were performed and relative donor peak quenching and acceptor peak enhancing for the complexes at low temperatures was observed; see Figure 4.2(a). This is in qualitative agreement with energy transfer between Cy3.5 and NP when integrated in the complex. As mentioned in Section 4.3, all TIPL peak heights recovered fully when cycling the samples thermally between 15°C and 70°C, thus confirming that supramolecular assembly is a reversible process for this system. A slight red shift with decreasing temperature was identified for the donor peak in Figure 4.2(b), in accordance with aggregation[111] of the NPs, induced by the oligothymine template at low temperatures. In addition, the figure showes that both the donor and acceptor peak intensities decrease with increasing temperature, which complicates a quantitative assessment of energy transfer based on such data alone. The subsequent analysis is based, accordingly, on measurements of the time-resolved emission recorded for the donor, acceptor and complex samples.

4.4.2 Donor and acceptor decay dynamics

For an accurate assessment of energy transfer in the DNA-templated complexes, the PL decay dynamics of the donor and the acceptor in the absence of the other species was measured and analysed. To investigate the effect of temperature on the lifetimes of the donor (NP-Tn) and acceptor (Tn-Cy3.5) samples, TCSPC measurements were performed for n=40 for a range of

different temperatures.

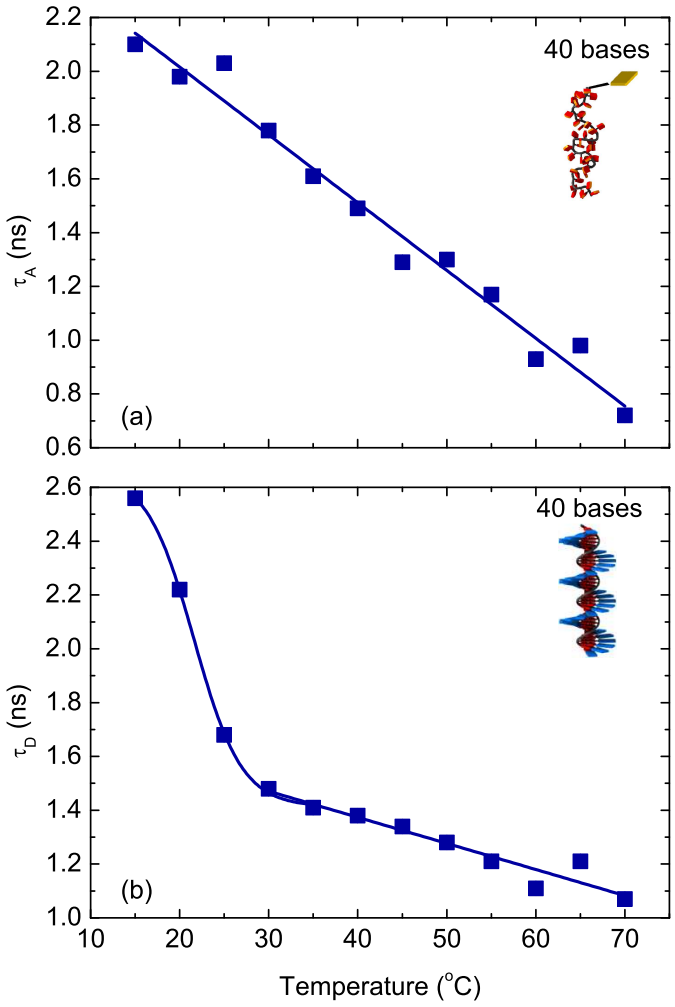

Figure 4.4: PL decay lifetimes for (a) the acceptor (T*40*-Cy3.5) and (b) the donor (NP-T*40*) as a function of temperature, extracted from the PL decay curves shown in Figure 4.3 by fitting a mono-exponential function to the data within the range 0.4 ns (TCSPC peak) to 6 ns (T*40*-Cy3.5) or 1.5 to 5 ns (NP-T*40*). Solid lines are guides to the eye.

Figure 4.3 shows the normalised PL decays of (a) the acceptor sample, detected at 620 nm, and (b) the donor sample, detected at 507 nm. While the acceptor PL decay is mono-exponential, the donor PL is slightly non-exponential concomitant with the presence of both aggregated NP on the template and excess molecularly-dissolved NP. Both species show faster PL decay with increasing temperature. To quantify the changes in lifetimes, these data were fitted with single exponentials and the resulting lifetimes displayed in Figure 4.4 as a function of temperature for both the acceptor (τ_A) and the donor (τ_D).

Figure 4.4(a) indicates that the lifetime of Cy3.5 bound to the DNA template decreases almost linearly from its value of 2.1 ns at 15°C to 0.7 ns at 70°C, suggesting increasingly efficient non-radiative excitation pathways at higher temperatures. It is not thermodynamically favourable for the dye to be quenched via photoinduced electron transfer by the thymine bases of the template[71, 172], as shown in a study of the relative excited-state reduction potential of a Cy3 dye and oxidation potentials of various nucleobases[202]. Collisions with solvent molecules and intramolecular vibrations may make a contribution to such effects. However, the observed trend is most likely caused by changes in photoisomerisation which has been shown to provide an efficient nonradiative-deactivation pathway for cyanine dyes, especially those with short polymethine chains[172]. In this process, the polymethine linkers adopt an all-*trans* configuration in solution until, upon absorption of light, the dyes isomerise from the first excited singlet state to a ground state photoisomer which adopts a mono *cis* conformation[172]. The isomerisation occurs via a partially twisted intermediate excited state. The *cis* photoisomer undergoes a thermal back isomerisation to yield the ground state *trans* isomer[135]. Attaching a cyanine dye to

a bulky substituent, such as a long oligothymine molecule, increases the activation energy of isomerisation, thus increasing the lifetime of the dye[172].

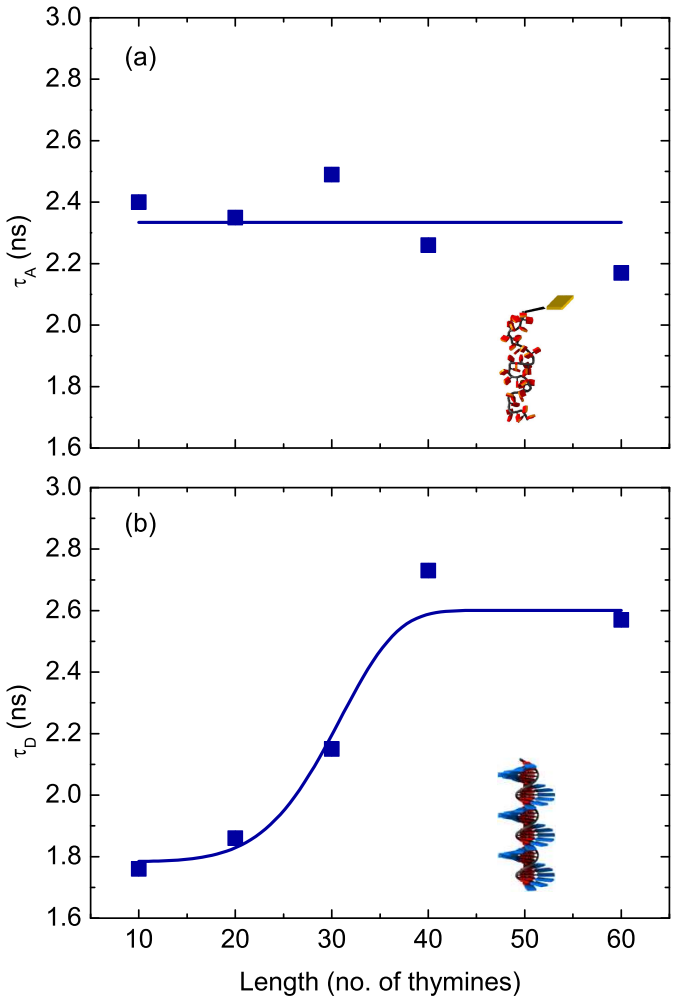

Figure 4.5: (a) Acceptor (T*n*-Cy3.5) and (b) donor (NP-T*n*) lifetimes for different oligothymine lengths *n*, extracted through mono-exponential fitting to the PL decays measured at 15°C at the emission peak wavelengths. Solid lines are guides to the eye.

Comparable effects have been previously witnessed for the similar dye Cy3, which in solution has a lifetime of $\sim$0.2 ns that increases to $\sim$2 ns when Cy3 is attached to ssDNA[85, 172]. Isomerisation is an activated process that depends strongly on the temperature of the medium such that a decrease in lifetime with temperature, as shown in Figure 4.4(a), is to be expected.

Figure 4.4(b) implies the temperature-dependence of the NP donor lifetime τ_D, which exhibits a sharp decrease between 15°C and 30°C superimposed on a more subtle linear decrease towards higher temperature. The lifetime of aggregated NP is longer than that for unbound NP, therefore the initial sharp decrease of τ_D indicates the detachment of NP from the oligothymine once the complex dissolves around the transition temperature. These trends in donor lifetimes are matched by those found in circular dichroism (CD) measurements (*vide infra*): as the temperature is raised above $\sim$25-30°C the CD signal disappears in accordance with the dissolution of helical aggregates of NP, as previously observed in similar complexes[94]. The small, linear decrease of donor lifetime with temperature is likely to be again caused by an increasingly efficient non-radiative pathway, possibly involving the solvent and relaxation of vibrational states.

The dependence of the acceptor and donor lifetimes (at 15°C) on oligothymine-template length was determined using the same procedure as described above. The results are displayed in Figure 4.5, which indicates that the acceptor has a length-independent lifetime with an average of 2.33 ns. This is in excellent agreement with the value of 2.31 ns reported for a Cy3.5 dye attached to ssDNA consisting of approximately 30 bases[101]. It has been reported also that the lifetimes of acceptor molecules attached to dsDNA hairpin structures are constant as

the base pair domain length varies[128]. The donor lifetime, on the other hand, increases from $\sim$1.8 ns for short (n=10) oligothymines to $\sim$2.6 ns for long ($n\geq$40) oligothymines. As already mentioned, the donor lifetime depends on the degree of templated assembly of NP and, hence, the ordering and distribution of the NPs on the template. On short templates, similar naphthalene derivatives have been shown to be arranged in a disordered assembly with varying distances between conjugated units along the template[198]. CD spectra corroborate this theory as smaller templates exhibit low peak intensities (*vide infra*) showing that the donors barely bind to the 10-base oligothymine thus decreasing the donor PL lifetime. The cooperative nature of the assembly means that a minimum template size is clearly needed to stabilise the hybrid complex[95]. There is theoretical evidence that, at low temperatures, short templates in solution are either filled with similar naphthalene derivatives or empty. Mixed forms are not favoured because of a lack of combinatorial entropy as fewer mutually distinguishable distributions of bound guest molecules are possible[94]. In contrast, temperature-dependent UV absorption experiments for similar DNA-templated complexes show that stronger guest-guest interactions exist for longer templates, which increases the stability of the stack and the ordering of the donors along the template[94]. It is important to note that the diaminopurine-naphthalene derivative donors used in this study have a stronger guest-guest, and weaker host-guest, interaction energy than the similar diaminotriazine-naphthalene derivatives mentioned above[95]. Hence, it can be assumed that the donor arrangement on short templates is disordered and that donors may have only limited binding to short templates.

4.4.3 Energy transfer dynamics in donor-acceptor complexes

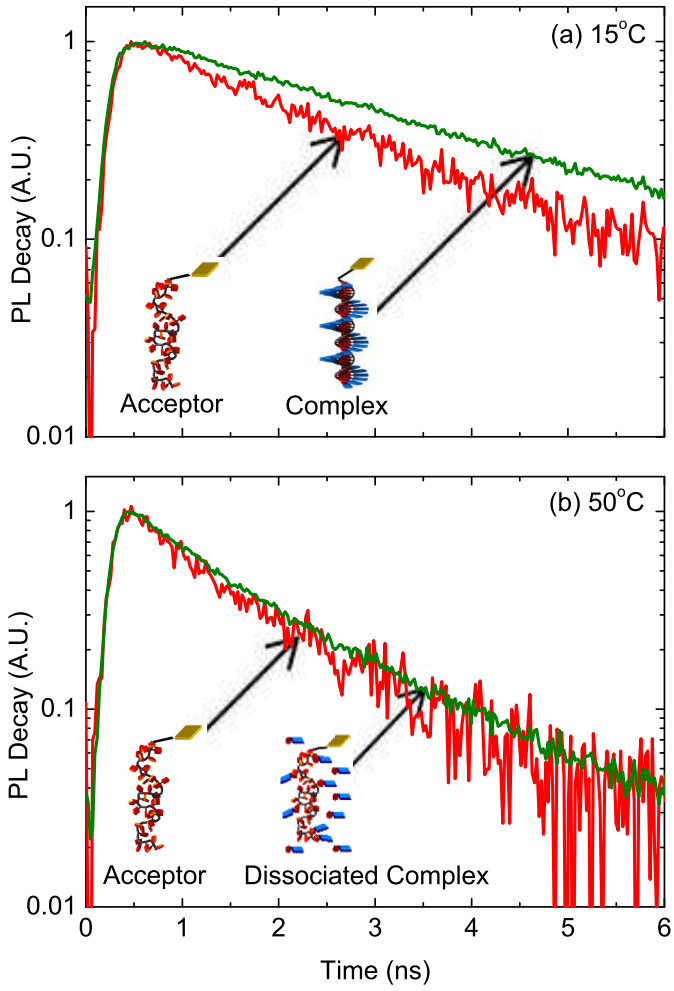

Figure 4.6: Photoluminescence decay of the acceptor (T*60*-Cy3.5) and the complex (NP-T*60*-Cy3.5) sample, measured at 620 nm for (a) low (15°C) and (b) high (50°C) temperature. At 50°C, the complex has dissociated with the donors molecularly dissolved in solution.

In order to assess the rate at which energy transfer occurred between naphthalene and Cy3.5 chromophores, measurements of (A) the Cy3.5 PL decay on the template with and without NP attached (i.e. for acceptor *vs.* complex samples), and (B) the NP luminescence decay on the template with and without Cy3.5 attached (i.e. for donor *vs.* complex samples) for all template lengths were performed. Figure 4.6 shows an example of such data for the 60-base oligothymine for Case A at two different temperatures, 15°C and 50°C, at which the complexes are respectively either assembled or fully molecularly dissolved. At low temperature, the Cy3.5 luminescence is longer lived when NP is present, suggesting energy transfer from NP to Cy3.5 occurs. However, this discrepancy is not fully removed when the complexes are dissociated at 50°C. It is unlikely that significant energy transfer occurs from dissociated NP to the Cy3.5 dyes at the low solution concentrations employed. Instead, the higher viscosity of the complex solution caused by the presence of NP may induce interactions that affect the photoisomerisation of the dye[127], and hence modify the Cy3.5 lifetime.

Figure 4.7 shows the peak-normalised PL decay for NP donors in the presence of the 60-base oligothymine template with and without the covalently-bonded acceptor dye (Case B) at 15°C and 50°C. These data demonstrate that the lifetime of the donors is shorter in the presence rather than in the absence of Cy3.5 acceptors. This difference disappears when the solution temperature is raised beyond the point at which the complexes dissociate. Both the lengthening of the acceptor lifetime in the presence of donors, and the shortening of the donor lifetime in the presence of acceptors over the same timescale, provide strong evidence for the occurrence of energy transfer between the donor and the acceptor when complexes form at low temperatures.

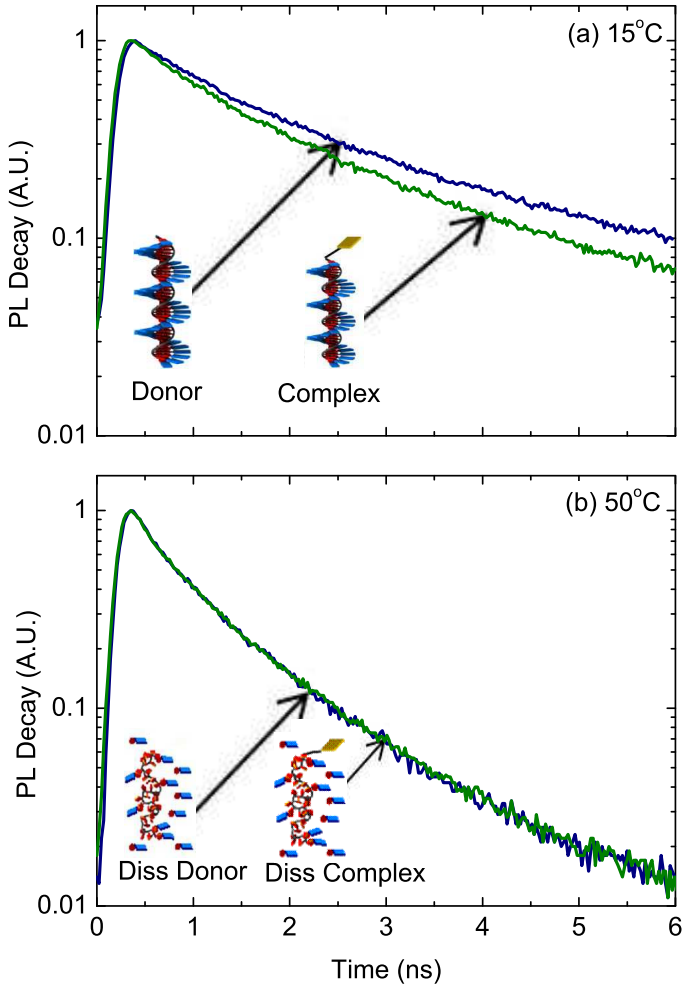

Figure 4.7: Photoluminescence decay of the donor (NP-T*60*) and the complex (NP-T*60*-Cy3.5) sample, measured at 507 nm for (a) low (15°C) and (b) high (50°C) temperature. At high temperatures, the donor and complex samples have dissociated (named diss donor and diss complex, respectively); see the text for details.

In order to obtain more quantitative information on the transfer rates involved, the changes in NP luminescence in the presence and absence of Cy3.5 (Case B) were analysed to avoid complications caused by direct acceptor excitation and solution viscosity changes affecting the acceptor lifetime, as mentioned above.

4.4.4 Removal of excess donor background

The additional decay path induced by the Förster radiative energy transfer mechanism for donor excitons must be considered when describing the de-excitation of the donor through all mechanisms[76, 134, 137]. In the absence of acceptors, the time-dependent PL decay of the donor bound to the template is

$$I_D(t) = \hat{I}_D \ \exp\left(\frac{-t}{\tau_D(t)}\right), \tag{4.1}$$

where $\hat{I}_D$ is the intensity at time $t = 0$, and τ_D the donor ensemble lifetime, which may be time dependent. In the presence of acceptors, the time-dependent PL decay of the donor is given by

$$I_C(t) = \hat{I}_C \exp\left[-t\left(\left(\frac{1}{\tau_D(t)}\right) + k_{ET}(t)\right)\right], \tag{4.2}$$

where $\hat{I}_C$ is the complexes' PL intensity at $t = 0$ and $k_{ET}(t)$ is the energy transfer rate to the acceptors. However, as mentioned in sections 4.2, 4.4.2, and 4.4.3, an excess of three donors per DNA binding site was added in order to ensure that the sites are more likely to be filled effectively[95]. In order to obtain I_D and I_C from the measured data, the PL background arising from the presence of the unbound donors was removed carefully, which was facilitated by taking into account that at temperatures over 50°C all NP molecules are not hydrogen-bonded to the

template.

At low temperatures T (e.g. 15°C), the PL decay from the donor can thus be described by

$$I_D^{15°C} = \hat{I}_D \left[\eta_{bound} N_{bound}^{15°C} \exp\left(-\frac{t}{\tau_{D,bound}} \right) + \eta_{free} N_{free}^{15°C} \exp\left(-\frac{t}{\tau_{D,free}} \right) \right]. \tag{4.3}$$

Here $\tau_{D,bound}$ and $\tau_{D,free}$ are the lifetimes of excitations on NP bound to the template, and those on excess, unbound NP, respectively, $N_{bound}^{15°C}$ and $N_{free}^{15°C}$ are the numbers of free and bound NP donors excited in the imaged volume of solution (at 15°C), and η_{bound} and η_{free} the quantum efficiencies of emission of the free and bound NP, respectively. At elevated temperatures (e.g. 50°C), all NP are detached from the templates, and the donor PL decay is given by

$$I_D^{50°C} = \hat{I}_D \eta_{free} N_{free}^{50°C} \exp\left(-\frac{t}{\tau_{D,free}} \right). \tag{4.4}$$

It is assumed implicitly that $\eta_{free}^{15°C} \equiv \eta_{free}^{50°C}$ because the largest intensity changes in donor PL (Figure 4.2(b)) and the largest donor lifetime changes (Figure 4.4(b)) occur over the temperature range of NP detachment from the template. The underlying changes to the quantum efficiencies of emission of the free NP as the temperature increases are negligibly small in comparison. As mentioned above, energy transfer at a rate $k_{ET}(t)$ has to be considered as an additional de-excitation pathway for NP in the complex, and the PL decay at low temperatures can be described by

$$I_C^{15°C} = \hat{I}_C \left[\eta_{bound} N_{bound}^{15°C} \exp\left(-\frac{t}{\tau_{D,bound}} - k_{ET} t \right) + \eta_{free} N_{free}^{15°C} \exp\left(-\frac{t}{\tau_{D,free}} \right) \right], \tag{4.5}$$

At high temperatures, again all NP are detached from the template which leads to the suppres-

sion of energy transfer and all luminescence originates from unbound NP, i.e.

$$I_C^{50^\circ C} = \hat{I}_C \, \eta_{free} \, N_{free}^{50^\circ C} \exp\left(-\frac{t}{\tau_{D,free}}\right). \tag{4.6}$$

Using equations 4.3 to 4.6, the energy transfer dynamics I_{ET} can now be extracted by calculating first the PL decay components associated only with NP *bound to the templates*, as

$$X \equiv I_D^{15^\circ C} - \frac{N_{free}^{15^\circ C}}{N_{free}^{50^\circ C}} I_D^{50^\circ C} = \hat{I}_D \, \eta_{bound} \, N_{bound}^{15^\circ C} \exp\left(-\frac{t}{\tau_{D,bound}}\right) \tag{4.7}$$

and

$$Y \equiv I_C^{15^\circ C} - \frac{N_{free}^{15^\circ C}}{N_{free}^{50^\circ C}} I_C^{50^\circ C} = \hat{I}_C \, \eta_{bound} \, N_{bound}^{15^\circ C} \exp\left(-\frac{t}{\tau_{D,bound}} - k_{ET}\, t\right). \tag{4.8}$$

From Eqns. 4.7 and 4.8 the energy transfer dynamics, where the *only* cause for donor de-excitation is energy transfer to acceptors[76], can then be determined through

$$I_{ET} = \frac{Y}{X} = \hat{I}_{ET} \, e^{(-k_{ET}\, t)}, \tag{4.9}$$

provided that the fraction $f = \frac{N_{free}^{15^\circ C}}{N_{free}^{50^\circ C}}$ is known. In general f can be directly calculated from the absorption coefficients $\alpha_{15^\circ C}$ and $\alpha_{50^\circ C}$ of the cold and hot solutions. However, for the experiments presented here, the absorption coefficients were small compared to the length of the imaged volume and the two absorption coefficients were very similar at the excitation wavelength used. For these cases, f is simply given by the concentration ratio

$$f = \frac{c_{free}}{c_{free} + c_{bound}} \tag{4.10}$$

i.e. it is the fraction f=0.75 of NP molecules that are free (unbound) even at low (15°C) temperature as a result of the addition of excess NP.

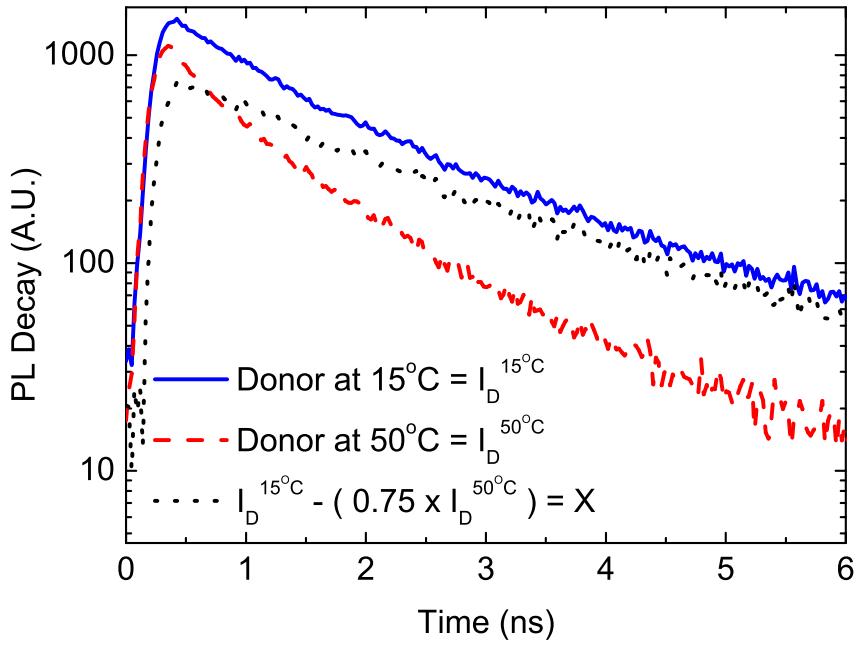

Figure 4.8: Photoluminescence (PL) decays illustrating the procedure involved in removing the excess NP contribution from the assembled NP photoluminescence decay contribution. $I_D^{15^\circ C}$ is the PL decay of a *n*-base oligothymine-NP assembly at a low temperature (15°C, for example), where *n* is the number of thymines. $I_D^{50^\circ C}$ is the PL decay of a *n*-base oligothymine-NP assembly at a high enough temperature at which all NP are assumed not to be bonded to the oligothymine. X is the NP-excess corrected decay solely from excitations on NP hydrogen-bonded to the template.

It is assumed that at temperatures of 50°C and over, all NP molecules present in the samples are not hydrogen-bonded to the template. TCSPC delay traces confirmed this assumption: the non-normalised intensities of the donor samples for arbitrary oligothymine length (at a detection wavelength of 507 nm) converged to a baseline PL decay that did not change significantly

between 50°C and 70°C. Another indication that the assemblies have fragmented at 50°C is the flattening of the temperature-dependence of τ_D values at this temperature; see Figure 4.4(b). For a given low temperature T (e.g. for 15°C as described above), the transfer dynamics were thus calculated using equations 4.3 to 4.9 with 50°C as the high-temperature reference point for which all NP are assumed to be free. Figure 4.8 illustrates the results of such calculations for T=15°C.

4.4.5 Experimental rates of energy transfer

Figure 4.9 shows the extracted energy transfer dynamics I_{ET} for complexes formed at 15°C for a number of different template lengths. The transfer dynamics accelerate from complexes with template length of n=10 base pairs towards those with n=30 bases, for which they are fastest, and then reduce again towards complexes with n=60 bases. In addition, the shape of the curves can be described in all cases by a stretched exponential, i.e.

$$I_{ET}(t) = \hat{I}_{ET} \exp\left[-\left(\frac{t}{\tau_0}\right)^d\right] \tag{4.11}$$

Comparison with Eqn. 4.9 yields an energy transfer rate $k_{ET} = t^{d-1}\tau_0^{-d}$ where τ_0 and d are time constants affecting the time-dependent rate of energy transfer k_{ET}. Such time-dependent energy transfer rates are very commonly observed for complex systems[24, 76, 153] and may arise from a multitude of causes, such as exciton diffusion or inhomogeneous chromophore arrangement in the system. When acceptors are randomly distributed throughout an arrangement of donors, the energy transfer dynamics have been shown to adopt the stretched-exponential behaviour[153] described by Eqn. 4.11 because of the range of donor-acceptor distances present.

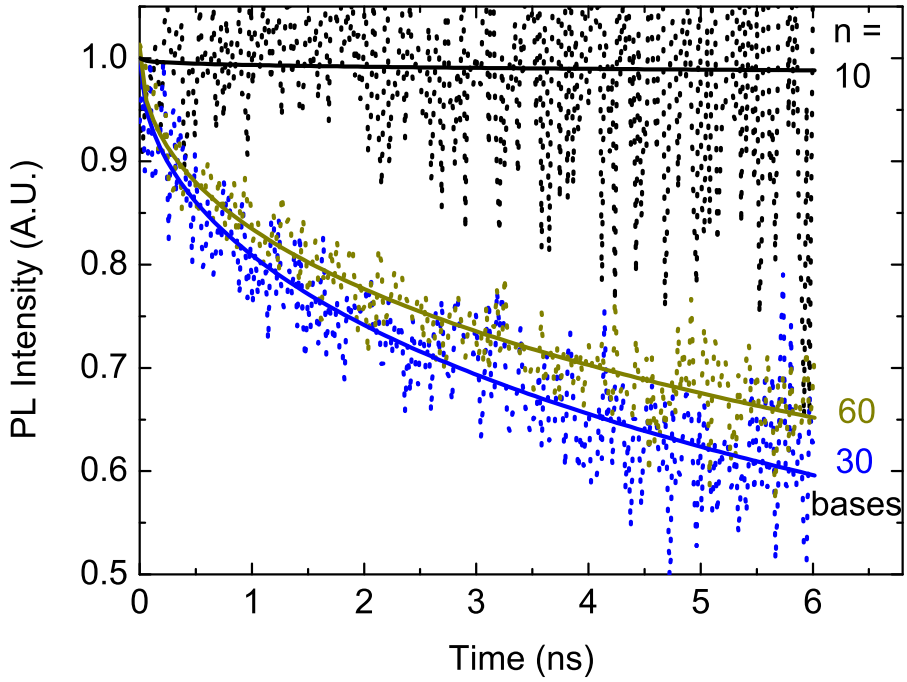

Figure 4.9: Energy transfer dynamics reflecting the NP emission decay arising solely from energy transfer to Cy3.5. The curves are derived from the donor PL transient, of which some are shown in Figure 4.7, by removing the contribution arising from excess unattached NP and from intrinsic donor excitation decay, as described in the text. Solid lines are fits to the data using the stretched-exponential function given by Equation 4.11.

In this case, the exponent d directly relates to the dimensionality Δ of the system[15, 29], with $\Delta = 6d$. For such systems, decreasing dimensionality for fixed acceptor concentrations leads to an increasing emphasis of fast initial PL decay as well as very slow PL decay components, a behaviour attributed to the increasing dominance of nearest-neighbours in the trapping of excitation energy[24, 137]. Equation 4.11 was fitted to the energy transfer curves as in Figure

4.9, and it is found that for all temperatures and template lengths for which stable assemblies form, $d = 0.6 \pm 0.1$. This value suggests a "dimensionality" of $\Delta = 3.6 \pm 0.6$. However, for the DNA-templated system under investigation here, the constant d cannot be directly linked with system dimensionality, as the acceptor chromophores are not randomly distributed but attached solely to the end of a strand of donors. As detailed in Chapter 5, a model was developed that incorporates a realistic structure of the complexes.

The value of energy transfer rate constant τ_0^{-1} was also extracted for the value of $d = 0.6$, and is displayed in Figure 4.10 (blue squares) as a function of DNA-template length. τ_0^{-1} is found to be strongly template-dependent: it is initially low for short oligothymines and rises with an increase in the length of the oligothymine template, then peaks for the 30-thymine strand with $\tau_0^{-1} \sim 0.05\,\mathrm{ns}^{-1}$, and subsequently decays towards longer ($\geq$60) template lengths. This complex behaviour arises from the contributions of two counteracting effects. For short templates, incomplete attachment of NP to the template suppresses the energy transfer[95], while for long templates, an increase in donor-acceptor distances also leads to a reduction. Therefore, an overall maximum in transfer efficiency can be expected for a particular template length. Figure 4.10 (green circles) shows the CD amplitude measured for complex samples of different lengths (NP-Tn-Cy3.5), at 15°C and a detection wavelength of 358 nm, near the peak of the donor absorption. A sharp onset in the CD amplitude arising from the Cotton effect can be clearly seen between $n \sim$20-30 matching the similar rise in energy transfer rate constant over that range.

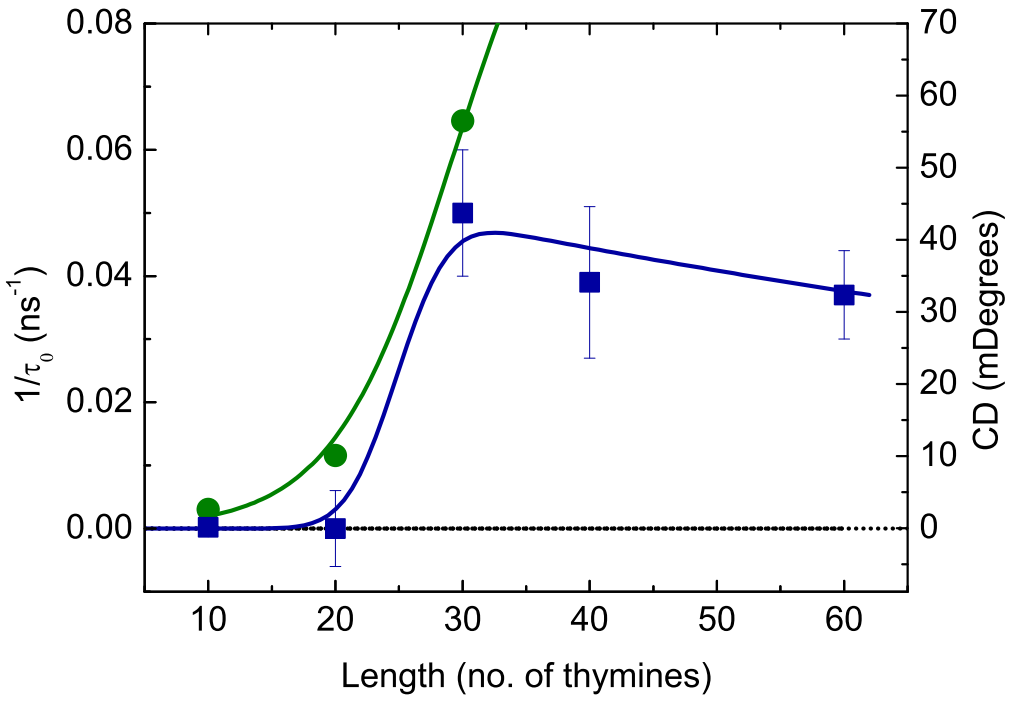

Figure 4.10: Blue filled squares: energy transfer rate constant τ_0^{-1} extracted from stretched-exponential fits to the energy transfer dynamics shown in Figure 4.9, plotted as a function of the number n of oligothymine bases forming the template. Green filled circles: circular dichroism signal at 358 nm as a function of oligothymine length n at 15°C. The solid lines are guides to the eye.

In addition, the influence of solution temperature on the energy transfer was investigated by extracting the transfer dynamics, correcting as described in Section 4.4.4 for excess donor and intrinsic donor PL, for the 40-base oligothymine sample. The resulting decay curves were again fitted with Eqn. 4.11 for $d = 0.6$, and the resulting τ_0^{-1} values displayed in Figure 4.11 as a function of temperature. The energy transfer rate parameter shows a strong correlation with the CD amplitude measured for the same complexes. As the system becomes more dis-

ordered at high temperatures and finally dissociates, the transfer rate constant τ_0^{-1} tends to zero.

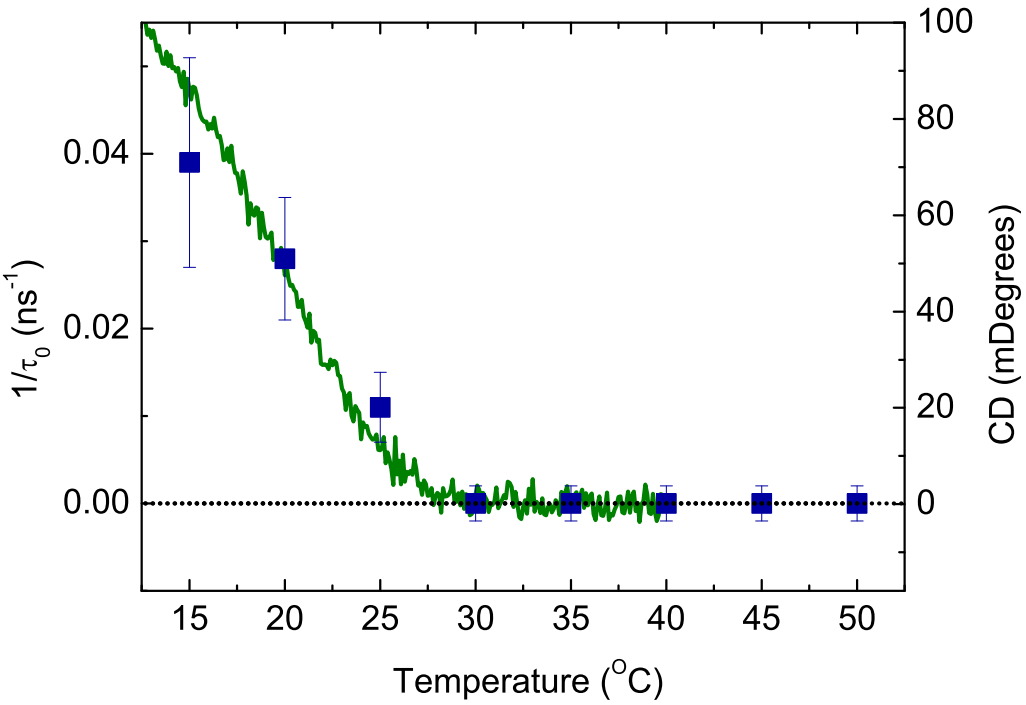

Figure 4.11: Solid squares: experimentally determined energy transfer rate constant (τ_0^{-1}) extracted from fits of a stretched exponential (Equation 4.11) to the energy transfer dynamics for a 40-base oligothymine (see Figure 4.9), as a function of temperature. The green solid line is the circular dichroism signal measured at 354 nm as a function of temperature.

4.5 Conclusion

The energy transfer has been investigated in a system comprising naphthalene donor chromophores attached via hydrogen bonding to a DNA template decorated with a Cy3.5 acceptor

molecule at one end. The efficiency of energy transfer from donor to acceptor depends intricately on temperature and template length, both of which have a strong influence on the extent to which the template is populated with an ordered donor assembly. Circular dichroism and donor lifetime data show that the assemblies dissociate over a fairly narrow ($\pm 5^{\circ}$C) temperature range centred around 25°C. Energy transfer rates decline to zero over the same range, as the temperature is raised, indicating that ordered assembly is a prerequisite for energy transfer. In addition, the energy transfer efficiency is found to exhibit a complex dependence on template length, with transfer rates increasing initially with template length towards an optimum for n=30, and then declining again towards n=60. In Chapter 5, the energy transfer dynamics as a function of template length are modelled and lead to further insights about this complex DNA-hybrid system.

Chapter 5

Modelling energy transfer in DNA-hybrid assemblies

5.1 Introduction

To complement the experimental results discussed in Chapter 4, a model was formulated for the ensemble-averaged Förster energy transfer rates between the naphthalene donors and Cy3.5 acceptors. This was based on assembly geometries extracted from molecular dynamics simulations of the DNA-templated structures. In Chapter 4, the dependence of energy transfer on temperature and DNA-template length was found to affect profoundly the extent to which the DNA template is populated with an ordered array of donors. Especially complex was the counteracting effects of inefficient filling of short templates and a reduction in energy transfer due to long donor-acceptor distances in the case of long templates. It is this latter effect that shall be explored in this chapter.

5.2 Elucidation of assemblies' structure

5.2.1 Molecular modelling

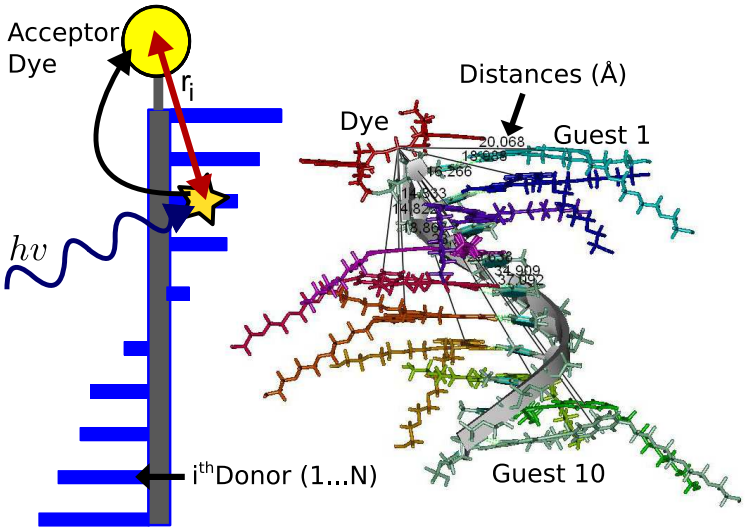

Figure 5.1: Left. Schematic depiction of the approach used in the model describing the Förster resonance energy transfer in the DNA-templated complexes. The grey strip is the oligothymine template, each blue rectangle represents an NP donor, and the yellow circle is the acceptor Cy3.5 dye. Random excitation of an NP chromophore is followed by possible energy transfer to the Cy3.5 dye positioned at the DNA end. Right. Example of a geometry-optimized structure for the 10-base DNA-assemblies extracted from molecular simulations, as described in the text. The counter-ions are not shown for the sake of clarity. The geometries obtained for the systems were used to extract the distances r_i between the *i*-th NP chromophore and the Cy3.5 dye centre which were used for the calculation of the individual transfer rates.

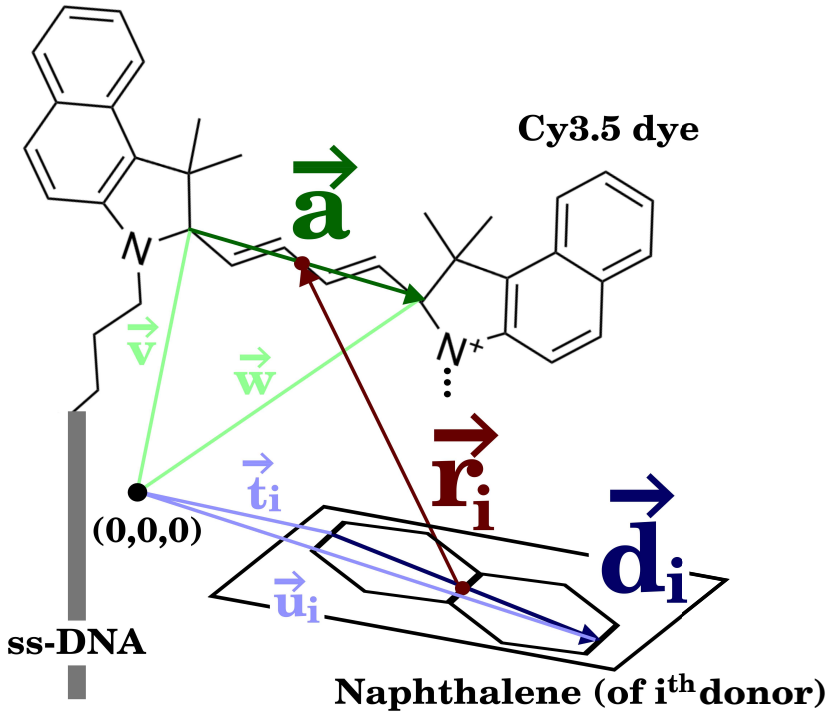

Figure 5.2: Schematic of the donor-acceptor complex structure consisting of a Cy3.5 dye covalently bonded to the end of a strand of 40 thymine bases. 40 naphthalene chromophore donors are arranged at intervals along the length of the strand. The acceptor absorption transition dipole across the polymethine bridge is represented by $\vec{a}$; the ith donor emission transition dipole across the long axis of the ith naphthalene, by $\vec{d}_i$; the distance from the center of the acceptor dipole to the center of the ith donor dipole $\vec{r}_i$, which was extracted from the shown atomic positions using $\vec{r}_i = \frac{1}{2}\left[\vec{w}+\vec{v}-\left(\vec{t}_i+\vec{u}_i\right)\right]$.

Simulations have been performed of Förster energy transfer from individual NP donors to Cy3.5 acceptors using geometry-optimised structures of the DNA-templated assemblies extracted

from molecular modelling. These calculations were carried out on systems made of 10 – 40 oligomer donors, each being hydrogen-bonded to a thymine base of a single-stranded DNA. The single-stranded DNA was end-capped with the cyanine-based molecule Cy3.5 covalently bonded to the final phosphate group. The starting structures of both the guest and the dye were built in extended conformation. The ssDNA structure was constructed in the canonical B-helix structure with sodium (Na+) counter-ions along the phosphate backbone and the stack of guests was built in Watson-Crick base pairing, following the simulations described in Ref 198. Molecular Dynamics simulations were carried out using the CHARMM force field in the canonical ensemble at 288 K (Berendsen thermostat) in implicit solvent model on a 10 nanoseconds timescale with a 1 femtosecond time step. Figure 5.1 shows a geometry-optimised starting conformation for the 10-base complex, which has been used to construct longer assemblies and model the transfer rates.

5.2.2 Extraction of atom coordinates using visual molecular dynamics (VMD) software

To model the energy transfer dynamics the real geometric assembly geometry of the complexes was taken into account by calculating donor-acceptor distances r_i and orientation factors κ_i for each donor-acceptor pair. For this purpose, the vectors representing each donor dipole moment direction, $\vec{d_i}$, the acceptor dipole moment, $\vec{a}$, and that connecting the centres of these moments, $\vec{r_i}$, were determined using atom positions, relative to a common origin, in

the geometry-optimised 40-donor complex from molecular simulations; see Appendix B for a list of the extracted coordinates. Figure 5.2 illustrates how these vectors were extracted for a particular i-th base donor and acceptor combination. For the calculations of the energy transfer dynamics described in Section 5.3, r_i and κ_i were determined from these vectors using

$$\kappa_i^2 = \left[\frac{\vec{a} \cdot \vec{d_i}}{\|\vec{a}\| \, \|\vec{d_i}\|} - 3 \frac{(\vec{d_i} \cdot \vec{r}_i) \, (\vec{a} \cdot \vec{r}_i)}{\|\vec{d_i}\| \, \|\vec{a}\| \, \|\vec{r}_i\|^2} \right]^2 \quad \text{and} \quad r_i = \|\vec{r}_i\| \tag{5.1}$$

where $\|\vec{a}\|$ is the norm or length of a vector $\vec{a}$; see Equation 2.12 in Chapter 2. The geometry-optimised assembly, shown on the right in Figure 5.1, was inputted into the visual molecular dynamics (VMD) program. This program has been specifically designed to display and analyse large biomolecular molecules and polymers[84]. From the VMD-displayed molecular model of the DNA-assemblies, atom coordinates were extracted. Figure 5.3 indicates how the DNA-assemblies appear in the VMD program.

Table 5.1 lists the values of r_i and κ_i obtained in this manner for the modelled assembly containing n=40 bases. It is interesting to note that for the realistic simulated structure examined here, the first NP of the template is not necessarily the closest to the Cy3.5 acceptor dye. Furthermore, full Molecular Dynamics simulation of the 10-base system on the 10 ns timescale reveals the structure globally collapses, i.e. the diaminopurines of the donors do not strictly remain H-bonded in Watson-Crick arrangement because of the base-flipping, naphthalene reorientation, and coiling of the ethylene oxide groups.

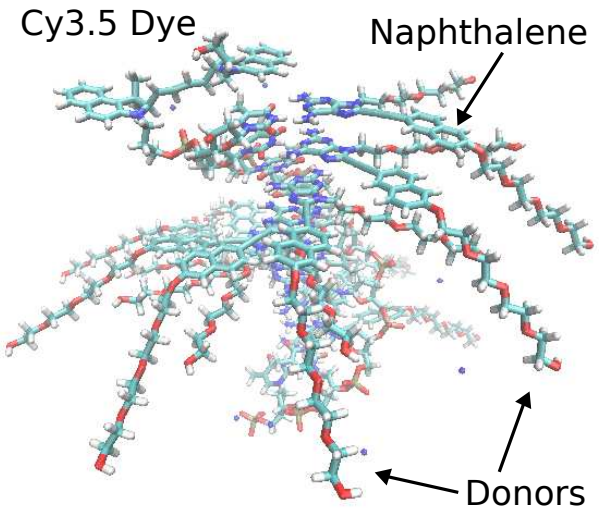

Figure 5.3: The geometry-optimised DNA-hybrid assemblies, in this case a 10-base complex sample (NP-T*10*-Cy3.5), visualised via the visual molecular dynamics program. The individual atom positions in the structure can be readily identified.

5.3 Modelling procedure

5.3.1 Summing over Förster contributions across the DNA assembly

In order to isolate the dynamics of donor de-excitation due strictly to energy transfer, the total emission intensity I_{total} was calculated:

$$I_{total}(t) = \frac{1}{N}\sum_{i=1}^{N} I_i(t), \tag{5.2}$$

where $I_i(t)$ is the contribution from the ith NP donor on the template. For each individual donor, the energy transfer rate is given by Equation 2.10, with the individual donor-acceptor distances r_i being defined as the distance from the centre of the Cy3.5 acceptor electronic transition dipole to the centre of the naphthalene chromophore transition dipole contained in each donor:

$$I_{total}(t) = \frac{I_0}{N} \sum_{i=1}^{N} \exp\left(-\frac{t}{\tau_D^{RAD}} \left(\frac{R_{0,i}}{r_i} \right)^6 \right). \tag{5.3}$$

Here, τ_D^{RAD} is the intrinsic or *radiative* lifetime of donors in the absence of acceptors, and $R_{0,i}$ is the distance at which energy transfer between the ith donor and the acceptor is as likely to occur as *radiative* recombination of the donor exciton[59].

5.3.2 The Förster radius for each donor

The radiative Förster radius $R_{0,i}$ for each donor i was calculated using[59]

$$R_{0,i} = \left[\frac{9000 \ln 10}{128\pi^5} \frac{\kappa_i^2}{n^4 N} \int_0^\infty \frac{1}{\bar{\nu}^4} f_D(\bar{\nu}) \varepsilon_A(\bar{\nu}) d\bar{\nu} \right]^{\frac{1}{6}} = \rho_0 \kappa_i^{\frac{1}{3}} \tag{5.4}$$

Here, κ_i^2 is the dipole orientation constant for the ith donor with respect to the acceptor, n is the refractive index of the material at the peak of the integrand, N is Avogadro's constant, $f_D(\bar{\nu})$ is the fluorescence spectrum of the bound NP donor with integrated intensity normalised to unity on a wavenumber scale, and $\varepsilon_A(\bar{\nu})$ is the molar decadic extinction coefficient of the acceptor (1.5×10^3 Lmol^{-1}cm^{-1} at the peak of the spectrum)[59, 75]. The integral depending on donor emission and acceptor absorption was determined by discrete summation over the experimental data products and also (in order to estimate the errors borne of this method) by numerical integration of functions fitted to the donor and acceptor spectra, which yielded very similar results. The refractive index n was taken to be 1.33 — that of bulk water — as done previously for the

case of fluorescein[146]. Substituting these for parameters in Equation 5.4 returns a value of $\rho_0 = 31 \pm 1$ Å.

κ_i^2 is related to the relative orientation of the acceptor absorption and i^{th}-donor emission transition moments. The lowest-energy singlet absorption and emission transitions in naphthalene are polarised along the long axis of the molecule, a ^1L_b state in Pariser notation[150]. This was established in the late 1950s[157, 117, 141, 149, 44] and has been supported by more recent experimental[25] and theoretical[73, 190] investigations. For cyanine dyes, the π-π^* transition moment lies along the in-plane long axis of the molecule defined by the polymethine chain[85, 86, 127, 148, 165]. If the donor or acceptor re-orient rapidly within the lifetimes of their excited states, then the value of κ^2 for this system is $2/3$; otherwise, a range of values are obtained depending on the relative donor-acceptor pair orientation[136, 75]. Several past studies on systems with cyanine dyes attached to ss- or ds-DNA via a flexible 3 or 6 carbon tether have explored the attachment mode of these dyes. Experiments have probed the activation energies of the isomerisation of free and tethered cyanine dyes[135, 72], the anisotropy of tethered dyes[146, 172, 165], and the modulation of FRET efficiencies after varying the number of base pairs between cyanine dyes attached to opposite ends of a DNA helix[85]. The emerging consensus is that cyanine dyes stack rigidly across the terminal base pair of the DNA similar to the way an additional base pair would[86]. The dye is held in position by a combination of hydrophobic and attractive electrostatic forces[146, 69], and π-π stacking, especially for purine bases[71]. Hence, a separate κ_i^2 value is calculated for each donor-acceptor pair such that the specific geometric arrangement for each naphthalene donor dipole and the acceptor dipole pair

is preserved:

$$\kappa_i^2 = \left[\hat{a}\cdot\hat{d}_i - 3(\hat{a}\cdot\hat{r}_i)(\hat{d}_i\cdot\hat{r}_i)\right]^2 \tag{5.5}$$

Here, $\hat{a}$ and $\hat{d}_i$ are unit vectors in the direction of the acceptor and ith donor transition dipoles, respectively, and $\hat{r}_i = \vec{r}_i/r_i$ is the unit vector in the direction connecting the centre of the acceptor dipole and the centre of the ith donor dipole, where $r_i = \|\vec{r}_i\|$ is the donor-acceptor dipole separation as used in Eqn. 5.3. These vectors are determined by using atom positions, relative to a common origin, in the geometry-optimised 40-donor complex from molecular simulations; see Section 5.2.2. Figure 5.1 shows as an example the calculated structure for a shorter 10-unit complex for ease of viewing. Thus, the calculated κ_i^2 values obtained from this procedure reflect the real structure of the complexes.

τ_D^{RAD} was calculated from the experimentally determined lifetime τ_D of the excited donor using $\tau_D = \eta_D \cdot \tau_D^{RAD}$, where η_D is the quantum yield of the bound NP donors. The quantum efficiency of the bound donors, η_D, used in the calculations was determined using $\eta_{15^\circ C} = 0.25\eta_D + 0.75\eta_{50^\circ C}$ in representation of the relative presences of bound and free donors in solution at low temperature, where $\eta_{15^\circ C}$ is the quantum efficiency measured for the solutions at 15°C and $\eta_{50^\circ C}$ that measured at 50°C, yielding η_D=0.9. The quantum efficiencies were obtained by measuring the power entering and exiting the samples for different temperatures.

Eqn. 5.3 realistically assumes that each NP on the template has, on average, the same probability of being excited. Subsequently, energy transfer causes a decay in the excited-NP ensemble population, which leads to a non-random distribution as donors close to the acceptor

transfer their excitation faster than those further away.

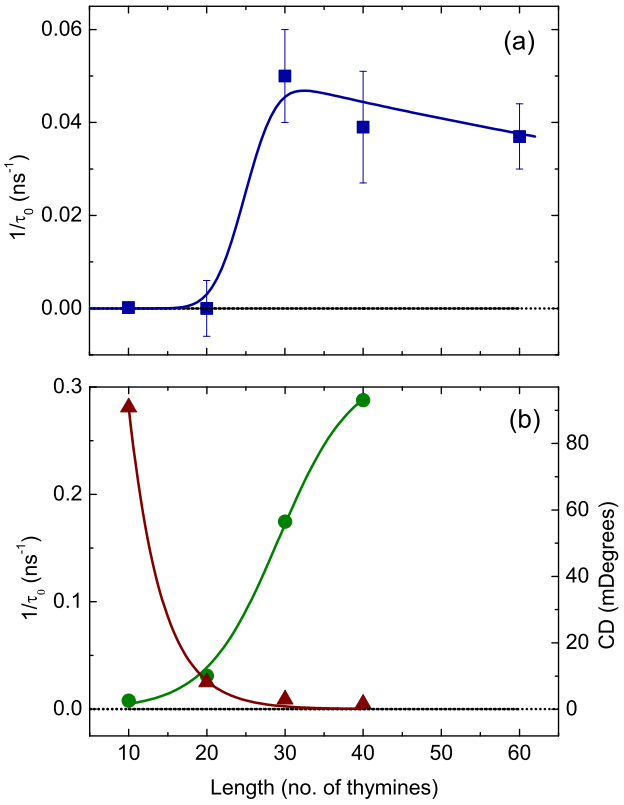

Figure 5.4: (a) Energy transfer rate constant τ_0^{-1} extracted from stretched-exponential fits to the energy transfer dynamics shown in Figure 4.9, plotted as a function of the number *n* of oligothymine bases forming the template. (b) Green filled circles: Circular dichroism signal at 354 nm as a function of oligothymine length *n* at 15°C. Maroon filled triangles: values for the energy transfer rate constant extracted from a model based on Förster energy transfer in complexes whose structure had been determined through molecular dynamics simulations, as described in the text. The rate constant was obtained by fitting stretched exponentials to the simulated energy transfer dynamics and is plotted as a function of oligothymine length. The solid lines are guides to the eye.

The ensemble transfer rate thus decreases with increasing time after excitation as only those excitations survive that are located far from acceptors[75, 76]. Hence, these effects cause a time-dependence in the ensemble transfer rate, as observed experimentally for these samples.

5.3.3 Modelling specifics

In order to obtain the simulated energy transfer dynamics for the donor, Equation 5.3 was evaluated at 0.02 ns intervals between 0 and 6 ns, using donor-acceptor distances derived from the $\vec{r}_i$ vectors and κ_i^2 values evaluated from Equation 5.5; see Table 5.1 for a list of $\|\vec{r}_i\|$ and κ_i^2 values. Donor de-excitation curves were calculated for template lengths n ranging between 10 and 40 with corresponding τ_D^{RAD} values of 1.95 ns to 3.03 ns. The resulting curves are displayed in Figure 5.5(b) together with the experimental data (Figure 5.5(a)). The calculated curves again show stretched-exponential behaviour, however, they appear to show a much more pronounced dependence on template length than the experimental curves. To allow comparison of numerical values Equation 4.11 was also fitted, with $d = 0.6$, to the simulated donor decay curves. The values extracted for the energy transfer rate constants, τ_0^{-1}, are given in Table 5.2 together with those previously determined from experimental data (see Figure 5.4(a)).

5.4 Results: experimental vs. calculated rates of energy transfer

The calculated rate of energy transfer was plotted in Figure 5.4(b) (maroon triangles) to highlight the strong influence of template length on energy transfer in the system. These theoretical

values of τ_0^{-1} decline sharply for template lengths $n \geq$10-20. Hence, the energy transfer is very fast for the short templates, assuming that they are fully populated with donors. However, as the distances between the donor and acceptor increase, the rate of energy transfer drops. The sharp onset in the CD amplitude (Figure 5.4(b), green filled circles) was discussed in Section 4.4.5 in the previous chapter. The resulting interplay between completeness of assembly and donor-acceptor separation thus leads to the observed peak in energy transfer rates around $n \sim 30$ in these systems.

Figure 5.2 and Figure 5.5 clearly show that the calculated transfer rate, $\tau_{0,Calc}^{-1}$, overestimates the experimental transfer rate, $\tau_{0,Exp}^{-1}$, for the shortest template length; and underestimates it for the longer template lengths. The former is not unexpected because the model is insensitive to effects of disorder, due to poorly formed assemblies, slowing energy transfer in the assemblies. Hence, $\tau_{0,Calc}^{-1}$ is too high in particular for the shorter (10-20 base) templates, for which such effects are strong. However, one would expect experimental and simulated values to converge for long template lengths, for which the assemblies are expected to be fully formed and well-ordered[95]. The point-dipole approximation incorporated into the Förster model may be inappropriate for the fraction of donor molecules very near to the acceptor molecule as the donor-acceptor distances here become comparable to the extent of the excitations themselves[180, 22]. However, such effects are likely to be insignificant for the longer (40-base) templates for which most donors are far from the acceptor.

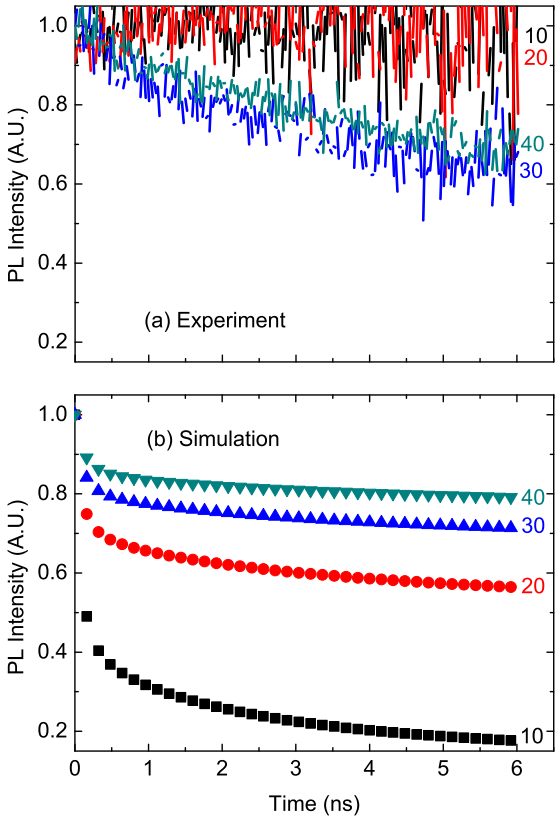

Figure 5.5: (a) Experimental and (b) calculated energy transfer dynamics for complexes containing oligothymine templates of lengths ranging from 10 to 40 bases. The calculated curves were extracted from the model described in this chapter.

Bimolecular processes such as exciton-exciton annihilation have been shown to have an effect on excitation transfer dynamics[45], however, the low laser fluence used to excite the samples in our study means that such processes are highly unlikely to occur. Most likely, excitation transfer between donors along the direction of the template contributes to the energy transfer to the assembly end. Such donor homo-transfer of excitations has been observed and modelled for

non-templated, hydrogen-bonded chiral assemblies of conjugated molecules[21, 34] for which it was shown to depend strongly on the extent of order in the assembly. Transfers of this kind may be either dominated again by dipole-dipole coupling between transition moments confined to individual donor chromophores[179] or be of a semi-coherent type, involving delocalisation of excitations across more than one donor molecule[21]. Comparison between the simulated and measured energy transfer rates (Table 5.2) suggests that for the longer ($n \geq 40$) templated assemblies such effects become increasingly significant and therefore need to be included in more comprehensive theoretical modelling.

5.5 Conclusion

This chapter and the previous chapter show that energy transfer in DNA-templated assemblies is influenced by a number of complex factors. Adoption of these materials for nano-scale sensors and wires thus requires an understanding of the processes that lead to cooperative assembly and order, and their influence on the transfer of excitations within these systems.

i	r_i (nm)	κ_i^2	i	r_i (nm)	κ_i^2
1	1.95	2.40685	21	7.21	0.28361
2	1.98	1.28356	22	7.42	0.00002
3	1.69	0.50905	23	7.63	0.20985
4	1.58	0.62685	24	7.78	0.98464
5	1.60	0.73086	25	8.10	1.19226
6	1.80	0.29898	26	8.40	0.47828
7	1.99	0.06079	27	8.74	0.00006
8	2.42	0.26614	28	9.09	0.22375
9	3.65	0.09963	29	10.00	0.96288
10	3.80	0.28050	30	10.32	0.72603
11	3.92	0.11810	31	10.46	0.31253
12	4.39	0.00050	32	10.62	0.00043
13	4.55	0.18688	33	11.02	0.07953
14	4.54	0.47728	34	11.41	0.97169
15	4.80	0.90628	35	11.44	0.75733
16	5.20	0.18459	36	11.91	0.05555
17	5.44	0.08336	37	12.27	0.00219
18	6.44	0.10414	38	12.78	0.66885
19	6.72	0.88967	39	13.17	1.03577
20	6.92	0.95725	40	13.33	0.73948

Table 5.1: Separations r_i between the center of the dipole on the acceptor chromophore and the center of the dipole on the naphthalene of the i^{th} donor molecule, as shown in Figure 5.2. κ_i^2, which was calculated with Eqn. 5.1, defines the orientation dependence of the acceptor and donor dipoles on the Förster radius as described in the text.

No. of thymines	$\tau_{0,Exp}^{-1}$ (ns^{-1})	$\tau_{0,Calc}^{-1}$ (ns^{-1})
10	$< 10^{-3}$	0.281
20	$< 10^{-3}$	0.025
30	0.050	0.009
40	0.039	0.005

Table 5.2: Experimental and theoretical energy transfer rates constants, $\tau_{0,Exp}^{-1}$ and $\tau_{0,Calc}^{-1}$, obtained upon fitting Equation 4.11 to the energy transfer dynamics shown in Figure 5.5.

Chapter 6

Fluorene-based organic amphiphile nanoparticles

6.1 Introduction

Conjugated nanoparticles (CNPs) are used increasingly to investigate biological systems. Conjugated polymers, oligomers, and a host of molecules suffixed by hydrophobic and hydrophilic tails tend to form CNPs under appropriate conditions. The interactions present, whether π-stacking, Van der Waals, or hydrophobic effects[106], the ratio of hydrophobic to hydrophilic parts of the molecule[105], the side chain and tail architecture[2, 27, 221], and the concentration of molecules present[12] determine the shapes[164] the self-assembled systems adopt. Typical diameters of spherical polymer CNPs are tens of to several hundreds of nanometres[129, 81]. The CNPs have been used to target, track[220], and image specific biomolecules[163]. For example, polymer-loaded surfactant CNPs were functionalised with folic acid to selectively target

and image cancer cells[129]. Utilised as sensors, the CNPs capture the state of the cellular environment, for example, the pH[32] and the oxygen levels[211]. CNPs have several advantages over quantum dots or conventional probes. CNPs are not cytotoxic[81, 211] and do not impair a cell's functionality[225, 163]. If molecular packing is controlled carefully, enhanced emission, rather than quenching, is observed in high concentrations of oligomeric fluorophores in CNPs[106, 27]. Polymeric CNPs have large multiphoton cross-sections[88, 163] and are several orders of magnitude brighter than conventional fluorescent dyes and quantum dots[214] when imaged using multiphoton fluorescence microscopy techniques[49]. These techniques are ideal for use in biological environments due to the high spatial resolution and signal to noise ratio, and the low photodamage[214] they achieve. In this chapter the spectral characteristics and stability behaviour of fluorene-based organic CNPs were determined.

6.2 Samples and experimental details

In this and the next chapter, the properties of amphiphilic fluorene derivatives have been explored, the synthesis of which has been described elsewhere[105]. These amphiphiles incorporate chromophores into their structures, see Figure 6.1 (top), so that separate encapsulated probes, that could perturb the CNP structure[131], are not required. An electron rich naphthalene or an electron-withdrawing benzothiadiazole unit[120, 88] is covalently bonded between two fluorenes, depicted, in Figure 6.1, as a blue or a green disk, respectively, between two yellow squares. Introducing these aromatic molecules does not affect the rigidity of the oligomer backbone[36].

Chiral branched alkane side chains are attached to the fluorenes to prevent photooxidation to 9-fluorenone[3, 6] and to enhance solubility in organic solvents. The hydrophilic ethylene glycol wedges and hydrophobic alkane chains tails are displayed as blue and yellow strands in Figure 6.1, respectively. Amide linkers between the chromophores and the wedges introduce hydrogen bonding as an additional ordering interaction[5].

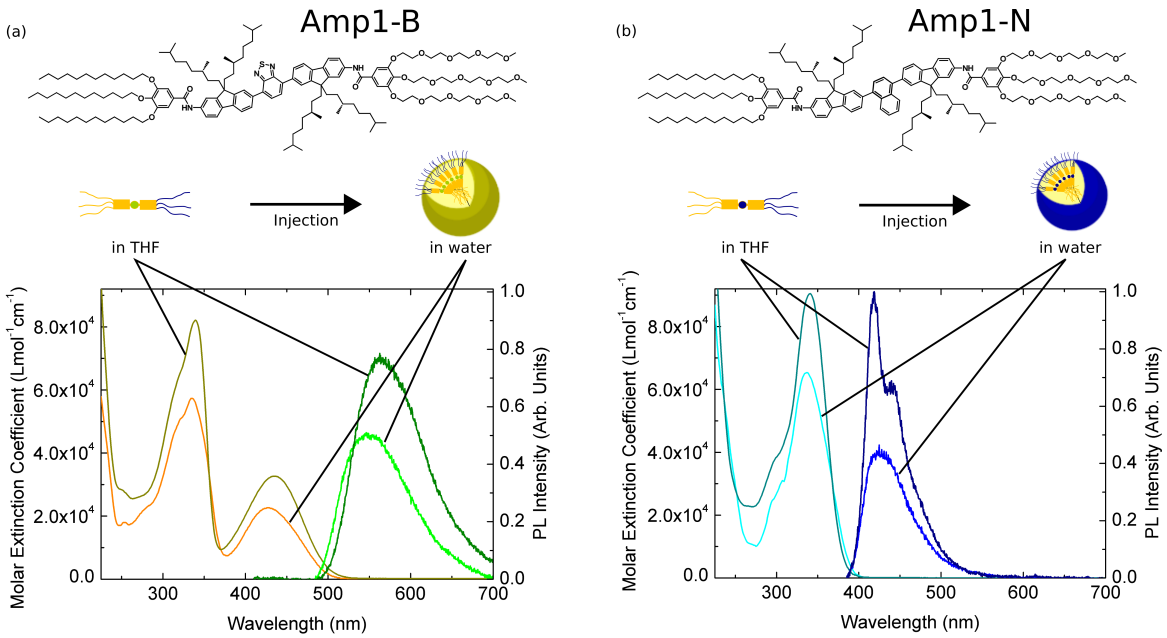

Figure 6.1: Top. Chemical structures of (a) the acceptor (Amp1-B) and (b) the donor (Amp1-N) amphiphiles. Middle. Cartoon representations of a single amphiphile, molecularly dissolved in THF, and a nanoparticle, formed upon injecting the molecularly dissolved amphiphiles into ultrapure water. Bottom. UV-vis and time-integrated photoluminescence spectra of molecularly dissolved amphiphiles in THF and nanoparticles in water. The photoluminescence spectra are scaled so that the peak of the molecularly dissolved donor spectrum, at 419 nm, is set to 1.

Single-component (1CNP) CNPs were manufactured, in such a way that each nanoparticle contained only donor amphiphiles (Amp1-N) or only acceptor amphiphiles (Amp1-B), by the fast injection method[215, 4]. In step 1, shown in Figure 6.2, a 1 mM stock solution was prepared by dissolving donors, or acceptors, in THF. A small amount (15 μL) of each stock solution was injected quickly into a large excess (5 mL) of ultrapure water to yield donor CNPs and acceptor CNPs with diameters of $\sim$80 nm[105] (step 2). Then, the separate preformed CNP solutions were mixed (step 3). Despite the low concentration of the CNP solutions, nanoparticles formed because of the low critical aggregation concentration value[102, 164], in the region of $\sim 10^{-9}$ M. Evidence of CNP formation is given by the TEM image of the acceptor 1CNP in Figure 7.1 in Section 7.2. Additionally, the lack of an edge-type structure indicates that amorphous nanoparticles form.

Room temperature time-integrated photoluminescence (TIPL) and time-correlated single-photon counting (TCSPC) measurements were conducted on the CNPs using the experimental setups described in Ref. 195 and in detail in Chapter 3. The samples were placed in cuvettes with a light path of 10×4 mm on a temperature-controlled stage and excited with 50 μW of a pulsed laser output at a wavelength of 375 nm. The wavelength was chosen to excite predominantly the donor 1CNPs. The collection time of 20 s per TCSPC scan and sample convection due to the reasonably large cuvette volumes negate sample degradation. A 400 nm LED was used to visually inspect the quality of the samples.

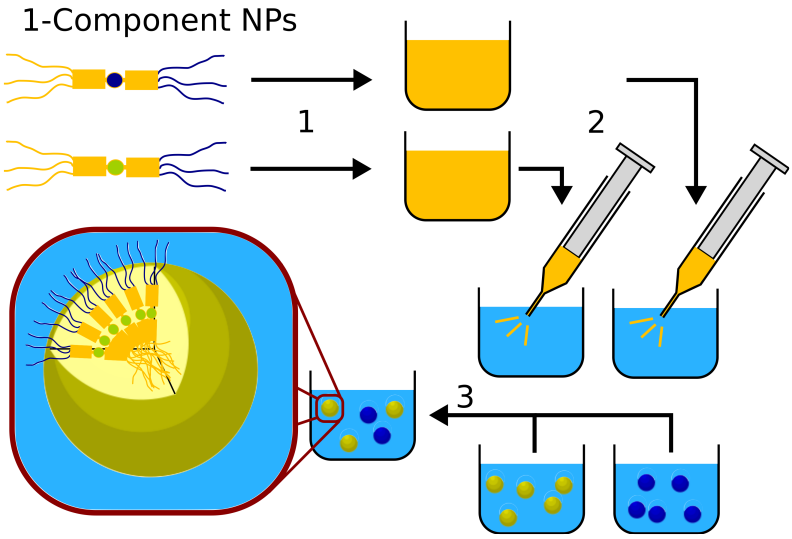

Figure 6.2: Preparation of single-component nanoparticles by the fast injection method. Naphthalene-containing (Amp1-N) and benzothiadiazole-containing (Amp1-B) amphiphiles are shown schematically in the top left corner. An acceptor nanoparticle, with ∼40 nm radius, is depicted in the red square.

6.3 Results and discussion

6.3.1 Forming nanoparticles from molecularly dissolved amphiphiles

The molecularly dissolved stock solutions of acceptors and donors show local absorption peaks in Figure 6.1 (bottom) at 340/435 nm and at 341 nm, respectively. Also identifiable are the photoluminescence (PL) spectra maxima that occur at 562 nm and 419 nm for the acceptor and donor stock solutions, respectively. The molecularly dissolved amphiphiles do not interact with one another[81]. Their spectral characteristics are determined by the bandgaps[2] which are controlled by the chemical structures of the chromophores[4]. Hence, the lower wavelength acceptor

peaks correspond to the π-π^* transition[181] of the fluorene unit; the higher wavelength peaks, the benzothiadiazole ring[4, 208, 213]. The donor peaks correspond to the fluorene-naphthalene chromophore[4, 112, 26, 213, 208] and a vibronic PL red shoulder[81, 181] is visible also.

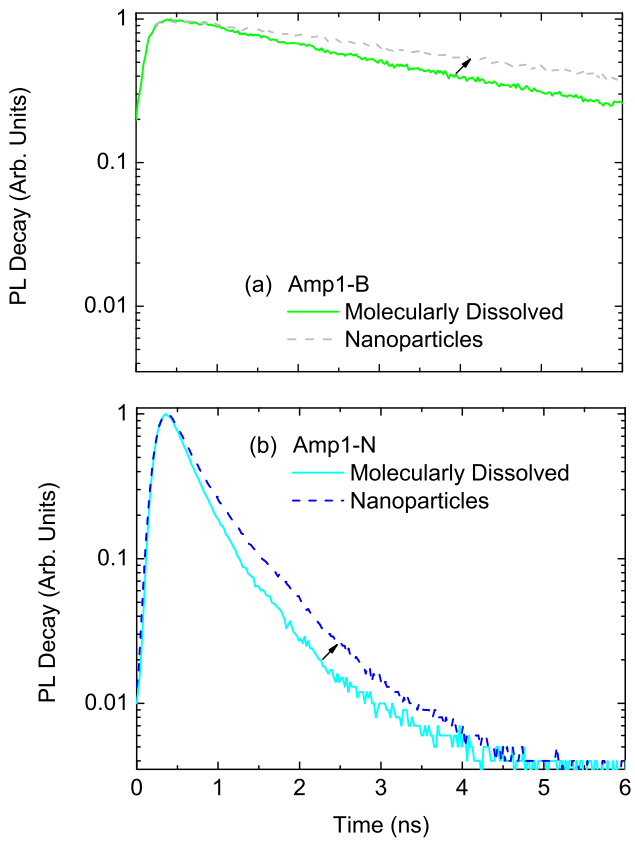

Figure 6.3: Normalised time-resolved photoluminescence decays of amphiphiles molecularly dissolved in THF and of amphiphile nanoparticles in ultrapure water. The detection wavelengths of (a) the acceptor amphiphile emission and (b) the donor amphiphile emission are 545 nm and 430 nm, respectively. Refer to Table 6.1 for lifetimes extracted from these decays.

As detailed in Section 6.2, when a small amount of the nonpolar solutions of these molecules is injected quickly into a large volume of polar solvent the molecules form CNPs. The main driving force for this self-assembling process is the need to reduce the energy of the system by limiting the unfavourable interactions between the amphiphiles' hydrophobic alkane side chains and the polar solvent[102]. More generally, the forces that encourage the amphiphiles to coagulate are hydrophobic and interfacial tension forces at the hydrocarbon-water boundary, and van der Waals and hydrogen bonding forces between the hydrophobic cores[102, 89, 215]. Steric constraints and hydration forces between the hydrophilic-chain ends limit the closeness of approach of the amphiphiles[89]. Equation 2.5 combines elegantly these complimentary forces into the free energy difference of an isolated molecule compared to the energy change when a molecule is taken from bulk and put into an aggregate[102].

Upon attaining a minimum free energy, a thermodynamically-arrested phase separation[102] occurs wherein a certain number of amphiphiles assemble into appropriately-shaped structures[89].

For the amphiphiles studied here, CNPs are formed with radii of $\sim$40 nm[105]. The sensitivity of the confined amphiphiles to the presence of other molecules affects their spectral characteristics. In the acceptor amphiphile case, upon forming CNPs, the absorption peaks blueshift to 335 and 428 nm, the PL peak blueshifts to 546 nm, and the quantum yield stays constant at 85%; see Table 6.2. Peak shifts and intensity decreases in the spectra imply the emergence of an aggregated state in which the adjacent chromophores interact electronically[205, 218]. H-type

	Donor	*Acceptor*
Sample Type	τ_D *(ns)*	τ_A *(ns)*
Molecularly Dissolved	0.372 ± 0.005	3.965 ± 0.159
Nanoparticles	0.451 ± 0.005	6.127 ± 0.303

Table 6.1: Acceptor (τ_A) and donor (τ_D) lifetimes for amphiphiles molecularly dissolved in THF and for amphiphile nanoparticles in ultrapure water. Lifetimes were extracted from the decays shown in Figure 6.3 by fitting a monoexponential function ($y = Ae^{-(t/\tau)}$) from the peak to 1 ns past the peak of the decays.

aggregation is inferred from spectral blueshifts[38, 48, 110]; see Chapter 2. The donor absorption blueshifts to 337 nm, while its PL redshifts to 425 nm and the two-peak vibronic progression is smeared into a single peak[98] upon CNP formation. The peaks all lower in intensity, the Stokes shift increases, and the quantum yield increases from 20 to 40%; see Table 6.2. These observations allude to the establishment of an aggregated[129, 39, 130, 218, 88], dense, glassy phase[212, 213, 99]. Figure 7.4 in Chapter 7 illustrates the circular dichroism (CD) data for the 1CNP donor and acceptor samples as navy and red lines, respectively. A bisignate Cotton effect is observed for both cases, although larger for the acceptor CNPs. It is believed that chiral aggregate domains form[79, 62, 2].

Sample Type	*Donor Quantum Yield (%)*	*Acceptor Quantum Yield (%)*
Molecularly Dissolved	20	85
Nanoparticles	40	85
Annealed Nanoparticles	50	85

Table 6.2: Quantum yields of the amphiphilic molecules, from Ref. 105, in THF (molecularly dissolved), water (nanoparticles), and after a postformation treatment procedure (annealed).

The detection wavelengths of the time-resolved TCSPC measurements were set near the PL emission peaks shown in Figure 6.1, i.e. 545 and 430 nm for the acceptor and donor samples, respectively. Figure 6.3 and Table 6.1 both show that lifetimes increase upon amphiphile aggregation. The acceptor lifetime increases from 4 ns to 6 ns while the donor lifetime increases from 0.37 ns to 0.45 ns upon CNP formation. This is close to a lifetime of 0.33 ns found for another fluorene derivative (poly-dihexylfluorene) CNP with a detection wavelength of 420 nm[216]. An increase in PL lifetimes, accompanied by the multiexponential nature of the decays, is attributed to aggregation and interchain state formation[99, 14]; see Chapter 2. As mentioned above, the donor PL is redshifted which can indicate an increase in the planarity of conjugated backbones upon formation of the solid state[43, 42]. Hence, two counteracting effects are present upon injection of the molecules into a hydrophilic environment: aggregation and planarisation of the molecules. Aggregation lowers the radiative oscillator strength of the molecules leading to longer PL lifetimes and *lower* PL efficiencies, while planarisation reduces the non-radiative recombination pathways available to the molecular excitations. This reduction lengthens the PL lifetimes

but *raises* the radiation efficiencies. The emission efficiencies are evidently the key to unravelling the impacts of these effects on the nanoparticles.

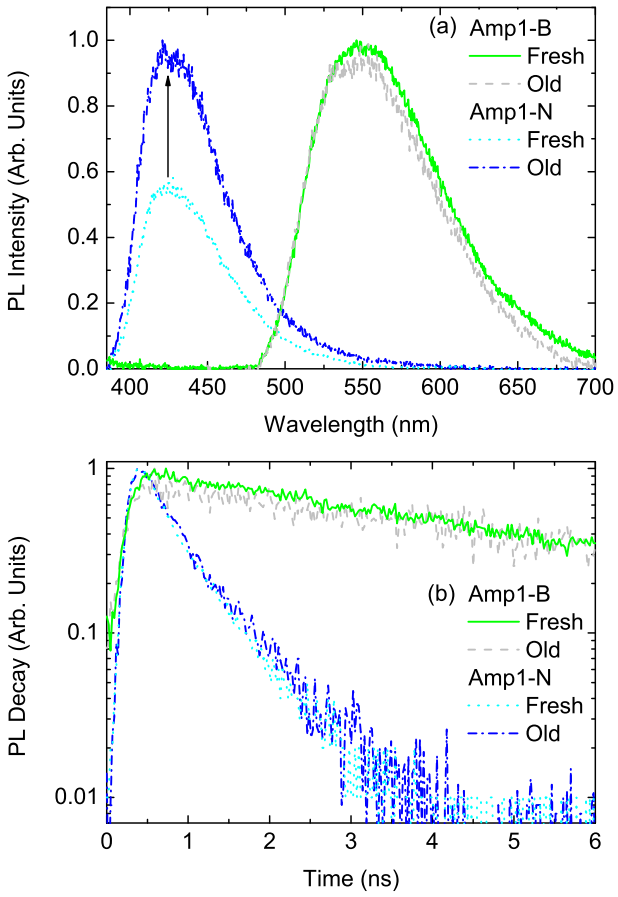

Figure 6.4: (a) Time-integrated and (b) normalised time-resolved photoluminescence spectra of freshly made and 2-week old acceptor and donor nanoparticles. The detection wavelengths of the acceptor and donor amphiphile photoluminescence emission are 545 nm and 430 nm, respectively.

From Table 6.2, the quantum efficiency for the molecularly dissolved acceptor amphiphile is much higher than for the donor. Calculations have established that the torsional angle between the fluorene and benzothiadiazole units ($\sim$40°) is much smaller than between the fluorene and

naphthalene units ($\sim$71°)[200, 5]. The large torsional angle along the conjugated path of the donor molecule promotes an increased intersystem crossing rate, i.e. a larger nonradiative rate, and an accompanying enhanced quantum efficiency. The large twist between moieties enables σ-π orbital mixing that gives rise to efficient spin-orbit coupling[23]. Upon aggregation of the donor amphiphile, a substantial reduction in intersystem crossing rates is expected due to molecular planarisation, in agreement with the enhanced emission observed in the presence of largely unchanged absorption; see Figure 6.1. For the acceptor molecule, aggregation is the dominating effect upon formation of a solid state and the PL lifetime increases with no concomitant increase in quantum efficiency.

6.3.2 Stability of freshly-made nanoparticles

Figure 6.4(a) shows the longer-wavelength and shorter-wavelength acceptor and donor PL spectra, respectively, for fresh samples (tested within 24 hrs. of CNP formation) and old ones (same batch tested 14 days later). Figure 6.4(b) displays the samples' corresponding time-resolved decays. The acceptor time-integrated emission spectra and time-resolved emission transients do not change over the 2 week period. Therefore, the acceptor samples seem stable and resistant to structural changes over this time period. However, the donor emission peak intensity increases over time, while its lifetime remains constant. This hints at some slight structural changes that reorganise the extent to which donors interact with one another.

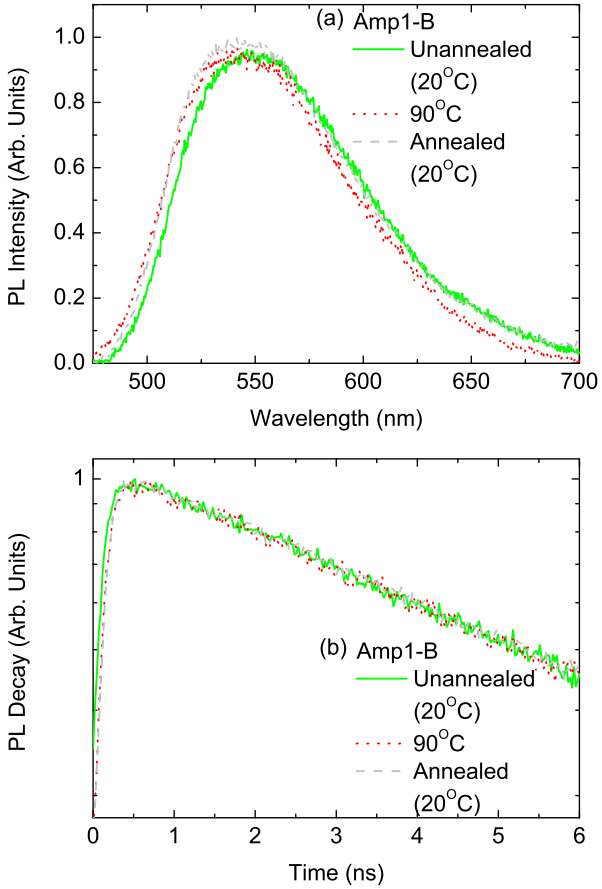

Figure 6.5: (a) Time-integrated and (b) normalised time-resolved photoluminescence of acceptor nanoparticles at 20°C, heated to 90°C during the annealing process, and cooled to 20°C post-annealing. The detection wavelength for the time-resolved photoluminescence decays is near the peak of the acceptor emission at 545 nm.

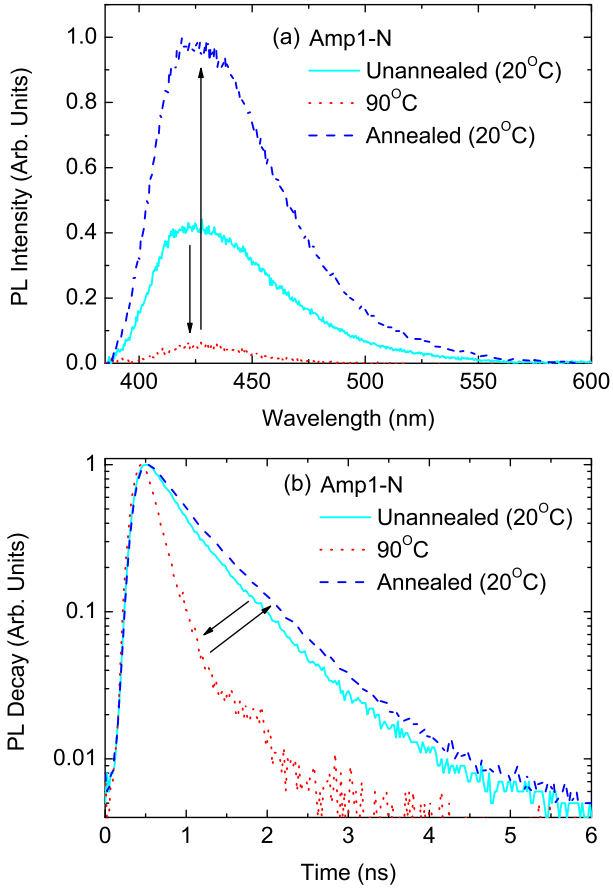

Figure 6.6: (a) Time-integrated and (b) normalised time-resolved photoluminescence of donor nanoparticles at 20°C, heated to 90°C during the annealing process, and cooled to 20°C post-annealing. The detection wavelength for the time-resolved photoluminescence decays is near the peak of the donor emission at 430 nm.

6.3.3 Effect of annealing

The excitation laser beam is blocked during the annealing procedure. The heating stage is turned on and heated to 90°C. The cuvette is placed on the heating stage so that the CNP

sample is heated at 90°C for ∼10 minutes. The cuvette is then removed and the stage is cooled to 20°C. The cuvette is replaced on the sample stage and the sample is measured immediately. Figure 6.5(a) shows the CNP emission spectra for the unannealed acceptor sample measured at 20°C, for the sample during annealing at 90°C, and for the sample after annealing at 20°C. Figure 6.5(b) displays the corresponding acceptor emission decays detected at 545 nm. A small rise and a 5 nm blueshift is revealed by comparing the pre- and post-annealed acceptor PL peaks. However, there is no change in the decay lifetimes or the quantum yield; see Table 6.2. From these results, high acceptor CNP stability upon heating[4] with no pronounced morphological change[2] is inferred, although, the molecules may rearrange slightly.

The annealing procedure, described above for the acceptor samples, was performed on the donor CNPs. Both the emission peak intensities and the emission decays changed substantially upon annealing; see Figure 6.6. The donor peak emission intensity decreases during the annealing process, but is more than double the initial peak intensity post annealing. Additionally, the peak blueshifts by 6 nm and the quantum yield increases from 40 to 50%[105]. In Figure 6.6(b), the donor lifetime drops dramatically during annealing but recovers and lengthens overall after annealing compared to the pre-annealed lifetime. Repeating the annealing procedure does not elicit further change of the emission properties of the donor, or acceptor, CNPs. Increased non-radiative deexcitation pathways produce the emission properties, shown in Figure 6.6, for the donor CNPs at 90°C. The annealing-induced donor lifetime increase suggests that the donors are more tightly bound or that the aggregated regions have increased in size. The emission blueshift precludes planarisation of the units that constitute the amphiphile[3]. Annealed polymer films

show increased PL from interchain species[181]. It is clear that the initially formed metastable state has changed irreversibly into a thermodynamically stable state[2] which involves some large rearrangements of the amphiphilic molecules.

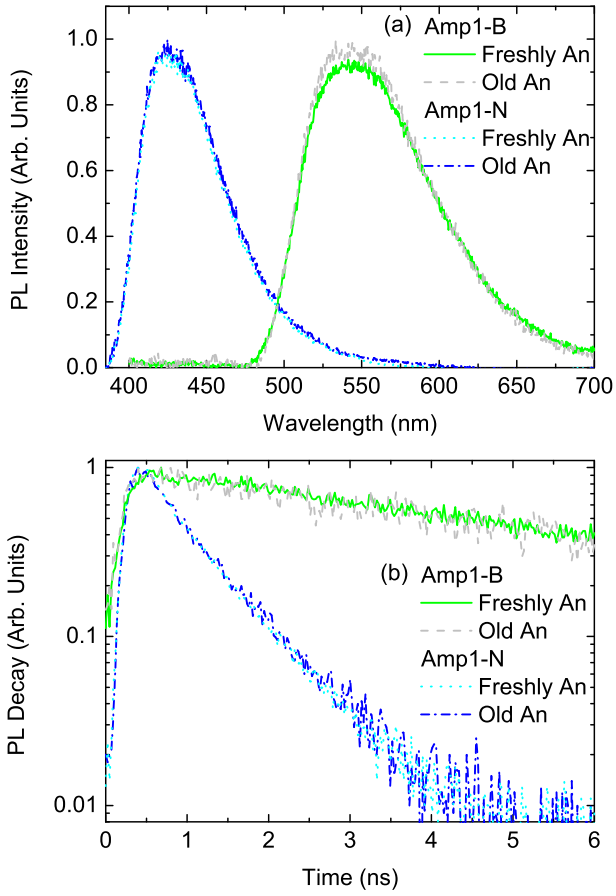

Figure 6.7: (a) Time-integrated and (b) normalised time-resolved photoluminescence spectra of freshly made and annealed, and 9 day old annealed acceptor and donor nanoparticles. The detection wavelengths of the acceptor and donor amphiphile photoluminescence emission are 545 nm and 430 nm, respectively.

Figure 6.7 shows the (a) PL emission spectra and (b) PL emission decay transients for acceptor and donor post-annealed samples. The "Freshly An" samples were annealed within 24 hrs of CNPs being formed and re-tested 9 days later ("Old An"). Annealing increases the stability of the nanoparticles because no PL intensity differences or PL lifetime differences were visible for either the acceptor or donor samples. See Figure 6.4 for a comparison.

6.4 Conclusion

Nanoparticles have been formed from fluorene derivative amphiphiles. The nanoparticles occur as "thin-film-like" untextured aggregates that are dipole-dipole coupled such that π-electrons can delocalise between different chromophores[181, 27, 111, 81]. This was supported by the spectral changes and lifetime increases upon CNP formation. It has been shown that rapid injection can lead to metastable aggregates trapped in less organised structures[199]. However, the CNPs were relatively stable over a period of 2 weeks, which suggests that the interactions between the aggregate amphiphiles are strong[99]. This is certainly the case for the acceptor-type amphiphiles. Upon annealing the donor-type CNPs at high temperatures, the emission spectra and decays changed dramatically. This post-deposition treatment organises the donor amphiphiles into a more thermodynamically stable state[2]. Hence, the emission properties of the annealed CNPs show no subsequent changes after measurements were repeated after 9 days. The electronic properties of the amphiphiles are intricately-related to the arrangement and, hence, the chemical structure of the amphiphiles, including π-conjugation and the interaction

accessibility of the chromophores[3, 171, 181, 37, 48, 200].

Chapter 7

Morphology-dependent energy transfer dynamics in mixed nanoparticles

7.1 Introduction

The Förster radius R_0 — the critical transfer distance for which excitation transfer and spontaneous deactivation are of equal probability — is a useful length in biological, and in particular cellular, environments[59, 75]. Indeed, some biological systems have already been explored through the lens of energy transfer[64, 120, 82, 83, 30, 222, 138] in which molecular packing plays a large role. Hence, in this chapter the effect of oligomer packing on energy transfer has been investigated. Conjugated nanoparticles (CNPs) provide an ideal testing ground because of

the intimate contact of the chromophores.

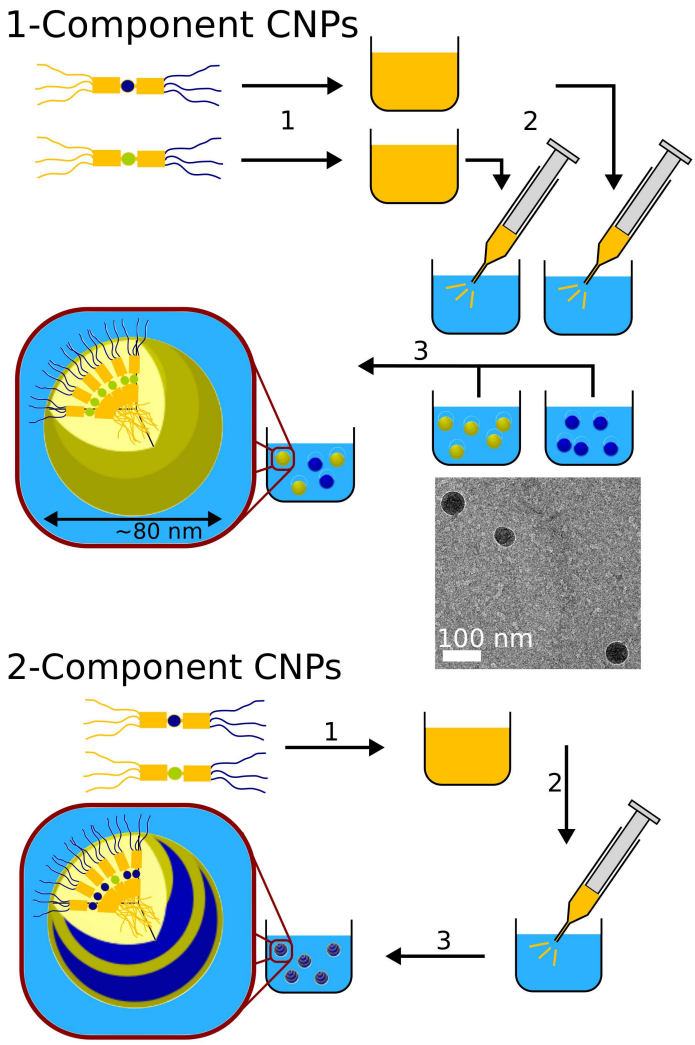

Figure 7.1: Top. Preparation of single-component nanoparticles. Naphthalene-containing and benzothiadiazole-containing amphiphiles are shown schematically in the top left corner and an acceptor nanoparticle, with ∼40 nm radius, is depicted in the red square. The TEM image is of acceptor nanoparticles. Bottom. Preparation of two-component nanoparticles. A mixed nanoparticle, in which yellow and blue bands are used to highlight its mixed composition, is shown in the red square. See text for details.

7.2 Samples and experimental details

The formation of single-component CNPs (1CNPs) was described thoroughly in Section 6.2. It was concluded in Chapter 6 that the amphiphilic molecules aggregate upon being injected into polar solvents with a corresponding increase of photoluminescence lifetimes upon CNP formation. Hence, energy transfer processes will depend not only on the spectral characteristics of the donor-acceptor pair but also on their arrangement[162, 208]. Forming CNPs from our amphiphiles enabled us to study this effect, while simultaneously enhancing their solubility in water[83].

For so-called two-component (2CNP) CNPs, each nanoparticle is composed of a mixture of donors and acceptors. They were formed by injecting mixed stock solutions (with various donor to acceptor ratios) into water, as shown in the bottom of Figure 7.1. The experiments were conducted as described in Section 6.2. However, all the results presented in this chapter are for freshly-made 1CNP and 2CNP samples, i.e. no postformation treatments have taken place, as annealing conjugated oligomer samples changes their organisation[2] and affects their electronic properties[181].

7.3 Results and Discussion

Figure 7.2 displays time-integrated photoluminescence (TIPL) results for (a) 1CNP and (b) 2CNP samples. All the spectra are normalised. For 1CNPs, the donor emission peaks at 425 nm

and the acceptor molecules emit broadly around 550 nm, in agreement with literature[213, 5, 3, 36, 132]. As the acceptor fraction in the CNPs increases, the donor emission decreases with a corresponding acceptor emission increase.

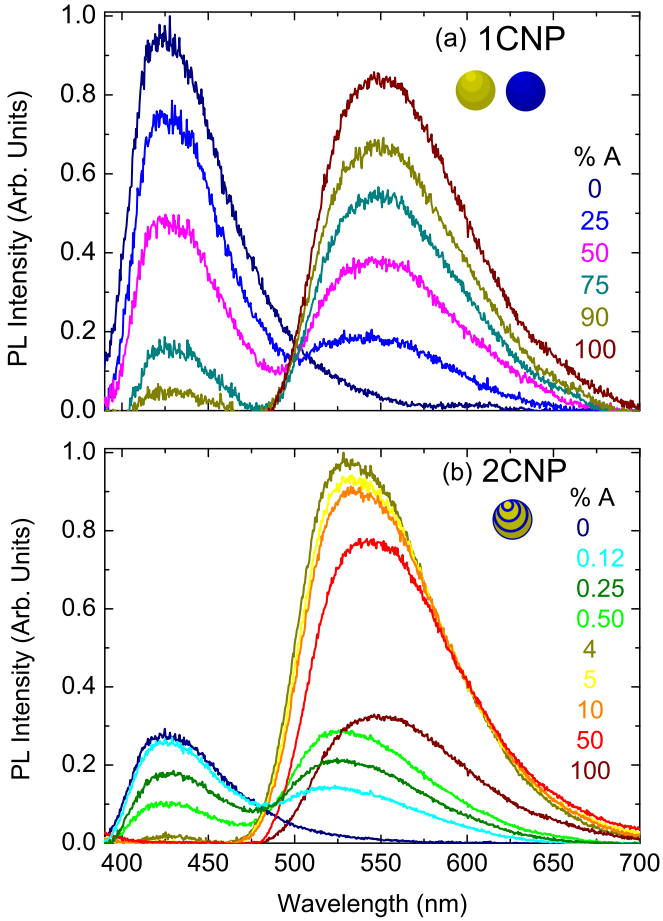

Figure 7.2: Normalised time-integrated photoluminescence spectra of (a) freshly-made single-component nanoparticles (1CNP) and (b) freshly made two-component nanoparticles (2CNP) as a function of the percentage of acceptor molecules present. The samples were excited at 375 nm.

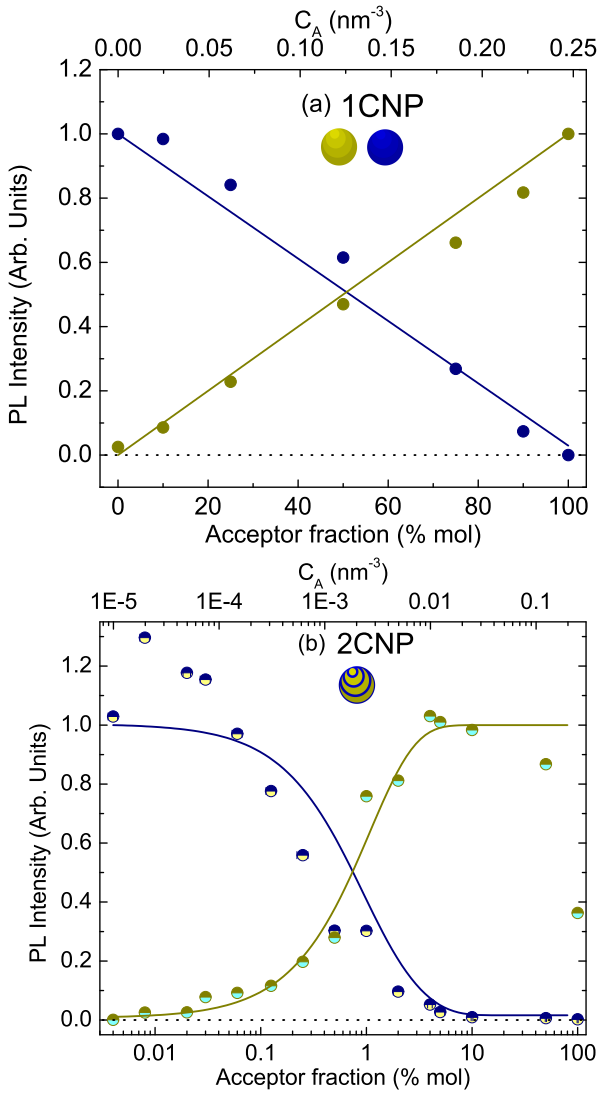

Figure 7.3: Time-integrated photoluminescence intensities at donor ((a) blue; (b) navy/yellow) and acceptor ((a) yellow; (b) dark yellow/cyan) emission wavelengths (430 nm and 575 nm, respectively) as a function of acceptor percentage in (a) single-component nanoparticles (1CNP) and (b) two-component nanoparticles (2CNP). The acceptor concentration (C_A) at each acceptor percentage is shown. The fitting curves (solid lines) have been normalised in (a) and (b).

No peak shifts are visible. For 2CNPs, the donor emission peaks at 425 nm and rapidly reduces in intensity upon introduction of acceptors until, at an acceptor fraction of 2%, it can no longer be resolved. At low acceptor fractions ($<$0.5%), the 2CNP acceptor peak is at 525 nm with an intensity similar to that of the donor peak. The acceptor intensity peaks at 4%. Beyond that maximum, the lower acceptor peaks redshift to 550 nm.

To probe the concentration-dependent evolution of the nanoparticle PL intensities in more detail, the PL intensities were plotted at two wavelengths (see Figure 7.2) as a function of the percentage of acceptors present in the sample. The navy and yellow disks in Figure 7.3(a) are the 1CNP PL intensities at 430 nm and 575 nm, respectively. The acceptor concentration (C_A) depends on the number of moles of acceptor and donor per sample and assumes an CNP density of a polymer film ($\sim$1 gcm^{-3})[133]. The lines in Figure 7.3(a) are fits to the experimental data and cross at an acceptor fraction of 50%. This is expected if the difference in quantum yields of the acceptors and donors have been ignored by appropriate scaling and there are no energy transfer processes occurring[4].

In fact, the favourable overlap between the donor-only emission spectrum (Figure 7.2(b), navy curve) and the acceptor-only absorption spectrum (Figure 7.4(a), yellow curve) should promote energy transfer and yield a large Förster radius. Förster theory was applied to the CNPs since their diameters are much larger than exciton diffusion lengths in organic films[183, 213]. Stern-Volmer quenching theory has been applied to CNPs[14] also but is less appropriate when the small numbers of acceptors present result in significant particle-to-particle variations in

quenching efficiency[213]. Hence, the Förster radius, cf. Equation 5.4, was invoked. The CNPs resemble an amorphous polymer film, which has a refractive index of 1.5[133, 40] and a κ^2 value of 0.48[136, 15]. In this case, the Förster radius for donor-acceptor transfer is 2.9 nm, consistent with dye-incorporated CNP systems[216], and for donor-donor homotransfer is 1.5 nm; see Table 7.1. The low concentration of CNPs in water (3 μM) implies that interparticle donor to acceptor energy transfer is not possible[213, 212]. Therefore, no energy transfer occurs in the 1CNP samples.

Transfer Type	n	κ	R_0^{RAD} *(nm)*	Φ_D	R_0 *(nm)*
D–A	1.5	$0.845\sqrt{2/3}$	3.4	0.4	2.9
D–D	1.5	$0.845\sqrt{2/3}$	1.7	0.4	1.5

Table 7.1: Radiative Förster radius (R_0^{RAD}) and total Förster radius (R_0) of the nanoparticles calculated from the overlap of the donor's emission spectrum and the acceptor's absorption spectrum, with variables that include the refractive index (n), the orientation of the acceptor and donor dipole moments (κ), and the quantum yield of the donor (Φ_D).

The donor peak 2CNP PL intensities from Figure 7.2(b) are plotted in Figure 7.3(b) (disks with navy exteriors and yellow interiors). To arrive at intensities for the acceptors, the donor peaks were removed from the PL spectrum for each CNP acceptor fraction, by scaling the 100% donor time-integrated PL spectrum to the donor peaks of the other ($<$100% donor)

spectra before subtracting the first from the latter. After integrating the remaining spectra, the outcome is Figure 7.2(b) — see the cyan disks with dark yellow circumferences. This achieves greater accuracy than choosing the intensity values at a fixed acceptor emission wavelength, by compensating for redshifting of the acceptor peak. The data deviates from the linear case of the 1CNPs and the donor and acceptor data cross at an acceptor fraction of 0.7–0.8%. This enhancement of acceptor emission and quenching of donor emission is due to efficient intraparticle energy transfer. In order to extract a Förster radius, functions based on an ensemble of donors and acceptors randomly distributed and integrated over time[161]

$$\phi_D(X) = B\left(1-\left[\sqrt{\pi}Xe^{X^2}(1-\mathrm{erf}(X))\right]\right) \tag{7.1}$$

$$\phi_A(X) = B\left(\sqrt{\pi}Xe^{X^2}(1-\mathrm{erf}(X))\right), \tag{7.2}$$

were fitted to the donor and acceptor 2CNP data, respectively; see equations 2.16, 2.17. B is a scaling factor; Φ_D and Φ_A are the radiative efficiencies of the donors (in absence of acceptors) and acceptors (in absence of donors), respectively; and $X = 3.71R_0^3C_A$. The donor and acceptor fits are shown in Figure 7.3(b) as navy and yellow lines. The corresponding Förster radius, 3.97 $\pm$ 0.03 nm, implies very efficient energy transfer above that calculated for the spectral overlap of the molecules. In other CNP systems, the observation of greatly enhanced acceptor emission under small incorporation amounts[208, 213, 79, 46, 83] informs the conclusion that each acceptor quenches many donors[213, 222].

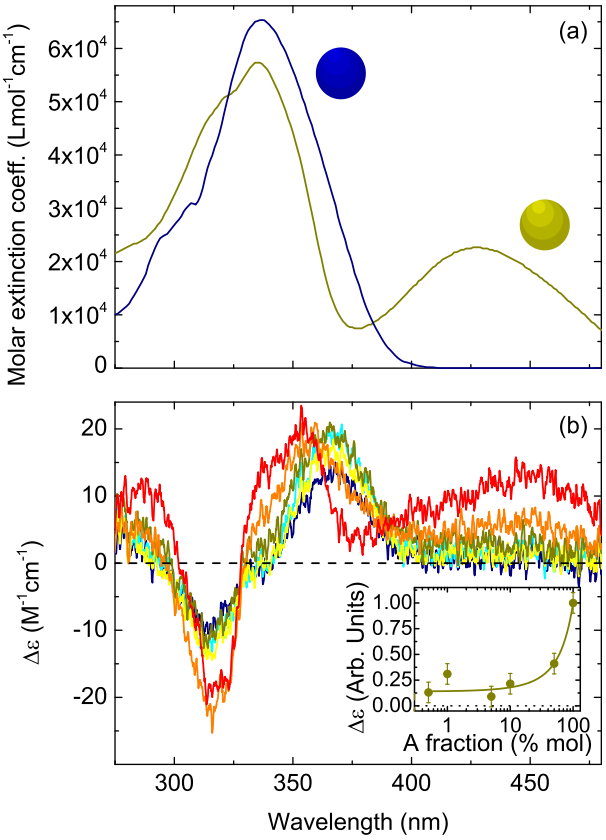

Figure 7.4: (a) UV-Vis absorption spectra of the 100% donor amphiphile-containing nanoparticle (navy line) and the 100% acceptor amphiphile-containing nanoparticle (yellow line). The cartoons depict the spherical nature of the nanoparticles. (b) Molar circular dichroism data of two-component nanoparticle (2CNP) samples as a function of wavelength. The navy, cyan, yellow, dark yellow, orange, and red lines correspond to acceptor fractions of 0, 0.5, 5, 10, 50, and 100%, respectively. The inset shows the normalised integrated $\Delta\varepsilon$ intensities of the 2CNPs from 430 nm to 500 nm, i.e. from the acceptor absorption peak.

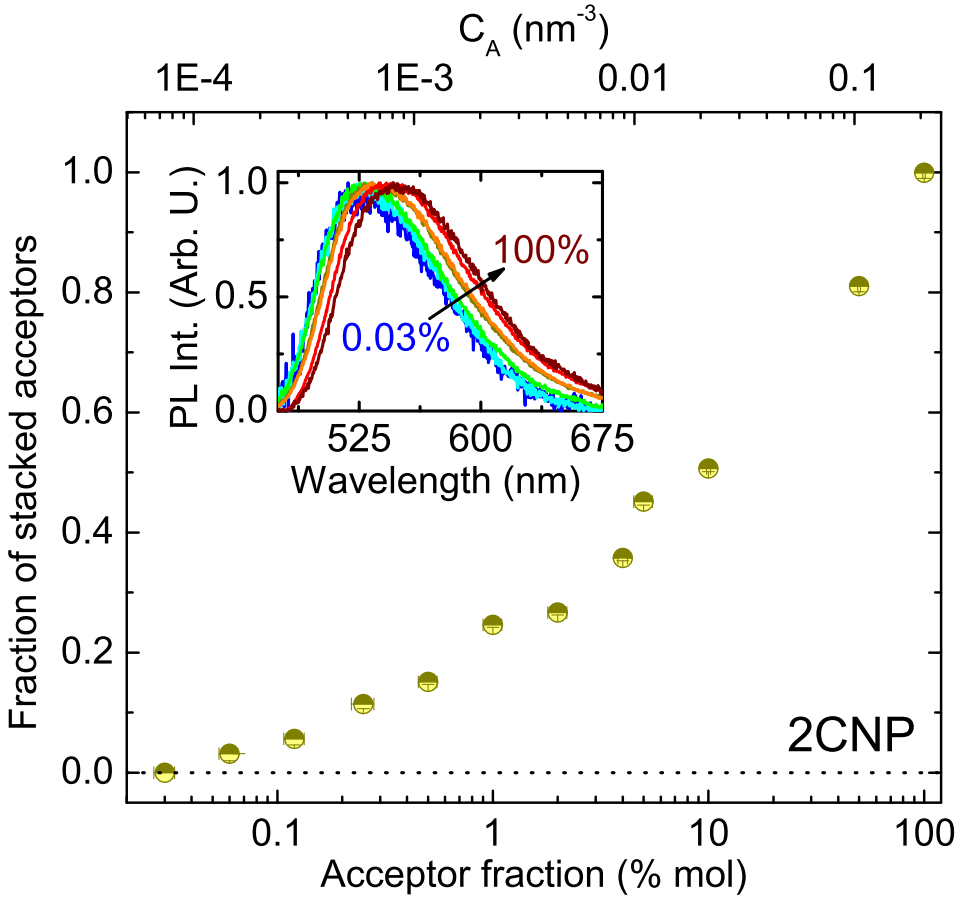

Figure 7.5: The fraction of stacked acceptors in two-component nanoparticles as a function of acceptor percentage and acceptor concentration. The donor proportion of the nanoparticle time-integrated photoluminescence spectra has been removed and the resulting spectra normalised, as shown in the inset. These spectra are then fitted with a sum of "stacked" acceptor and "unstacked" acceptor functions from which the proportion of stacked acceptors can be extracted.

Next, the acceptor peak shifts in Figure 7.2 were investigated. To isolate acceptor-only effects, the same procedure as for the intensity study was used. However, instead of integrating,

the resulting spectra were normalised (inset of Figure 7.5). There is a distinct redshift of the spectra as the acceptor fraction increases. The 0.03% acceptor spectrum is defined as representing the acceptors dispersed evenly throughout the mostly-donor CNPs; the 100% acceptor spectrum, fully stacked acceptors in the CNPs. The normalised spectra of various acceptor fractions were then fitted with

$$[A_1 \times (100\% \text{ stacked spectrum})] + [A_2 \times (0.03\% \text{ unstacked spectrum})] \tag{7.3}$$

where A_1 and A_2 are amplitudes. The fraction of stacked acceptors is $\frac{A_1}{(A_1+A_2)}$, which is shown in Figure 7.5 in terms of acceptor fraction and acceptor concentration.

At low acceptor concentrations, the acceptors are uniformly distributed in the donor CNPs[213]. At high acceptor fractions, the pronounced redshift and PL intensity decrease suggest that low energy, weakly fluorescent aggregates have formed[129, 81, 83, 79, 205, 39, 218, 181, 216, 110, 111] due to π-π stacking of the rigid conjugated part of the acceptor amphiphile[4, 40] into domains[39, 27]. The equal amount of conjugated region to side chains suggests that untextured aggregates form, confirmed by the TEM image (Figure 7.2). Figure 7.4 shows the (b) molar circular dichroism (CD) spectrum with the corresponding (a) absorption spectra. The inset shows the results of integrating over the CD signals from 430 to 500 nm, i.e. the acceptor absorption region. The strengthening of the CD signal at the acceptor absorption peak and the bisignate Cotton effect, positive at high energy and negative at low energy, suggest that the side chains introduce some helicity into the formation of acceptor aggregate domains[79, 20].

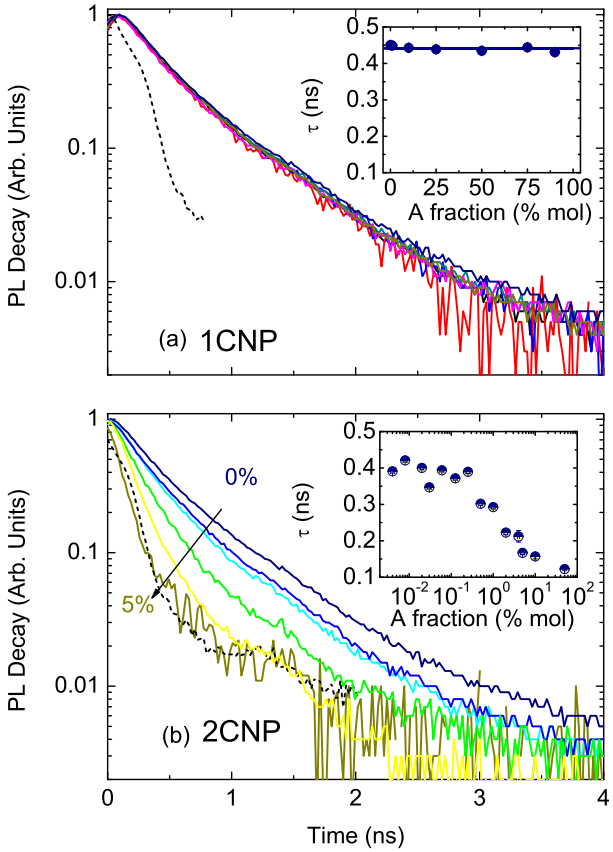

Figure 7.6: Normalised time-resolved photoluminescence decays of (a) single-component nanoparticles (1CNP) and (b) two-component nanoparticles (2CNP) at the donor emission peak wavelength (430 nm). The acceptor proportions in the 1CNP samples are 0, 1, 10, 25, 50, 75, and 90% and in the 2CNP samples are 0, 0.02, 0.12, 1, 2, and 5%. The dashed curves represent the instrument response function. The insets show donor lifetimes (τ) as a function of acceptor proportion, for all samples tested. The blue line in the inset in (a) is the average of the 1CNP lifetime values.

To examine further the dynamics of the CNPs, TCSPC experiments were conducted on the samples. Figure 7.6 shows the time-resolved donor PL decays, at an emission wavelength of 430 nm, for the 1CNPs and 2CNPs. Donor lifetimes were extracted from the graphs by fitting the peak to 1.0 ns past the peak with a monoexponential function ($y = Ae^{(-t/\tau)}$). In Figure 7.6(a), the decays overlap and the donor lifetimes, plotted as a function of acceptor fraction in the inset, are identical. The average of the lifetimes is 0.44 ns (blue line in inset), similar to lifetimes for polymer CNP systems and aggregates[216, 212, 98].

The 2CNP donor decays, shown in Figure 7.6(b), become faster as the acceptor percentage increases, due to acceptor quenching via energy transfer[46, 216, 79]. The 5% acceptor fraction decay overlaps with the instrument response function (IRF), dotted line in Figure 7.6(b). These effects are reflected by the extracted donor lifetimes, in the inset. The lifetimes decrease sharply at acceptor fractions above $\sim$0.1%, while above $\sim$5% the resolution limit is reached with a correspondingly slower rate of decrease. To extract Förster radii from the 2CNP PL decay data, this data was divided by the 0% acceptor decay, navy line in Figure 7.6(b), thereby separating the energy transfer transient from the donor natural lifetime. The resulting data was fitted with

$$K_{DA} = A\,exp\left(-7.42 C_A R_0^3 \sqrt{\frac{t}{\tau_D}}\right), \tag{7.4}$$

where K_{DA} is the donor emission intensity decay caused solely by energy transfer, A is a constant, and τ_D is the donor decay lifetime in the absence of acceptors (0.45 ns). (Refer to Equation 2.20 in Section 2.4.)

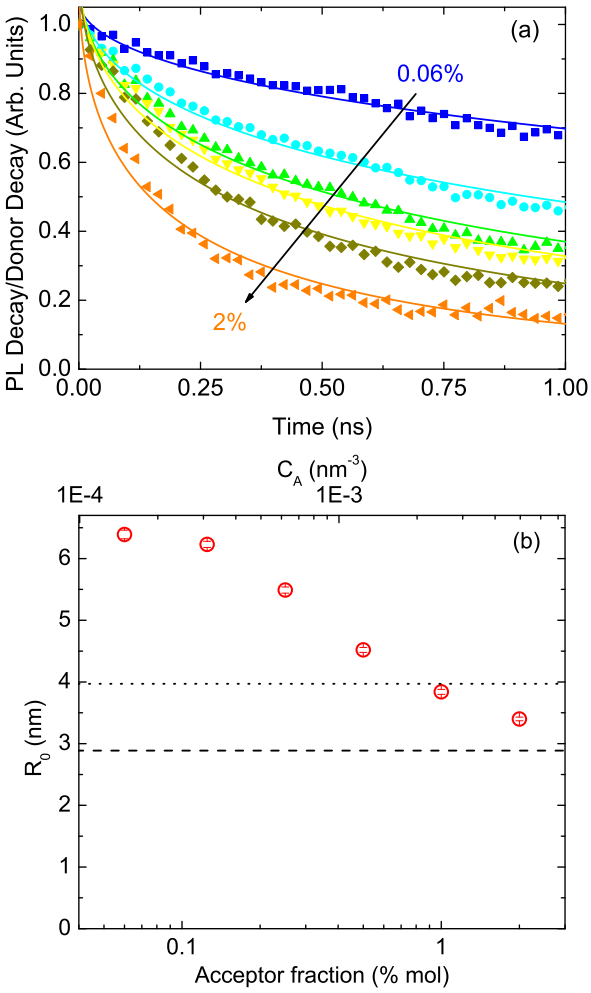

Figure 7.7: (a) Normalised energy transfer transients of the two-component nanoparticles (points) displayed with their fits (solid curves). The detection wavelength for the decays is at the donor photoluminescence emission peak wavelength (430 nm). The acceptor proportions in the samples are 0.06, 0.12, 0.25, 0.5, 1, and 2%. (b) The Förster radius (R_0) as a function of acceptor percentage and acceptor concentration. The dashed and dotted lines are the Förster radii calculated from spectral overlaps (see Eqn. 5.4) and extracted from fits to the time-integrated photoluminescence intensities at the donor and acceptor emission wavelengths (see Fig. 7.3), respectively.

The data with the corresponding fitting curves are shown in Figure 7.7(a). Plotting the PL decay data as a Kohlrausch-Williams-Watts representation, see Figure 7.8, it is clear the 3D (α=0.5) lines are the asymptotic limits to the data at long times. This confirms that Equation 7.4 incorporates the appropriate acceptor-donor ensemble dimensionality. The extracted Förster radii for different acceptor fractions are plotted in Figure 7.7(b), along with the calculated R_0 (dashed line, 2.9 nm) and the R_0 extracted from fits to the TIPL data (dotted line, 3.97 $\pm$ 0.03 nm). The Förster radii decrease as the acceptor fraction increases to 2%. Above 2%, the decays coincide with the IRF.

There are several reasons for the decreasing Förster radii. Upon introducing a very small amount of acceptors into a donor-only CNP, $<$0.01%, the donor decay lifetime decreases quite dramatically, from 0.45 to 0.40 ns, and then stays roughly constant until an acceptor fraction of 0.5% (inset of Figure 7.7(b)). Hence, the acceptors immediately disrupt the stacking of the donors leading to a lower donor lifetime than would be expected if donors were still fully packed[212]. In Chapter 6, the unstable nature of the donor stacking was observed upon annealing the donor CNPs at high temperatures. The donor lifetime increases from 0.56$\pm$0.01 to 0.66$\pm$0.01 ns, while the same treatment does not change the acceptor lifetime[105]. One reason for the packing disruption might be the different torsional angles[5] between the fluorene and benzothiadiazole molecules ($\sim$35°), and the fluorene and naphthalene molecules (71°). From equations 2.10 and 7.4, τ_D is proportional to R_0^6, so as the well-stacked 100% donor lifetime is higher than donor lifetimes in the frustrated stacks, an artificially high R_0 results. At 0.5%, when the effect of the donor lifetime is less important, the R_0 value is $\sim$4.5 nm which is

higher still than the calculated value. However, Förster theory neglects the effect of diffusion through homoenergy transfer between the donors. The homotransfer Förster radius is 1.5 nm; see Table 7.1.

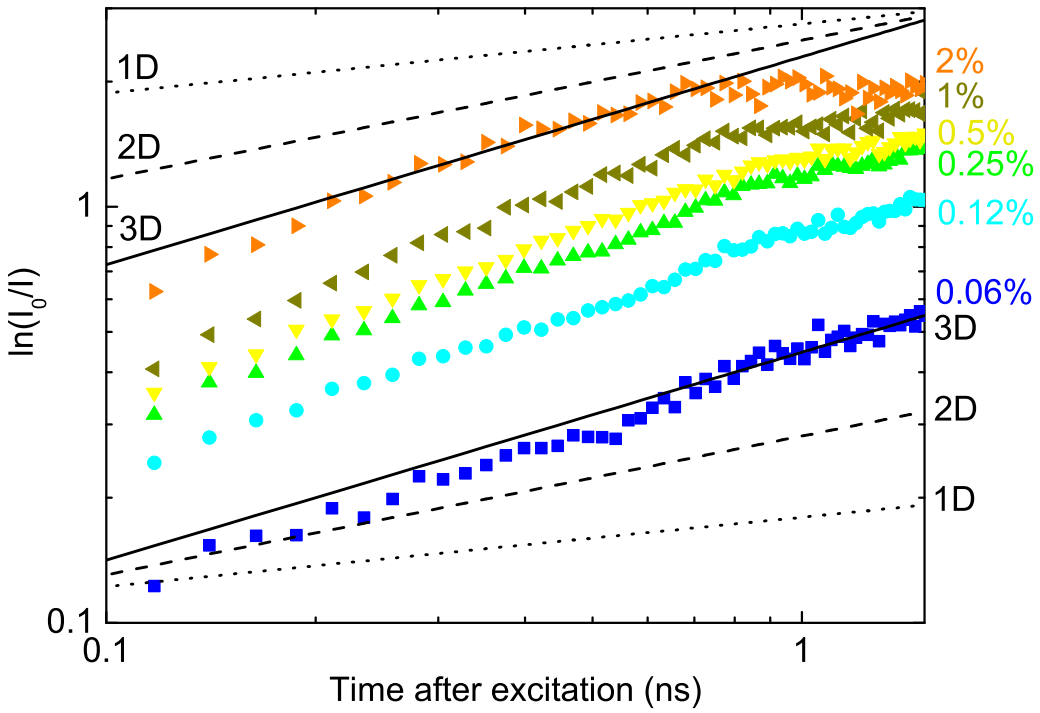

Figure 7.8: A Kohlrausch-Williams-Watts representation ($\log_{10}(ln(I_0/I))$ *vs.* $\log_{10}(t)$) of the excitation transfer decays of two-component nanoparticles, shown in Figure 7.7(a), for varying percentage of acceptor. $I(t)$ is the photoluminescence decay of the donor as a result of energy transfer *only*, I_0 is the initial intensity, and t_0 is a system-specific time constant related to R_0. The solid, dashed, and dotted lines represent a system dimensionality of 3, 2, and 1, respectively, i.e. slopes of $\frac{\Delta}{6}$ where Δ is the number of dimensions of the system.

Exciton diffusion increases the energy transfer rate by repopulating deexcited donors near acceptors, which are quenched quickly, with excitons[76, 52]. To correctly model the Förster en-

ergy transfer in other CNP systems with a Monte Carlo-type simulation, exciton diffusion length parameters of 8 ± 1 nm must be included[216]. Hence, the experimentally-extracted Förster radii, both from TIPL intensities and from PL decays, are larger than the calculated Förster radius. The final process that affects the Förster radii is the acceptors stacking into domains, which becomes significant as the acceptor fraction reaches 1% and above. The stacking limits the energy transfer because the acceptors are surrounded predominantly by other acceptors. Hence, the effective energy transfer surface area is decreased due to these large acceptor regions. This contributes to the decrease in the Förster radius of the last points in Figure 7.7(b).

7.4 Conclusion

For the flourene-based systems under investigation, TIPL intensity investigations proved there was no interparticle, and hence no 1CNP sample, energy transfer. However, in the 2CNP particles, highly efficient energy transfer was evident — a direct result of the close proximity of the molecules. The PL emission at acceptor wavelengths was indicative of aggregation through decreased and redshifted PL. The extracted stacked acceptor value as a function of acceptor fraction in the CNPs became significant at around 1% acceptor fraction. These results, in conjunction with the supporting CD results, confirmed that the acceptors π-π stacked along their conjugated core sections, enabled by their chiral fluorene side chains. Energy transfer was confirmed by the decreased donor lifetime as the acceptor fraction increased. The energy transfer transients were obtained as the quotient of the donor decays (with incorporated acceptor frac-

tions) by the pure donor decay. The Förster radii extracted from three sources were compared: PL intensities, PL decays ($\geq$0.06%), and donor / acceptor spectral overlap. The radii from the second source exceeded that of the third for all acceptor fractions, but was a decreasing function of the acceptor fraction rather than a constant. The large initial radii were artifacts of the disrupted donor stacks, thereby altering the donor lifetime. Efficient exciton diffusion amongst the donors widens the Förster radius also. Finally, acceptor stacking into domains at higher acceptor fractions decreases the energy transfer efficiency and, in turn, the Förster radius. The morphology of the molecules in the CNP system has a clear bearing on the energy transfer efficiency. When CNPs are used to track and image biomolecules, morphological effects cannot be taken lightly, as they determine the fluorescence intensities of the CNPs.

Chapter 8

Postscript

This dissertation has proved conclusively the credo *morphology matters*. The morphology of an assembled molecular structure controls the interactions between the molecules through their relative orientations and separation distances. This, in turn, affects the efficiency of energy transfer between donor and acceptor chromophores embedded in those molecules. Hence, energy transfer was harnessed to provide evidence of the types and strengths of the interactions present in the structures.

Two new organic structures were investigated. Firstly, in chapters 4 and 5, a supramolecular model organic wire was examined. This DNA-hybrid assembly was exciting because the energy transporting efficiency problems associated with intercalation of dyes was removed by changing to a dye incorporation method. The naphthalene-derivative donor molecules were hydrogen bonded directly to the thymine bases in the ssDNA strand. Energy transfer was observed to occur from the assembled donors to the end-appended cyanine dye through use of

time-integrated photoluminescence (TIPL) and time-correlated single photon counting (TCSPC) measurements. The energy transfer depended crucially on the temperature of the sample and the length of the thymine-base strand. Once the temperature rose above $\sim$25°C, the hydrogen bonding was disrupted, thus dissolving the donor assembly. The optimum thymine-base scaffold length at which to achieve an ordered and fully-assembled donor array was 30 thymine bases. For shorter scaffolds, the extra energy gained from donor cooperative interactions as they decorate the template is insufficient to stabilise the array. It was puzzling that the energy transfer rate should also decrease for scaffolds composed of more than 30 thymine bases. At these lengths, the donors fully decorate the thymine bases. To understand this complicated dependence on template length, the energy transfer dependence on the distances between the acceptor dye and donor chromophores was modelled. An emission intensity for each donor along the assembly was calculated which depended on the distance between the donor and the acceptor molecules, the radiative lifetime of the donors, and the Förster radius. The Förster radius incorporated the effects of donor-acceptor chromophore dipole orientation and spectral overlap. Including these effects, while disregarding template-dependent completeness of assembly, donor to donor exciton migration, and other multiple donor considerations, revealed that the energy transfer rate decreased sharply as the template length increased above 10 to 20 thymine bases.

It would be very interesting to be able to measure how many donors are on a particular DNA template composed of a certain number of thymines at a certain temperature. An investigation of the uniformity of the distribution of the donor array from one template to the next would yield compelling results, also. To image the individual structures, single molecule meth-

ods are required. These methods, which include single-molecule imaging and single-molecule nanomanipulation through the use of AFM-based[224, 10, 65] measurements for example, are widespread and have been applied to the study of molecular motors'[87] behaviour amongst other things. A less widely-used technique is the alternating laser excitation of single molecules (ALEX). A single molecule diffusing through a confocal volume labelled with donors and acceptors is excited by alternating green and red laser pulses to produce a photon burst[176]. The emitted photons are collected and separated into four separate signals depending on the laser excitation (D_{exc} or A_{exc}) and the emission detection (D_{em} or A_{em}) wavelengths[109]. The molecules are sorted according to their FRET efficiency and their stoichiometry (depends on presence of acceptor and/or donor species)[122]. The emission contributions from DNA strands with different donor-acceptor separations, down to a five base-pair difference, were extracted from a mixed DNA sample[177]. With this technology, the numbers and positions of donors on a ssDNA strand could be imaged directly and the variations between different strands in the same sample could be estimated. This would complement the ensemble fluorescence emission spectra and emission decays to yield a deeper understanding of the supramolecular DNA-hybrid structure.

Neglecting multiple effects that occur in real-life systems, e.g. donor array disorder and exciton migration, leads to an overestimated theoretical energy transfer rate at short template lengths; at long lengths; it underestimates it — see Chapter 5. Also, because the inter-donor distances are small, the point-dipole assumption has limited validity. Hence, an interesting further project would be to model the DNA assembly with a Monte Carlo simulation. Monte Carlo simulations have been used to investigate hopping and trapping of excitations in organic

systems[178, 209, 210]. A Monte Carlo simulation involves generating a molecule, randomly placing an excitation upon it, calculating probabilities for each process that the excitation could undergo (e.g. migration, energy transfer), choosing a process based on the probabilities, updating the system, and repeating the procedure[178, 89, 209]. A more accurate result would be achieved if the transition dipole moment contribution to the simulated excitonic coupling term (V_{AD}) was defined by the line-dipole approximation[18]. This would improve our understanding of the relative importance of more complicated transport effects in the DNA system and should reproduce the experimental energy transfer rates.

In chapters 6 and 7, another new organic structure was investigated. Amphiphilic molecules, with an embedded naphthalene (donor) or benzothiadiazole (acceptor) species, self-assembled into conjugated nanoparticles when injected into a large volume of polar solvent. Preliminary and stability investigations of the acceptor-only or donor-only particles reveal the presence of stacking interactions. The stacking interactions are specific to the molecular structure of the amphiphiles and so impart different stabilities and spectral signatures on the acceptor and donor nanoparticles. When the acceptor and donor amphiphiles form mixed nanoparticles, the energy transfer is very efficient. This is because of a very favourable spectral overlap and the close proximity of the chromophores. The nanoparticle dynamics were investigated through use of the Förster energy transfer model, which has been applied successfully to many conjugated polymer film systems. The Förster radius was extracted by calculating the donor-acceptor spectral overlap, by fitting to acceptor-fraction dependent time-integrated photoluminescence plots, and by fitting to acceptor-fraction dependent time-resolved photoluminescence decays. Surprisingly, the

Förster radius extracted from the photoluminescence decays varied for nanoparticles containing a different fraction of acceptor molecules. This uncommon result was explained by including the influence of stacking interactions and the different conformations of the acceptor and donor amphiphiles.

An intriguing experiment to try is to introduce these nanoparticles into live cells and test their fluorescence response. Other nanoparticles have been uptaken readily by cells and have shown good fluorescence signals[129]. Even more exciting would be to covalently bond, or otherwise embed, functional groups into these molecules such that they could target[81] and image specific cells in their nanoparticle state. Changing the structures of the molecules could provide further important insights into the role of morphology in these nanoparticles. The morphology effect of altering the ratio of hydrophobic to hydrophilic parts of the molecules could be examined by testing the stacking interactions in the nanoparticles. Literature suggests also that changing the size and chemical structure of the polymer coil-type end groups[199, 2] of the amphiphiles could enable the molecules to form micelles[14, 46] or vesicles upon fast injection into a polar solvent. It would be fascinating to assess how the energy transfer changes as a result of forming hollow nanoparticle vesicles.

Appendix A

List of publications:

- A Ruiz-Carretero, PGA Janssen, AL Stevens, M Surin, LM Herz, and APHJ Schenning. Directing energy transfer in discrete one-dimensional oligonucleotide-templated assemblies. *Chem. Commun.* , (2011), **47**, 884-886.
- AL Stevens, PGA Janssen, A Ruiz-Carretero, M Surin, APHJ Schenning, and LM Herz. Energy transfer in single-stranded DNA-templated stacks of naphthalene chromophores. *J. Phys. Chem. C*, (2011), **115**, 10550-10560.
- AL Stevens, A Kaeser, APHJ Schenning, and LM Herz. Morphology-dependent energy transfer dynamics in fluorene-based organic amphiphile nanoparticles. *In preparation*.
- A Kaeser, I Fischer, R Abbel, P Besenius, D Dasgupta, M Gillissen, G Portale, AL Stevens, LM Herz, and APHJ Schenning. Fluorescent nanoparticles based on self-assembled π-conjugated oligomers: The role of side chains on the dynamics within and between nanoparticles. *In preparation*.

Appendix B

Cartesian coordinates of the head and tail of the lowest transition dipole vector in naphthalene, shown in Figure 5.2, for the 40-base complex sample (NP-T40-Cy3.5).

Type	*HEAD: x*	*y*	*z*	*TAIL: x*	*y*	*z*
A†	-5.969000	-3.209000	134.511996	-9.754000	-7.666000	132.422997
D‡ **1**	11.700000	1.620000	131.106995	7.179000	2.916000	132.227997
D 2	12.566000	-4.092000	128.768005	8.720000	-1.148000	128.604996
D 3	7.738000	-9.420000	127.636002	6.260000	-4.931000	126.569000
D 4	2.773000	-12.246000	123.922997	3.668000	-7.513000	123.439003
D 5	-1.442000	-11.640000	122.038002	0.602000	-8.130000	119.388000
D 6	-11.162000	-6.010000	116.036003	-6.425000	-6.791000	115.422997
D 7	-12.446000	3.848000	116.144997	-9.216000	0.453000	114.927002
D 8	-8.616000	7.038000	114.094002	-6.970000	3.804000	110.876999
D 9	5.537000	14.147000	103.551003	2.817000	10.206000	104.218002
D 10	9.196000	7.999000	102.039001	4.493000	8.184000	100.930000

Type	*HEAD: x*	*y*	*z*	*TAIL: x*	*y*	*z*
D 11	11.985000	2.432000	100.758003	7.702000	4.177000	99.350998
D 12	13.988000	-3.668000	93.113998	10.079000	-2.176000	95.544998
D 13	8.416000	-8.501000	89.481003	7.073000	-4.188000	91.241997
D 14	-5.226000	-14.337000	88.411003	-2.969000	-10.101000	89.101997
D 15	-9.047000	-10.311000	85.977997	-4.772000	-8.117000	85.315002
D 16	-11.056000	-2.687000	82.045998	-6.474000	-4.100000	81.374001
D 17	-11.193000	1.415000	80.638000	-7.503000	-0.894000	78.508003
D 18	-6.985000	9.609000	68.223999	-6.251000	7.821000	72.653999
D 19	3.876000	14.590000	69.768997	1.393000	10.440000	70.092003
D 20	5.858000	10.865000	68.459000	2.546000	7.777000	66.725998
D 21	11.775000	3.637000	64.578003	7.010000	4.461000	64.292999
D 22	11.969000	-4.693000	61.456001	8.518000	-1.316000	61.766998
D 23	8.354000	-9.427000	59.305000	6.768000	-4.910000	58.567001
D 24	2.395000	-11.447000	57.505001	3.831000	-7.185000	55.7090002
D 25	-0.253000	-12.536000	55.018002	1.514000	-9.239000	51.943001
D 26	-10.333000	-5.420000	49.695000	-5.542000	-5.521000	48.9620021
D 27	-12.870000	3.267000	46.172001	-8.979000	0.383000	46.034000
D 28	-6.495000	8.359000	44.863998	-6.227000	4.211000	42.367001
D 29	6.331000	12.096000	34.778000	2.594000	9.290000	36.035999
D 30	10.582000	8.839000	33.200001	5.972000	7.478000	32.660000

Type	*HEAD: x*	*y*	*z*	*TAIL: x*	*y*	*z*
D 31	12.924000	1.936000	30.849001	8.154000	2.781000	31.038000
D 32	11.856000	-4.845000	29.275999	8.360000	-1.594000	28.466000
D 33	5.823000	-11.114000	22.686001	4.913000	-6.782000	24.636000
D 34	-0.303000	-13.620000	21.155001	1.199000	-9.196000	19.921000
D 35	-7.128000	-10.528000	18.670000	-2.937000	-8.118000	18.809000
D 36	-11.175000	-1.853000	13.691000	-6.621000	-3.284000	14.509000
D 37	-11.887000	6.164000	12.155000	-8.466000	2.992000	10.848000
D 38	-6.793000	11.801000	5.000000	-6.237000	7.607000	7.342000
D 39	1.044000	14.266000	3.427000	-1.224000	9.993000	3.621000
D 40	4.869000	11.684000	2.878000	1.797000	8.391000	1.078000

†: Cy3.5 acceptor dye transition dipole coordinates. ‡: Naphthalene donor transition dipole coordinates for each of 40 donor molecules attached to the DNA template.

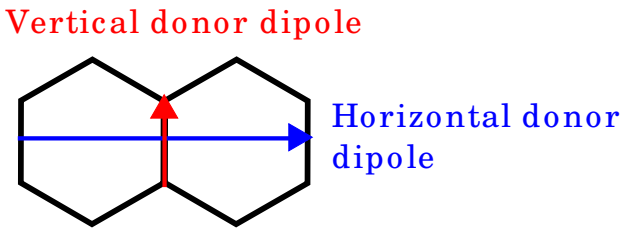

Figure 8.1: The electronic transition dipoles in naphthalene. The transition dipole with the lowest energy is the horizontal dipole. The “head” is the point of the arrow and the “tail” is the other end of the vector.

Bibliography

[1] Abbel, R., Grenier, C., Pouderoijen, M. J., Stouwdam, J. W., Leclère, P. E. L. G., Sijbesma, R. P., Meijer, E. W., and Schenning, A. P. H. J. White-light emitting hydrogen-bonded supramolecular copolymers based on π-conjugated oligomers. *J. Am. Chem. Soc. 131* (2009), 833–843.

[2] Abbel, R., Schenning, A. P. H. J., and Meijer, E. W. Molecular weight optimum in the mesoscopic order of chiral fluorene (co)polymer films. *Macromolecules 41* (2008), 7497–7504.

[3] Abbel, R., Schenning, A. P. H. J., and Meijer, E. W. Fluorene-based materials and their supramolecular properties. *J. Polym. Sci. Pol. Chem. 47* (2009), 4215–4233.

[4] Abbel, R., van der Weegen, R., Meijer, E. W., and Schenning, A. P. H. J. Multicolour self-assembled particles of fluorene-based bolaamphiphiles. *Chem. Commun. 0* (2009), 1697–1699.

[5] ABBEL, R., VAN DER WEEGEN, R., PISULA, W., SURIN, M., LECLÈRE, P., LAZZARONI, R., MEIJER, E. W., AND SCHENNING, A. P. H. J. Multicolour self-assembled fluorene co-oligomers: from molecules to the solid state via white-light-emitting organogels. *Chem.-Eur. J. 15* (2009), 9737–9746.

[6] ABBEL, R., WOFFS, M., BOVEE, R. A. A., VAN DONGEN, J. L. J., LOU, X., HENZE, O., FEAST, W. J., MEIJER, E. W., AND SCHENNING, A. P. H. J. Side-chain degradation of ultrapure π-conjugated oligomers: implications for organic electronics. *Adv. Mater. 21* (2009), 597–602.

[7] AJAYAGHOSH, A., VARGHESE, R., PRAVEEN, V. K., AND MAHESH, S. Evolution of nano- to microsized spherical assemblies of a short oligo(*p*-phenyleneethynylene) into superstructured organogels. *Angew. Chem.-Int. Edit. 45* (2006), 3261–3264.

[8] ALBERS, P., STARK, E., AND HUBER, G. Continuous-wave laser operation and quantum efficiency of titanium-doped sapphire. *J. Opt. Soc. Am. B 3* (1986), 134–139.

[9] ALLARD, S., FORSTER, M., SOUHARCE, B., THIEM, H., AND SCHERF, U. Organic semiconductors for solution-processable field-effect transistors (OFETs). *Angew. Chem. Int. Ed. 47* (2008), 4070–4098.

[10] ALLEN, S., RIGBY-SINGLETON, S. M., HARRIS, H., DAVIES, M. C., AND O'SHEA, P. Measuring and visualizing single molecular interactions in biology. *Biochem. Soc. Trans. 31* (2003), 1052–1057.

[11] ANDERSON, H. L. Building molecular wires from the colours of life: conjugated porphyrin oligomers. *Chem. Commun. 0* (1999), 2323–2330.

[12] ANTONY, M. J., AND JAYAKANNAN, M. Molecular template approach for evolution of conducting polymer nanostructures: tracing the role of morphology on conductivity and solid state ordering. *J. Phys. Chem. B 114* (2010), 1314–1324.

[13] APANASOVICH, V. V., AND NOVIKOV, E. G. Deconvolution method for fluorescence decays. *Opt. Commun. 78* (1990), 279–282.

[14] AYDIN, B. M., ACAR, M., ARIK, M., AND ONGANER, Y. The fluorescence resonance energy transfer between dye compounds in micellar media. *Dyes Pigment. 81* (2009), 156–160.

[15] BAUMANN, J., AND FAYER, M. D. Excitation transfer in disordered two-dimensional and anisotropic three-dimensional systems: effects of spatial geometry on time-resolved observables. *J. Chem. Phys. 85* (1986), 4087–4107.

[16] BECKER & HICKL GMBH. *The bh TCSPC Handbook*. Nahmitzer Damm 30, 12277 Berlin, Germany.

[17] BECKER, W. *Advanced time-correlated single photon counting techniques*. Springer-Verlag Berlin, 2005.

[18] BEENKEN, W. J. D., AND PULLERITS, T. Excitonic coupling in polythiophenes: comparison of different calculation methods. *J. Chem. Phys. 120* (2004), 2490.

[19] BEENKEN, W. J. D., AND PULLERITS, T. Spectroscopic units in conjugated polymers: A quantum chemically founded concept? *J. Phys. Chem. B 108* (2004), 6164–6169.

[20] BEHANNA, H. A., RAJANGAM, K., AND STUPP, S. I. Modulation of fluorescence through coassembly of molecules in organic nanostructures. *J. Am. Chem. Soc. 129* (2007), 321–327.

[21] BELJONNE, D., HENNEBICQ, E., DANIEL, C., HERZ, L. M., SILVA, C., SCHOLES, G. D., HOEBEN, F. J. M., JONKHEIJM, P., SCHENNING, A. P. H. J., MESKERS, S. C. J., PHILLIPS, R. T., FRIEND, R. H., AND MEIJER, E. W. Excitation migration along oligophenylenevinylene-based chiral stacks: Delocalization effects on transport dynamics. *J. Phys. Chem. B 109* (2005), 10594–10604.

[22] BELJONNE, D., POURTOIS, G., SILVA, C., HENNEBICQ, E., HERZ, L. M., FRIEND, R. H., SCHOLES, G. D., SETAYESH, S., MÜLLEN, K., AND BRÉDAS, J. L. Interchain vs. intrachain energy transfer in acceptor-capped conjugated polymers. *Proc. Natl. Acad. Sci. USA. 99* (2002), 10982–10987.

[23] BELJONNE, D., SHUAI, Z., POURTOIS, G., AND BREDAS, J. L. Spin-orbit coupling and intersystem crossing in conjugated polymers: a configuration interaction description. *J. Phys. Chem. A 105* (2001), 3899–3907.

[24] BERBERAN-SANTOS, M. N., BODUNOV, E. N., AND VALEUR, B. Mathematical functions for the analysis of luminescence decays with underlying distributions 1. Kohlrausch decay function (stretched exponential). *Chem. Phys. 315* (2005), 171–182.

[25] BERDEN, G., MEERTS, W. L., PLUSQUELLIC, D. F., FUJITA, I., AND PRATT, D. W. High resolution electronic spectroscopy of 1-aminonaphthalene: s_0 and s_1 geometries and $s_1 leftarrows_0$ transition moment orientations. *J. Chem. Phys. 104* (1996), 3935–3946.

[26] BERLMAN, I. B. *Handbook of fluorescence spectra of aromatic molecules*. Academic Press, 1965.

[27] BHONGALE, C. J., AND HSU, C. S. Emission enhancement by formation of aggregates in hybrid chromophoric surfactant amphiphile/silica nanocomposites. *Angew. Chem.-Int. Edit. 45* (2006), 1404–1408.

[28] BIRKS, J. B. *Photophysics of aromatic molecules*. Wiley-interscience, 1970.

[29] BLUMEN, A., AND MANZ, J. On the concentration and time dependence of the energy transfer to randomly distributed acceptors. *J. Chem. Phys. 71* (1979), 4694–4702.

[30] BULAKOV, D. V., AND SALETSKIĬ, A. M. Processes of electronic excitation energy transfer between luminescent dye molecules in microheterogeneous systems based on polymer micellar solutions. *Opt. Spectrosc. 104* (2008), 374–377.

[31] BURROUGHES, J. H., BRADLEY, D. D. C., BROWN, A. R., MARKS, R. N., MACKAY, K., FRIEND, R. H., BURNS, P. L., AND HOLMES, A. B. Light-emitting-diodes based on conjugated polymers. *Nature 347* (1990), 539–541.

[32] CHAN, Y. H., WU, C. F., YE, F. M., JIN, Y. H., SMITH, P. B., AND CHIU, D. T. Development of ultrabright semiconducting polymer dots for ratiometric pH sensing. *Anal. Chem. 83* (2011), 1448–1455.

[33] CHANG, M. H., FRAMPTON, M. J., ANDERSON, H. L., AND HERZ, L. M. Photoexcitation dynamics in thin films of insulated molecular wires. *Appl. Phys. Lett. 89* (2006), 232110.

[34] CHANG, M. H., HOEBEN, F. J. M., JONKHEIJM, P., SCHENNING, A. P. H. J., MEIJER, E. W., SILVA, C., AND HERZ, L. M. Influence of mesoscopic ordering on the photoexcitation transfer dynamics in supramolecular assemblies of oligo-*p*-phenylenevinylene. *Chem. Phys. Lett. 418* (2006), 196–201.

[35] CHEN, Q., FENG, Y., ZHANG, D. Q., ZHANG, G. X., FAN, Q. H., SUN, S. N., AND ZHU, D. B. Light-triggered self-assembly of a spiropyran-functionalized dendron into nano-/micrometer-sized particles and photoresponsive organogel with switchable fluorescence. *Adv. Funct. Mater. 20* (2010), 36–42.

[36] CHEN, Q., LIU, N., YING, L., YANG, W., WU, H., XU, W., AND CAO, Y. Novel white-light-emitting polyfluorenes with benzothiadiazole and Ir complex on the backbone. *Polymer 50* (2009), 1430–1437.

[37] CHEN, R. F., ZHENG, C., FAN, Q. L., AND HUANG, W. Structural, electronic, and optical properties of 9-heterofluorenes: a quantum chemical study. *J. Comput. Chem. 28* (2007), 2091–2101.

[38] CHOWDHURY, A., WACHSMANN-HOGIU, S., BANGAL, P. R., RAHEEM, I., AND PETEANU, L. A. Characterization of chiral H and J aggregates of cyanine dyes formed

by DNA templating using stark and fluorescence spectroscopies. *J. Phys. Chem. B 105* (2001), 12196–12201.

[39] CLARK, J., SILVA, C., FRIEND, R. H., AND SPANO, F. C. Role of intermolecular coupling in the photophysics of disordered organic semiconductors: aggregate emission in regioregular polythiophene. *Phys. Rev. Lett. 98* (2007), 206406.

[40] COLBY, K. A., BURDETT, J. J., FRISBEE, R. F., ZHU, L., DILLON, R. J., AND BARDEEN, C. J. Electronic energy migration on different time scales: concentration dependence of the time-resolved anisotropy and fluorescence quenching of Lumogen Red in poly(methyl methacrylate). *J. Phys. Chem. A 114* (2010), 3471–3482.

[41] COOPER, V. R., THONHAUSER, T., PUZDER, A., SCHRÖDER, E., LUNDQVIST, B. I., AND LANGRETH, D. C. Stacking interactions and the twist of DNA. *J. Am. Chem. Soc. 130* (2008), 1304–1308.

[42] CORNIL, J., BELJONNE, D., CALBERT, J. P., AND BRÉDAS, J. L. Interchain interactions in organic π-conjugated materials: impact on electronic structure, optical response, and charge transport. *Adv. Mater. 13* (2001), 1053–1067.

[43] CORNIL, J., DOS SANTOS, D. A., CRISPIN, X., SILBEY, R., AND BRÉDAS, J. L. Influence of interchain interactions on the absorption and luminescence of conjugated oligomers and polymers: A quantum-chemical characterization. *J. Am. Chem. Soc. 120* (1998), 1289–1299.

[44] CRAIG, D. P., HOLLAS, J. M., REDIES, M. F., AND WAIT, S. C. Analysis of the naphthalene vapour absorption bands at 3200. 1. Naphthalene h-8. *Philos. Trans. R. Soc. Lond. 253* (1961), 543.

[45] DANIEL, C., HERZ, L. M., BELJONNE, D., HOEBEN, F. J. M., JONKHEIJM, P., SCHENNING, A. P. H. J., MEIJER, E. W., PHILLIPS, R. T., AND SILVA, C. Resonance energy transfer dynamics in hydrogen-bonded oligo p-phenylenevinylene nanostructures. *Synth. Met. 147* (2004), 29–35.

[46] DE, S., AND GIRIGOSWAMI, A. Fluorescence resonance energy transfer - a spectroscopic probe for organized surfactant media. *J. Colloid Interface Sci. 271* (2004), 485–495.

[47] DE ARAÚJO, M. A. C., SILVA, R., DE LIMA, E., PEREIRA, D. P., AND DE OLIVEIRA, P. C. Measurement of Gaussian laser beam radius using the knife-edge technique: improvement on data analysis. *Appl. Optics 48* (2009), 393–396.

[48] DE CUENDIAS, A., IBARBOURE, E., LECOMMANDOUX, S., CLOUTET, E., AND CRAMAIL, H. Synthesis and self-assembly in water of coil-rod-coil amphiphilic block copolymers with central π-conjugated sequence. *J. Polym. Sci. Pol. Chem. 46* (2008), 4602–4616.

[49] DEMTRÖDER, W. *Laser Spectroscopy: Basic Concepts and Instrumentation*. Springer, 2003.

[50] DEXTER, D. L. A theory of sensitized luminescence in solids. *J. Chem. Phys. 21* (1953), 836–850.

[51] DIETZ, H., DOUGLAS, S. M., AND SHIH, W. M. Folding DNA into twisted and curved nanoscale shapes. *Science 325* (2009), 725–730.

[52] EBBINGHAUS, S., KIM, S. J., HEYDEN, M., YU, X., HEUGEN, U., GRUEBELE, M., LEITNER, D. M., AND HAVENITH, M. An extended dynamical hydration shell around proteins. *Proc. Natl. Acad. Sci. U. S. A. 104* (2007), 20749–20752.

[53] EDELSTEIN, D. C., WACHMAN, E. S., CHENG, L. K., BOSENBERG, W. R., AND TANG, C. L. Femtosecond ultraviolet pulse generation in β-BaB_2O_4. *Appl. Phys. Lett. 52* (1988), 2211–2213.

[54] EKLUND, H., ROOS, A., AND ENG, S. T. Rotation of laser beam polarization in acousto-optic devices. *Opt. Quantum Electron. 7* (1975), 73–79.

[55] ELLIOTT, S. *The physics and chemistry of solids*. Wiley, 1998.

[56] FORK, R. L., MARTINEZ, O. E., AND GORDON, J. P. Negative dispersion using pairs of prisms. *Opt. Lett. 9* (1984), 150–152.

[57] FORREST, S. R. The path to ubiquitous and low-cost organic electronic appliances on plastic. *Nature 428* (2004), 911–918.

[58] FÖRSTER, T. H. Zwischenmolekulare energiewanderung und fluoreszenz. *Ann. Physik 437* (1948), 55–75.

[59] FÖRSTER, T. H. 10th Spiers Memorial Lecture. Transfer mechanisms of electronic excitation. *Discuss. Faraday Soc. 27* (1959), 7–17.

[60] FOX, M. *Optical Properties of Solids*. Oxford University Press, 2001.

[61] FRENCH, P. M. W. Ultrafast solid-state lasers. *Contemp. Phys. 37* (1996), 283.

[62] GEORGE, S. J., BOVEE, R., SCHENNING, A. P. H. J., AND MEIJER, E. W. Photodimerization processes in self-assembled chiral oligo(p-phenylenevinylene) bolaamphiphiles. *Chem.-Asian J. 4* (2009), 910–917.

[63] GEUSIC, J. E., MARCOS, H. M., AND VAN UITERT, L. G. Laser oscillations in Nd-doped yttrium aluminium, yttrium gallium and gadolinium garnets. *Appl. Phys. Lett. 4* (1964), 182–184.

[64] GHOSH, S., MANDAL, U., ADHIKARI, A., DEY, S., AND BHATTACHARYYA, K. Study of organized and biological systems using an ultrafast laser. *Int. Rev. Phys. Chem. 26* (2007), 421–448.

[65] GREENLEAF, W. J., WOODSIDE, M. T., AND BLOCK, S. M. High-resolution, single-molecule measurements of biomolecular motion. *Annu. Rev. Biophys. Biomolec. Struct. 36* (2007), 171–190.

[66] HAAS, S., TAKAHASHI, Y., TAKIMIYA, K., AND HASEGAWA, T. High-performance dinaphtho-thieno-thiophene single crystal field-effect transistors. *Appl. Phys. Lett. 95* (2009), 22111–22113.

[67] HAINS, A. W., LIANG, Z., WOODHOUSE, M. A., AND GREGG, B. A. Molecular semiconductors in organic photovoltaic cells. *Chem. Rev. 110* (2010), 66896735.

[68] HÄNER, R., SAMAIN, F., AND MALINOVSKII, V. L. DNA-assisted self-assembly of pyrene foldamers. *Chem. Eur. J. 15* (2009), 5701–5708.

[69] HANNAH, K. C., AND ARMITAGE, B. A. DNA-templated assembly of helical cyanine dye aggregates: a supramolecular chain polymerization. *Accounts Chem. Res. 37* (2004), 845–853.

[70] HANNESTAD, J. K., SANDIN, P., AND ALBINSSON, B. Self-assembled DNA photonic wire for long-range energy transfer. *J. Am. Chem. Soc. 130* (2008), 15889–15895.

[71] HARVEY, B. J., AND LEVITUS, M. Nucleobase-specific enhancement of Cy3 fluorescence. *J. Fluoresc. 19* (2009), 443–448.

[72] HARVEY, B. J., PEREZ, C., AND LEVITUS, M. DNA sequence-dependent enhancement of Cy3 fluorescence. *Photochem. Photobiol. Sci. 8* (2009), 1105–1110.

[73] HASHIMOTO, T., NAKANO, H., AND HIRAO, K. Theoretical study of the valence $\pi \rightarrow \pi^*$ excited states of polyacenes: benzene and naphthalene. *J. Chem. Phys. 104* (1996), 6244–6258.

[74] HERZ, L. M. *Aggreagation effects in conjugated polymer films studied by time-resolved photoluminescence spectroscopy*. PhD thesis, University of Cambridge, November 2001.

[75] HERZ, L. M., SILVA, C., FRIEND, R. H., PHILLIPS, R. T., SETAYESH, S., BECKER, S., MARSITSKY, D., AND MÜLLEN, K. Effects of aggregation on the excitation transfer in perylene-end-capped polyindenofluorene studied by time-resolved photoluminescence spectroscopy. *Phys. Rev. B 64* (2001), 195203.

[76] HERZ, L. M., SILVA, C., GRIMSDALE, A. C., MÜLLEN, K., AND PHILLIPS, R. T. Time-dependent energy transfer rates in a conjugated polymer guest-host system. *Phys. Rev. B 70* (2004), 165207.

[77] HIROMI MINEMAWARI, TOSHIKAZU YAMADA, H. M. J. T. S. H. R. C. R. K. . T. H. Inkjet printing of single-crystal films. *Nature 475* (2011), 364–367.

[78] HIRST, A. R., ESCUDER, B., MIRAVET, J. F., AND SMITH, D. K. High-tech applications of self-assembling supramolecular nanostructured gel-phase materials: from regenerative medicine to electronic devices. *Angew. Chem.-Int. Edit. 47* (2008), 8002–8018.

[79] HOEBEN, F. J. M., SHKLYAREVSKIY, I. O., POUDEROIJEN, M. J., ENGELKAMP, H., SCHENNING, A. P. H. J., CHRISTIANEN, P. C. M., MAAN, J. C., AND MEIJER, E. W. Direct visualization of efficient energy transfer in single oligo(*p*-phenylene vinylene) vesicles. *Angew. Chem.-Int. Edit. 45* (2006), 1232–1236.

[80] HOPPE, H., AND SARICIFTCI, N. S. Organic solar cells: an overview. *J. Mater. Res. 19* (2004), 1924–1945.

[81] HOWES, P., GREEN, M., BOWERS, A., PARKER, D., VARMA, G., KALLUMADIL, M., HUGHES, M., WARLEY, A., BRAIN, A., AND BOTNAR, R. Magnetic conjugated polymer nanoparticles as bimodal imaging agents. *J. Am. Chem. Soc. 132* (2010), 9833–9842.

[82] HSU, C. P., YOU, Z. Q., AND CHEN, H. C. H. Characterization of the short-range couplings in excitation energy transfer. *J. Phys. Chem. C 112* (2008), 1204–1212.

[83] HUEBNER, C. F., ROEDER, R. D., AND FOULGER, S. H. Nanoparticle electroluminescence: controlling emission color through Förster resonance energy transfer in hybrid particles. *Adv. Funct. Mater. 19* (2009), 3604–3609.

[84] HUMPHREY, W., DALKE, A., AND SCHULTEN, K. VMD – Visual Molecular Dynamics. *Journal of Molecular Graphics 14* (1996), 33–38.

[85] IQBAL, A., ARSLAN, S., OKUMUS, B., WILSON, T. J., GIRAUD, G., NORMAN, D. G., HA, T., AND LILLEY, D. M. J. Orientation dependence in fluorescent energy transfer between Cy3 and Cy5 terminally attached to double-stranded nuclelic acids. *Proc. Natl. Acad. Sci. USA. 105* (2008), 11176–11181.

[86] IQBAL, A., WANG, L., THOMPSON, K. C., LILLEY, D. M. J., AND NORMAN, D. G. The structure of Cyanine 5 terminally attached to double-stranded DNA: implications for FRET studies. *Biochemistry 47* (2008), 7857–7862.

[87] ISHIJIMA, A., AND YANAGIDA, T. Single molecule nanobioscience. *Trends Biochem.Sci. 26* (2001), 438–444.

[88] ISHOW, E., BROSSEAU, A., CLAVIER, G., NAKATANI, K., TAUC, P., FIORINI-DEBUISSCHERT, C., NEVEU, S., SANDRE, O., AND LÉAUSTIC, A. Multicolor emission of small molecule-based amorphous thin films and nanoparticles with a single excitation wavelength. *Chem. Mat. 20* (2008), 6597–6599.

[89] ISRAELACHVILI, J. N. *Intermolecular and Surface Forces*. Academic Press, 1985.

[90] IWAURA, R., HOEBEN, F. J. M., MASUDA, M., SCHENNING, A. P. H. J., MEIJER, E. W., AND SHIMIZU, T. Molecular-level helical stack of a nucleotide-appended oligo(*p*-phenylenevinylene) directed by supramolecular self-assembly with a complementary oligonucleotide as a template. *J. Am. Chem. Soc. 128* (2006), 13298–13304.

[91] IWAURA, R., YOSHIDA, K., MASUDA, M., OHNISHI-KAMEYAMA, M., YOSHIDA, M., AND SHIMIZU, T. Oligonucleotide-templated self-assembly of nucleotide bolaamphiphiles: DNA-like nanofibers edged by a double-helical arrangement of A-T base pairs. *Angew. Chem. Int. Edit. 42* (2003), 1009–1012.

[92] JANSSEN, P. G. A. *DNA templated self-assembly*. PhD thesis, Eindhoven University of Technology, 2009.

[93] JANSSEN, P. G. A., BRANKAERT, N. J. M., VILA, X., AND SCHENNING, A. P. H. J. ssDNA templated assembly of oligonucleotides and bivalent naphthalene guests. *Soft Matter 6* (2010), 1494–1502.

[94] JANSSEN, P. G. A., JABBARI-FAROUJI, S., SURIN, M., VILA, X., GIELEN, J. C., DE GREEF, T. F. A., VOS, M. R. J., BOMANS, P. H. H., SOMMERDIJK, N. A. J. M., CHRISTIANEN, P. C. M., LECLÈRE, P., LAZZARONI, R., VAN DER SCHOOT, P., MEIJER, E. W., AND SCHENNING, A. P. H. J. Insights into templated supramolecular polymerization: binding of naphthalene derivatives to ssDNA templates of different lengths. *J. Am. Chem. Soc. 131* (2009), 1222–1231.

[95] JANSSEN, P. G. A., RUIZ-CARRETERO, A., GONZÁLEZ-RODRÍGUEZ, D., MEIJER, E. W., AND SCHENNING, A. P. H. J. PH-switchable helicity of DNA-templated assemblies. *Angew. Chem. Int. Edit. 48* (2009), 8103–8106.

[96] JANSSEN, P. G. A., VAN DONGEN, J. L. J., MEIJER, E. W., AND SCHENNING, A. P. H. J. Electrospray-ionization mass spectrometry for screening the specificity and stability of single-stranded-DNA templated self-assemblies. *Chem. Eur. J. 15* (2009), 352–360.

[97] JANSSEN, P. G. A., VANDENBERGH, J., VAN DONGEN, J. L. J., MEIJER, E. W., AND SCHENNING, A. P. H. J. ssDNA templated self-assembly of chromophores. *J. Am. Chem. Soc. 129* (2007), 6078–6079.

[98] JANSSON, E., JHA, P. C., AND ÅGREN, H. Chain length dependence of singlet and triplet excited states of oligofluorenes: a density functional study. *Chem. Phys. 336* (2007), 91–98.

[99] JENEKHE, S. A., AND OSAHENI, J. A. Excimers and exciplexes of conjugated polymers. *Science 265* (1994), 765–768.

[100] JOHANSSON, M. K., AND COOK, R. M. Intramolecular dimers: a new design strategy for fluorescence-quenched probes. *Chem. Eur. J. 9* (2003), 3466–3471.

[101] JOHANSSON, M. K., FIDDER, H., DICK, D., AND COOK, R. M. Intramolecular dimers: a new strategy to fluorescence quenching in dual-labeled oligonucleotide probes. *J. Am. Chem. Soc. 124* (2002), 6950–6956.

[102] JONES, R. A. L. *Soft Condensed Matter*. Oxford University Press, 2002.

[103] JURCHESCU, O. D., BAAS, J., AND PALSTRA, T. T. M. Effect of impurities on the mobility of single crystal pentacene. *Appl. Phys. Lett. 84* (2004), 3061–3063.

[104] JURCHESCU, O. D., POPINCIUC, M., VAN WEES, B. J., AND PALSTRA, T. T. M. Interface-controlled, high-mobility organic transistors. *Adv. Mater. 19* (2007), 688–692.

[105] KAESER, A., FISCHER, I., ABBEL, R., BESENIUS, P., DASGUPTA, D., GILLISSEN, M., PORTALE, G., STEVENS, A., HERZ, L., AND SCHENNING, A. P. H. J. Fluorescent nanoparticles based on self-assembled π-conjugated oligomers: the role of side chains on the dynamics within and between nanoparticles. In Preparation.

[106] KAESER, A., AND SCHENNING, A. P. H. J. Fluorescent nanoparticles based on self-assembled *pi*-conjugated systems. *Adv. Mater. 22* (2010), 2985–2997.

[107] KAFKA, J. D., WATTS, M. L., AND PIETERSE, J. J. Picosecond and femtosecond pulse generation in a regeneratively mode-locked Ti:Sapphire laser. *IEEE J. Quantum Electron. 28* (1992), 2151–2162.

[108] KAFKA, J. D., WATTS, M. L., AND PIETERSE, J. W. J. Picosecond and femtosecond pulse generation in a regeneratively mode-locked ti-sapphire laser. *IEEE J. Quantum Electron. 28* (1992), 2151.

[109] KAPANIDIS, A. N., LEE, N. K., LAURENCE, T. A., DOOSE, S., MARGEAT, E., AND WEISS, S. Fluorescence-aided molecule sorting: analysis of structure and interactions by alternating-laser excitation of single molecules. *Proc. Natl. Acad. Sci. U. S. A. 101* (2004), 8936–8941.

[110] KASHA, M. Energy transfer mechanisms and the molecular exciton model for molecular aggregates. *Radiat. Res. 20* (1963), 55.

[111] KASHA, M., RAWLS, H. R., AND ASHRAF EL BAYOUMI, M. The exciton model in molecular spectroscopy. *Pure Appl. Chem. 11* (1965), 371–392.

[112] KAZZAZ, A. A., AND MUNRO, I. H. Naphthalene excimer emission. *Proc. Phys. Soc. 87* (1966), 329–330.

[113] KELLEY, T. W., BAUDE, P. F., GERLACH, C., ENDER, D. E., MUYRES, D., HAASE, M. A., VOGEL, D. E., AND THEISS, S. D. Recent progress in organic electronics: Materials, devices, and processes. *Chem. Mater. 16* (2004), 4413–4422.

[114] KEPLER, R. C. P. . R. G. Energy transfer in doped organic crystals. *Mol. Cryst. Liq. Cryst. 11* (1970), 349–360.

[115] KERSTING, R., LEMMER, U., MAHRT, R. F., LEO, K., KURZ, H., BÄSSLER, H., AND GÖBEL, E. O. Femtosecond energy relaxation in π-conjugated polymers. *Phys. Rev. Lett. 70* (1993), 3820–3823.

[116] KIPPELEN, B., AND BRÉDAS, J. Organic photovoltaics. *Energy Environ. Sci. 2* (2009), 241332.

[117] KLEVENS, H. B., AND PLATT, J. R. Spectral resemblances of cata-condensed hydrocarbons. *J. Chem. Phys. 17* (1949), 470–481.

[118] KOLBER, Z. S., AND BARKLEY, M. D. Comparison of approaches to the instrumental response function in fluorescence decay measurements. *Anal. Biochem. 152* (1986), 6–21.

[119] LANGE, U., ROZNYATOVSKAYA, N. V., AND MIRSKY, V. M. Conducting polymers in chemical sensors and arrays. *Anal. Chim. Acta 614* (2008), 1–26.

[120] LANGHALS, H., ESTERBAUER, A. J., WALTER, A., RIEDLE, E., AND PUGLIESI, I. Förster resonant energy transfer in orthogonally arranged chromophores. *J. Am. Chem. Soc. 132* (2010), 16777–16782.

[121] LAZARIDES, T., SYKES, D., FAULKNER, S., BARBIERI, A., AND WARD, M. D. On the mechanism of d-f energy transfer in Ru^{II}/L^{III} and Os^{II}/L^{III} dyads: Dexter-type energy transfer over a distance of 20 å. *Chem.-Eur. J. 14* (2008), 9389–9399.

[122] LEE, N. K., KAPANIDIS, A. N., WANG, Y., MICHALET, X., MUKHOPADHYAY, J., EBRIGHT, R. H., AND WEISS, S. Accurate FRET measurements within single diffusing biomolecules using alternating-laser excitation. *Biophys. J. 88* (2005), 2939–2953.

[123] LEHN, J. M., MASCAL, M., DECIAN, A., AND FISCHER, J. Molecular recognition directed self-assembly of ordered supramolecular strands by cocrystallization of complementary molecular-components. *J. Chem. Soc. Chem. Commun.* (1990), 479–481.

[124] LEHN, J. M., AND RIGAULT, A. Helicates: tetra- and pentanuclear double helix complexes of Cu^{I} and poly(bipyridine) strands. *Angew. Chem. Int. Edit. Engl. 27* (1988), 1095–1097.

[125] LEHN, J. M., RIGAULT, A., SIEGEL, J., HARROWFIELD, J., CHEVRIER, B., AND MORAS, D. Spontaneous assembly of double-stranded helicates from oligobipyridine ligands and copper(I) cations: structure of an inorganic double helix. *Proc. Natl. Acad. Sci. USA. 84* (1987), 2565–2569.

[126] LEMMER, U., HEUN, S., MAHRT, R. F., SCHERF, U., HOPMEIER, M., SIEGNER, U., GÖBEL, E. O., MÜLLEN, K., AND BÄSSLER, H. Aggregate fluorescence in conjugated polymers. *Chem. Phys. Lett. 240* (1995), 373–378.

[127] LEVITUS, M., NEGRI, R. M., AND ARAMENDÍA, P. F. Rotational relaxation of carbocyanines. Comparative study with the isomerization dynamics. *J. Phys. Chem. 99* (1995), 14231–14239.

[128] LEWIS, F. D., ZHANG, L. G., AND ZUO, X. B. Orientation control of fluorescence resonance energy transfer using DNA as a helical scaffold. *J. Am. Chem. Soc. 127* (2005), 10002–10003.

[129] LI, K., PAN, J., FENG, S. S., WU, A. W., PU, K. Y., LIU, Y. T., AND LIU, B. Generic strategy of preparing fluorescent conjugated-polymer-loaded poly(DL-lactide-*co*-glycolide) nanoparticles for targeted cell imaging. *Adv. Funct. Mater. 19* (2009), 3535–3542.

[130] LIN, H. C., SUNG, H. H., TSAI, C. M., AND LI, K. C. Synthesis and characterization of alternating fluorene-based copolymers containing diaryl- and non-substituted bithiophene units. *Polymer 46* (2005), 9810–9820.

[131] LINDIG, B. A., AND RODGERS, M. A. J. Molecular excited states in micellar systems. *Photochem. Photobiol. 31* (1980), 617–622.

[132] LIU, X. Z., ZHU, R., ZHANG, Y., LIU, B., AND RAMAKRISHNA, S. Anionic benzothiadiazole containing polyfluorene and oligofluorene as organic sensitizers for dye-sensitized solar cells. *Chem. Commun. 0* (2008), 3789–3791.

[133] LUDE, D. R. *CRC Handbook of Chemistry and Physics*. CRC PRESS, 2001.

[134] LUNZ, M., BRADLEY, A. L., CHEN, W. Y., AND GUN'KO, Y. K. Two-dimensional Förster resonant energy transfer in a mixed quantum dot monolayer: experiment and theory. *J. Phys. Chem. C 113* (2009), 3084–3088.

[135] LV, W., CHEN, X. D., AUMILER, D., AND XIA, A. D. Single molecule fluorescence fluctuations of the cyanine dyes linked covalently to DNA. *Sci. China Ser. B: Chem. 52* (2009), 1148–1153.

[136] MAKSIMOV, M. Z., AND ROZMAN, I. M. On the energy transfer in rigid solutions. *Opt. Spectrosc. 12* (1961), 337–338.

[137] MALIWAL, B. P., KUŚBA, J., AND LAKOWICZ, J. R. Fluorescence energy transfer in one dimension: frequency-domain fluorescence study of DNA-fluorophore complexes. *Biopolymers 35* (1995), 245–255.

[138] MALLICK, A., PURKAYASTHA, P., AND CHATTOPADHYAY, N. Photoprocesses of excited molecules in confined liquid environments: an overview. *J. Photochem. Photobiol. C-Photochem. Rev. 8* (2007), 109–127.

[139] MARTÍ, A. A., JOCKUSCH, S., LI, Z. M., JU, J. Y., AND TURRO, N. J. Molecular beacons with intrinsically fluorescent nucleotides. *Nucleic Acids Res. 34* (2006), e50.

[140] MAYER-ENTHART, E., WAGNER, C., BARBARIC, J., AND WAGENKNECHT, H. A. Helical self-assembled chromophore clusters based on DNA-like architecture. *Tetrahedron 63* (2007), 3434–3439.

[141] McClure, D. S. Excited states of the naphthalene molecule .1. Symmetry properties of the 1st 2 excited singlet states. *J. Chem. Phys. 22* (1954), 1668–1675.

[142] McNaught, A. D., and Wilkinson, A. *IUPAC Compendium of Chemical Terminology*. 1997. On-line corrected version created by M Nic, J Jirat, and B Kosata.

[143] Moulton, P. F. Spectroscopic and laser characteristics of Ti:Al_2O_3. *J. Opt. Soc. Am. B 3* (1986), 125–133.

[144] Nakamura, M., Ohtoshi, Y., and Yamana, K. Helical pyrene-array along the outside of duplex RNA. *Chem. Commun.* (2005), 5163–5165.

[145] Nakayama, K., Hirose, Y., Soeda, J., Yoshizumi, M., Uemura, T., Uno, M., Li, W., Kang, M. J., Yamagishi, M., Okada, Y., Miyazaki, E., Nakazawa, Y., Nakao, A., Takimiya, K., and Takeya, J. Patternable solution-crystallized organic transistors with high charge carrier mobility. *Adv. Mater. 23* (2011), 1626–1629.

[146] Norman, D. G., Grainger, R. J., Uhrín, D., and Lilley, D. M. J. Location of Cyanine-3 on double-stranded DNA: importance for fluorescence resonance energy transfer studies. *Biochemistry 39* (2000), 6317–6324.

[147] O'Connor, D. V., Ware, W. R., and Andre, J. C. Deconvolution of fluorescence decay curves. A critical comparison of techiques. *J. Phys. Chem. 83* (1979), 1333–1343.

[148] Ohta, N., Matsunami, S., Okazaki, S., and Yamazaki, I. Polarized absorption spectra and molecular orientation of some cyanine dyes in Langmuir-Blodgett monolayer films. *Langmuir 10* (1994), 3909–3912.

[149] PARISER, R. Theory of the electronic spectra and structure of the polyacenes and of alternant hydrocarbons. *J. Chem. Phys. 24* (1956), 250–268.

[150] PARISER, R., AND PARR, R. G. A semi-empirical theory of the electronic spectra and electronic structure of complex unsaturated molecules i. *J. Chem. Phys. 21* (1953), 466–471.

[151] PARK, S. H., YIN, P., LIU, Y., REIF, J. H., LABEAN, T. H., AND YAN, H. Programmable DNA self-assemblies for nanoscale organization of ligands and proteins. *Nano Lett. 5* (2005), 729–733.

[152] PARKER, C. A., AND REES, W. T. Correction of fluorescence spectra and measurement of fluorescence quantum efficiency. *Analyst 85* (1960), 587–600.

[153] PARKINSON, P., AHARON, E., CHANG, M. H., DOSCHE, C., FREY, G. L., KÖHLER, A., AND HERZ, L. M. Dimensionality-dependent energy transfer in polymer-intercalated SnS_2 nanocomposites. *Phys. Rev. B 75* (2007), 165206.

[154] PASCHOTTA, R. *Encyclopedia of Laser Physics and Technology*. Wiley-VCH, 2008.

[155] PICOQUANT GMBH. Technical Note: Time-Correlated Single Photon Counting. `http://www.picoquant.com/technotes/technote_tcspc.pdf`. Accessed: 18/09/2011.

[156] PINTO, Y. Y., LE, J. D., SEEMAN, N. C., MUSIER-FORSYTH, K., TATON, T. A., AND KIEHL, R. A. Sequence-encoded self-assembly of multiple-nanocomponent arrays by 2D DNA scaffolding. *Nano Lett. 5* (2005), 2399–2402.

[157] PLATT, J. R. Classification of spectra of cata-condensed hydrocarbons. *J. Chem. Phys. 17* (1949), 484–495.

[158] POPE, M., AND SWENBERG, C. E. *Electronic processes in organic crystals and polymers*. Oxford University Press, 1999.

[159] POWELL, R. C. Thermal and sample-size effects on the fluorescence lifetime and energy transfer in tetracene-doped anthracene. *Phys. Rev. B 2* (1970), 2090–2097.

[160] POWELL, R. C., AND KEPLER, R. G. Evidence for long-range exciton-impurity interaction in tetracene-doped anthracene crystals. *Phys. Rev. Lett. 22* (1969), 636–639.

[161] POWELL, R. C., AND SOOS, Z. G. Singlet exciton energy transfer in organic solids. *J. Lumines. 11* (1975), 1–45.

[162] QI, H. X., LI, G. Q., MAO, W. Y., WANG, Q. S., ZHU, T., AND LI, G. W. Fluorescence resonance energy transfer mediated by vesicles containing naphthalene moiety. *Dyes Pigment. 74* (2007), 454–457.

[163] RAHIM, N. A. A., MCDANIEL, W., BARDON, K., SRINIVASAN, S., VICKERMAN, V., SO, P. T. C., AND MOON, J. H. Conjugated polymer nanoparticles for two-photon imaging of endothelial cells in a tissue model. *Adv. Mater. 21* (2009), 3492–3497.

[164] RANA, D. K., SARKAR, A., DHAR, S., MANDAL, T. K., AND BHATTACHARYA, S. C. Modulated photophysics of 2-anthracene sulphonate in micellar assembly. *J. Lumines. 130* (2010), 1106–1112.

[165] RANJIT, S., GURUNATHAN, K., AND LEVITUS, M. Photophysics of backbone fluorescent DNA modifications: reducing uncertainties in FRET. *J. Phys. Chem. B 113* (2009), 7861–7866.

[166] ROBERTSON, N., AND MCGOWAN, C. A. A comparison of potential molecular wires as components for molecular electronics. *Chem. Soc. Rev. 32* (2003), 96–103.

[167] ROTHEMUND, P. W. K. Folding DNA to create nanoscale shapes and patterns. *Nature 440* (2006), 297–302.

[168] RUIZ-CARRETERO, A., JANSSEN, P. G. A., STEVENS, A. L., SURIN, M., HERZ, L. M., AND SCHENNING, A. P. H. J. Directing energy transfer in discrete one-dimensional oligonucleotide-templated assemblies. *Chem. Commun. 47* (2011), 884.

[169] RULLIÈRE, C. *Femtosecond Laser Pulses: Principles and Experiments*. Springer-Verlag, 1998.

[170] RUSECKAS, A., WOOD, P., SAMUEL, I. D. W., WEBSTER, G. R., MITCHELL, W. J., BURN, P. L., AND SUNDSTRÖM, V. Ultrafast depolarization of the fluorescence in a conjugated polymer. *Phys. Rev. B 72* (2005), 115214.

[171] SALONEN, A., KNYAZEV, A., VON BANDEL, N., DEGROUARD, J., LANGEVIN, D., AND DRENCKHAN, W. A novel pyrene-based fluorescing amphiphile with unusual bulk and interfacial properties. *ChemPhysChem 12* (2011), 150–160.

[172] SANBORN, M. E., CONNOLLY, B. K., GURUNATHAN, K., AND LEVITUS, M. Fluorescence properties and photophysics of the Sulfoindocyanine Cy3 linked covalently to DNA. *J. Phys. Chem. B 111* (2007), 11064–11074.

[173] SÁNCHESZ-MOSTEIRO, G., VAN DIJK, E. M. H. P., HERNANDO, J., HEILEMANN, M., TINNEFELD, P., SAUER, M., KOBERLIN, F., PATTING, M., WAHL, M., ERDMANN, R., VAN HULST, N. F., AND GARCÍA-PARAJÓ, M. F. DNA-based molecular wires: multiple emission pathways of individual constructs. *J. Phys. Chem. B 110* (2006), 26349–26353.

[174] SANCHEZ, A., FAHEY, R. E., STRAUSS, A. J., AND AGGARWAL, R. L. Room-temperature continuous-wave operation of a Ti:Al_2O_3 laser. *Opt. Letters 11* (1986), 363–364.

[175] SANCHEZ, A., FAHEY, R. E., STRAUSS, A. J., AND AGGARWAL, R. L. Room-temperature continuous-wave operation of a Ti:Al_2o_3 laser. *Opt. Letters 11* (1986), 363–364.

[176] SANTOSO, Y., HWANG, L. C., AND KAPANIDIS, A. N. Red light, green light: probing single molecules using alternating-laser excitation. *Biochem. Soc. Trans. 36* (2008), 738–744.

[177] SANTOSO, Y., AND KAPANIDIS, A. N. Probing biomolecular structures and dynamics of single molecules using in-gel alternating-laser excitation. *Anal. Chem. 81* (2009), 9561–9570.

[178] SCHEIDLER, M., LEMMER, U., KERSTING, R., KARG, S., RIESS, W., CLEVE, B., MAHRT, R. F., KURZ, H., BÄSSLER, H., GÖBEL, E. O., AND THOMAS, P. Monte carlo study of picosecond exciton relaxation and dissociation in poly(phenylenevinylene). *Phys. Rev. B 54* (1996), 5536–5544.

[179] SCHMID, S. A., ABBEL, R., SCHENNING, A. P. H., MEIJER, E. W., SIJBESMA, R. P., AND HERZ, L. M. Analyzing the molecular weight distribution in supramolecular polymers. *J. Am. Chem. Soc. 131* (2009), 17696–17704.

[180] SCHMID, S. A., ABBEL, R., SCHENNING, A. P. H. J., MEIJER, E. W., AND HERZ, L. M. Impact of nuclear lattice relaxation on the excitation energy transfer along a chain of $\pi-$conjugated molecules. *Phys. Rev. B 81* (2010), 085438.

[181] SCHWARTZ, B. J. Conjugated polymers as molecular materials: how chain conformation and film morphology influence energy transfer and interchain interactions. *Annu. Rev. Phys. Chem. 54* (2003), 141–172.

[182] SHAH, J. Ultrafast luminescence spectroscopy using sum frequency generation. *IEEE J. Quantum Electron. 24* (1988), 276–288.

[183] SHAW, P. E., RUSECKAS, A., AND SAMUEL, I. D. W. Exciton diffusion measurements in poly(3-hexylthiophene). *Adv. Mater. 20* (2008), 3516–3520.

[184] SHERWOOD, G. A., CHENG, R., SMITH, T. M., WERNER, J. H., SHREVE, A. P., PETEANU, L. A., AND WILDEMAN, J. Aggregation effects on the emission spectra and dynamics of model oligomers of MEH-PPV. *J. Phys. Chem. C 113* (2009), 18851–18862.

[185] SHINAR, J., AND SHINAR, R. Organic light-emitting devices (OLEDs) and OLED-based chemical and biological sensors: an overview. *J. Phys. D-Appl. Phys. 41* (2008), 133001.

[186] SHROFF, H., REINHARD, B. M., SIU, M., AGARWAL, H., SPAKOWITZ, A., AND LIPHARDT, J. Biocompatible force sensor with optical readout and dimensions of 6 nm^3. *Nano Lett. 5* (2005), 1509–1514.

[187] SHUQING, Z., CHAOEN, H., AND HONGWU, Z. Crystal growth and properties of lithium triborate. *J. Cryst. Growth 99* (1990), 805–810.

[188] SIRRINGHAUS, H., KAWASE, T., FRIEND, R. H., SHIMODA, T., INBASEKARAN, M., WU, W., AND WOO, E. P. High-resolution inkjet printing of all-polymer transistor circuits. *Science 290* (2000), 2123–2126.

[189] SOMSEN, O. J. G., KEUKENS, L. B., DE KEIJZER, M. N., VAN HOEK, A., AND VAN AMERONGEN, H. Structural heterogeneity in DNA: temperature dependence of 2-aminopurine fluorescence in dinucleotides. *ChemPhysChem 6* (2005), 1622–1627.

[190] SONY, P., AND SHUKLA, A. Large-scale correlated calculations of linear optical absorption and low-lying excited states of polyacenes: Pariser-Parr-Pople Hamiltonian. *Phys. Rev. B 75* (2007), 155208.

[191] SPADA, G. P., LENA, S., MASIERO, S., PIERACCINI, S., SURIN, M., AND SAMORÌ, P. Guanosine-based hydrogen-bonded scaffolds: controlling the assembly of oligothiophenes. *Adv. Mater. 20* (2008), 2433–2438.

[192] SPEARS, K. G., CRAMER, L. E., AND HOFFLAND, L. D. Subnanosecond time-correlated photon counting with tunable lasers. *Rev. Sci. Instrum. 49* (1978), 255–262.

[193] SPECTRA-PHYSICS. *Operator's Manual - Millennia Vis J, diode-pumped, CW visible laser*. Mountain View, CA.

[194] SPECTRA-PHYSICS. *Operator's Manual - Tsunami mode-locked Ti:Sapphire laser*. Mountain View, CA.

[195] STEVENS, A. L., JANSSEN, P. G. A., RUIZ-CARRETERO, A., SURIN, M., SCHENNING, A. P. H. J., AND HERZ, L. M. Energy transfer in single-stranded DNA-templated stacks of naphthalene chromophores. *J. Phys. Chem. C 115* (2011), 10550–10560.

[196] STINGL, A., LENZNER, M., SPIELMANN, C., KRAUSZ, F., AND SZIPOCS, R. Sub-1o-fs mirror-dispersion-controlled Ti-sapphire laser. *Opt. Lett. 20* (1995), 602–604.

[197] STROBL, G. *The physics of polymers*. Springer, 2007.

[198] SURIN, M., JANSSEN, P. G. A., LAZZARONI, R., LECLÈRE, P., MEIJER, E. W., AND SCHENNING, A. P. H. J. Supramolecular organization of ssDNA-templated π-conjugated oligomers via hydrogen bonding. *Adv. Mater. 21* (2009), 1126–1130.

[199] SURIN, M., MARSITZKY, D., GRIMSDALE, A. C., MÜLLEN, K., LAZZARONI, R., AND LECLÈRE, P. Microscopic morphology of polyfluorene-poly(ethylene oxide) block copolymers: influence of the block ratio. *Adv. Funct. Mater. 14* (2004), 708–715.

[200] SURIN, M., SONAR, P., GRIMSDALE, A. C., MÜLLEN, K., LAZZARONI, R., AND LECLÈRE, P. Supramolecular organization in fluorene/indenofluorene–oligothiophene alternating conjugated copolymers. *Adv. Funct. Mater. 15* (2005), 1426–1434.

[201] TOOMBS, G. A. Quasi-one-dimensional conductors. *Physics Reports 40* (1978), 181–240.

[202] TORIMURA, M., KURATA, S., YAMADA, K., YOKOMAKU, T., KAMAGATA, Y., KANAGAWA, T., AND KURANE, R. Fluorescence-quenching phenomenon by photoinduced electron transfer between a fluorescent dye and a nucleotide base. *Anal. Sci. 17* (2001), 155–160.

[203] UENO, Y., KOMATSUZAKI, S., TAKASU, K., KAWAI, S., KITAMURA, Y., AND KITADE, Y. Synthesis and properties of oligonucleotides containing novel fluorescent biaryl units. *Eur. J. Org. Chem. 2009* (2009), 4763–4769.

[204] VALEUR, B. *Molecular Fluorescence: Principles and Applications*. Wiley, 2002.

[205] VAN RIJN, P., JANELIUNAS, D., BRIZARD, A. M. A., STUART, M. C. A., EELKEMA, R., AND VAN ESCH, J. H. Introduction of curvature in amphipathic oligothiophenes for defined aggregate formation. *Chem.-Eur. J. 16* (2010), 13417–13428.

[206] VYON INC., J. Symphony: 1024×256 Cryogenic Open Electrode CCD Detector. `http://www.horiba.com/fileadmin/uploads/Scientific/Documents/OSD0028256FIOPLN.pdf`. Accessed: 17/09/2011.

[207] VYON INC., J. TRIAX Series. `http://www.horiba.com/fileadmin/uploads/Scientific/Documents/Mono/triax.pdf`. Accessed: 17/09/2011.

[208] WANG, F. K., AND BAZAN, G. C. Aggregation-mediated optical properties of pH-responsive anionic conjugated polyelectrolytes. *J. Am. Chem. Soc. 128* (2006), 15786–15792.

[209] WESTENHOFF, S., DANIEL, C., FRIEND, R. H., SILVA, C., SUNDSTRÖM, V., AND YARTSEV, A. Exciton migration in a polythiophene: probing the spatial and energy domain by line-dipole förster-type energy transfer. *J. Chem. Phys. 122* (2005), 094903.

[210] WOLF, U., ARKHIPOV, V. I., AND BÄSSLER, H. Current injection from a metal to a disordered hopping system. i. Monte Carlo simulation. *Phys. Rev. B 59* (1999), 7507–7513.

[211] WU, C. F., BULL, B., CHRISTENSEN, K., AND MCNEILL, J. Ratiometric single-nanoparticle oxygen sensors for biological imaging. *Angew. Chem.-Int. Edit. 48* (2009), 2741–2745.

[212] WU, C. F., AND MCNEILL, J. Swelling-controlled polymer phase and fluorescence properties of polyfluorene nanoparticles. *Langmuir 24* (2008), 5855–5861.

[213] WU, C. F., PENG, H. S., JIANG, Y. F., AND MCNEILL, J. Energy transfer mediated fluorescence from blended conjugated polymer nanoparticles. *J. Phys. Chem. B 110* (2006), 14148–14154.

[214] WU, C. F., SZYMANSKI, C., CAIN, Z., AND MCNEILL, J. Conjugated polymer dots for multiphoton fluorescence imaging. *J. Am. Chem. Soc. 129* (2007), 12904–12905.

[215] WU, C. F., SZYMANSKI, C., AND MCNEILL, J. Preparation and encapsulation of highly fluorescent conjugated polymer nanoparticles. *Langmuir 22* (2006), 2956–2960.

[216] WU, C. F., ZHENG, Y. L., SZYMANSKI, C., AND MCNEILL, J. Energy transfer in a nanoscale multichromophoric system: fluorescent dye-doped conjugated polymer nanoparticles. *J. Phys. Chem. C 112* (2008), 1772–1781.

[217] YANG, W., XIA, P. F., AND WONG, M. S. Highly ordered assembly of π-stacked distyrylbenzenes by oligoadenines. *Org. Lett. 12* (2010), 4018–4021.

[218] YANG, X. C., LU, R., XUE, P. C., LI, B., XU, D. F., XU, T. H., AND ZHAO, Y. Y. Carbazole-based organogel as a scaffold to construct energy transfer arrays with controllable fluorescence emission. *Langmuir 24* (2008), 13730–13735.

[219] YOUNG, M. *Optics and lasers*. Springer, 2000.

[220] YU, J. B., WU, C. F., SAHU, S. P., FERNANDO, L. P., SZYMANSKI, C., AND MCNEILL, J. Nanoscale 3D tracking with conjugated polymer nanoparticles. *J. Am. Chem. Soc. 131* (2009), 18410–18414.

[221] ZHANG, X., CHEN, Z. J., AND WÜRTHNER, F. Morphology control of fluorescent nanoaggregates by co-self-assembly of wedge- and dumbbell-shaped amphiphilic perylene bisimides. *J. Am. Chem. Soc. 129* (2007), 4886–4887.

[222] ZHANG, X., REHM, S., SAFONT-SEMPERE, M. M., AND WÜRTHNER, F. Vesicular perylene dye nanocapsules as supramolecular fluorescent pH sensor systems. *Nat. Chem. 1* (2009), 623–629.

[223] ZHAO, Z., YAN, H., AND LIU, Y. A route to scale up DNA origami using DNA tiles as folding staples. *Angew. Chem. Int. Edit. 49* (2010), 1414–1417.

[224] ZLATANOVA, J., LINDSAY, S. M., AND LEUBA, S. H. Single molecule force spectroscopy in biology using the atomic force microscope. *Prog. Biophys. Mol. Biol. 74* (2000), 37–61.

[225] ZUPKE, O., DISTLER, E., BAUMANN, D., STRAND, D., MEYER, R. G., LANDFESTER, K., HERR, W., AND MAILÄNDER, V. Preservation of dendritic cell function upon labeling with amino functionalized polymeric nanoparticles. *Biomaterials 31* (2010), 7086–7095.